



Rheinisch-Westfälische Technische Hochschule Aachen

Institut für Eisenhüttenkunde

- Materials Science of Steel –

Master Thesis

**Development of an Automated Strategy to
Calibrate Crystal Plasticity Subroutines for
ABAQUS, Using Machine Learning Approaches,
and Neural Networks**

Orkun Karagüllü

Matr.-Nr. 374039

From 01.06.2020 to 01.12. 2020

Examiner: Univ. Prof. Dr.-Ing. Sebastian Münstermann

Supervisor: Manuel Henrich

Acknowledgment

I would like to express my best thankfulness to Prof. Dr.-Ing. S. Münstermann for providing me the opportunity to work on this thesis in IEHK, RWTH Aachen. I use this opportunity to thank my supervisor MSc. M. Henrich for his management and intelligence in every step of this project. Without his surveillance, this project could not be realized.

Table of Contents

1	Abstract.....	1
2	Introduction	2
3	State of the Art	3
3.1	Materials	3
3.1.1	Dual Phase Steel.....	4
3.1.2	Pipeline Steel.....	5
3.2	Nanoindentation Test.....	6
3.2.1	Instruments	7
3.2.2	Force-Displacement Curve	9
3.3	Metallurgical Fundamentals of Elastoplastic Deformation.....	11
3.3.1	Dislocation Movement.....	12
3.3.2	Schmid` <i>s</i> Law	14
3.4	Crystal Plasticity Finite Element Method.....	15
3.4.1	Constitutive Model	16
3.5	Data Analysis	17
3.5.1	Response Surface Methodology.....	19
3.5.1.1	Morris Sensitivity Analysis.....	19
3.5.1.2	Latin Hypercube Sampling	22
3.5.1.3	Root Mean Square Error	23
3.5.1.4	Polynomial Regression.....	23
3.5.1.5	Particle Swarm Optimization	24
3.5.2	Machine Learning	26
4	Experimental Procedure.....	28
4.1	Materials Setup	28
4.1.1	Dual Phase Steel	28
4.1.2	Pipeline Steel.....	31

4.2	Nanoindentation Setup	32
4.2.1	Sample Preparation	32
4.2.2	Nanoindentation Test.....	33
4.3	Simulations Setup	34
4.3.1	Simulation Inputs	34
4.3.2	Automating Simulation Process	37
4.4	Artificial Intelligence Model.....	39
4.5	Response Surface Model.....	44
5	Results	47
5.1	Mechanical Test Results	47
5.2	Simulation Results	51
5.3	Artificial Intelligence Model.....	53
5.3.1	Dual-Phase Steel Artificial Intelligence Model.....	53
5.3.2	Pipeline Steel Artificial Intelligence Model.....	59
5.4	Response Surface Model.....	64
5.4.1	Morris Sensitivity Analysis	64
5.4.2	Response Surface Model for Dual-Phase Steel.....	65
5.4.3	Response Surface Model for Pipeline Steel.....	69
6	Discussion.....	74
6.1	Nanoindentation Test.....	74
6.2	FEM Simulations.....	75
6.3	Artificial Intelligence Model.....	78
6.4	Response Surface Model.....	81
7	Conclusion and Outlooks	85
8	Literatur.....	87

1 Abstract

The past decades have seen the rapid development of computational material science and under this topic, crystal plasticity (CP) modeling plays an important role in investigating mechanical structure-property relationships in crystalline materials such as strain hardening in single crystals or texture evolution in polycrystalline aggregates. Despite its unignorable positive outcome in materials science and engineering, it has a number of challenges in use. Although extensive research has been carried out on CP, there are only a few standardized calibration methods for the determination of the material's CP parameters available.

The objective of this research is to develop a method that can be used as a better calibration tool of CP parameters. The methodological approach taken in this study is a mixed methodology based on machine learning. Two models are created which are respectively based on artificial neural networks (AI model) and Response Surface (RS) methodology in combination with Particle Swarm Optimization (PSO).

The results indicated that the AI model shows great success to mimic simulations and very successfully identify the CP parameters, on the other hand, it is dependent on the range of the provided parameter set which makes this method unreliable when the given parameter is outside of the permitted range. Moreover, deep neural networks require a lot of simulation data, which makes it computationally expensive. On the contrary, the SR model is not able to mimic a simulation, but it is less dependent on the given parameter range due to its polynomial fitting capability and finally, compared to the AI model it is computationally less expensive.

These results suggest that the SR model is more flexible compared to the AI model, however, PSO is not as sensitive as AI, which makes AI more accurate for a given parameter set but it comes with several limitations. Overall both models can be used for predicting CP parameters.

2 Introduction

Nanoindentation was developed in the early 1970s (1) and has become an increasingly popular technique for mechanical characterization. It is theoretically based on contact mechanics which has been studied for more than a century, starting with Heinrich Hertz's revolutionary work on two linearly elastic isotropic solids in 1881 (2). Their popularity is mainly due to the increased interest in thin films and specimens with relatively small dimensions, which is required by modern applications such as microelectronics, nano, and biomaterials (3). The high accuracy and resolution of depth and load measurement of the indentation test make it a reliable technique for determining mechanical properties like hardness and elasticity modulus.

In this study, nanoindentation tests were performed on dual-phase (DP) and pipeline (PL) steels. DP steels were developed in the 1970s in order to compensate for the requirements of carmakers. The main advantages of using this steel are weight reduction, improving safety parameters with economical costs (4). On the other hand, the use of high-strength PL steels have been the largest oil and gas delivery network for the last 50 years due to its high strength and high resistance to corrosion (5). PL steels can greatly reduce overall costs in the construction of natural gas or crucial oil transmission systems, many attempts have been made to develop and introduce higher-grade PL steels.

Based on the crystallographic structure of the ferrite phase in DP, and bainite phase in PL steel, the main deformation mechanism is dislocation slip which can be simulated via Crystal Plasticity Finite Element Method (CPFEM). CPFEM is a CP model that can work together with finite element softwares. The orientation of a single grain, its response to an applied force, changes in orientations under the applied force, and the stresses on each slip system can be simulated by this method (6).

CPFEM is becoming a key instrument modeling materials microstructure, however, a primary concern of CPFEM is the calibration of CP parameters. The major objective of this study is to create a robust solution to this issue by using machine learning algorithms. For that purpose, SR and AI models were created from scratch by using Python programming language (version 3.7.3), and their curve-fitting capabilities are investigated.

3 State of the Art

In this chapter, theoretical information will be provided for the purpose of understanding the chosen materials, basic concepts and the mechanics of the nanoindentation test, crystal plasticity theory, CPFEM, and the predetermined workflow which is used for identifying the CP parameters. For this work, 2 main approaches were used to optimize CP parameters which are SR methodology and deep learning (DL). For the SR model, Morris sensitivity analysis, polynomial regression, and particle swarm optimization algorithm will be explained. As to the AI model, understanding artificial neural networks (ANN) and their working principles gain importance. However, these approaches are based on sophisticated statistical and mathematical concepts and the scope of this work is materials science rather than data science. For that reason, a relatively simple and easy explanation of these concepts is preferred.

3.1 Materials

This work aims to study by nanoindentation test the mechanical properties of single ferrite grain in DP steel, and bainite grain in PL steel X65. DP steels were firstly developed in the 1970s in order to compensate for the requirements of the car industry. The main advantages of using these steels are weight reduction, improving safety parameters with economical costs (7). DP steels provide a large range of different mechanical properties based on their microstructure. The characteristic mechanical properties due to its heterogeneous microstructure, which consists of 5-50 volume% martensite islands and fine-grained ferrite matrix. They also show high strain hardening and good fatigue resistance. For DP steels the yield strength is 280/300 MPa and UTS is above 590/600 MPa (8). There are two types of PL steel which are welded and seamless. Seamless PL steel production was tried by different methods in the mid-nineteenth century; the Mannesmann process was invented in Germany in 1885 and introduced in England commercially in 1887 (9). In this study, the chosen steel grade (X65) belongs to the seamless PL steel category. To understand this commercially and technically attracting materials deeper explanations about the process, microstructure, and chemical properties of DP and PL steels take place in this section.

The process route of DP and PL steels are separately and shortly introduced in order to prepare a basic knowledge about the materials.

3.1.1 Dual Phase Steel

Figure 1 illustrates how steel slab can be used to make DP steel. First, to achieve a completely austenitic microstructure, the slab heating around 1200 °C. The time and temperature parameters of this phase of reheating depend largely on the chemical composition of the grades of steel.

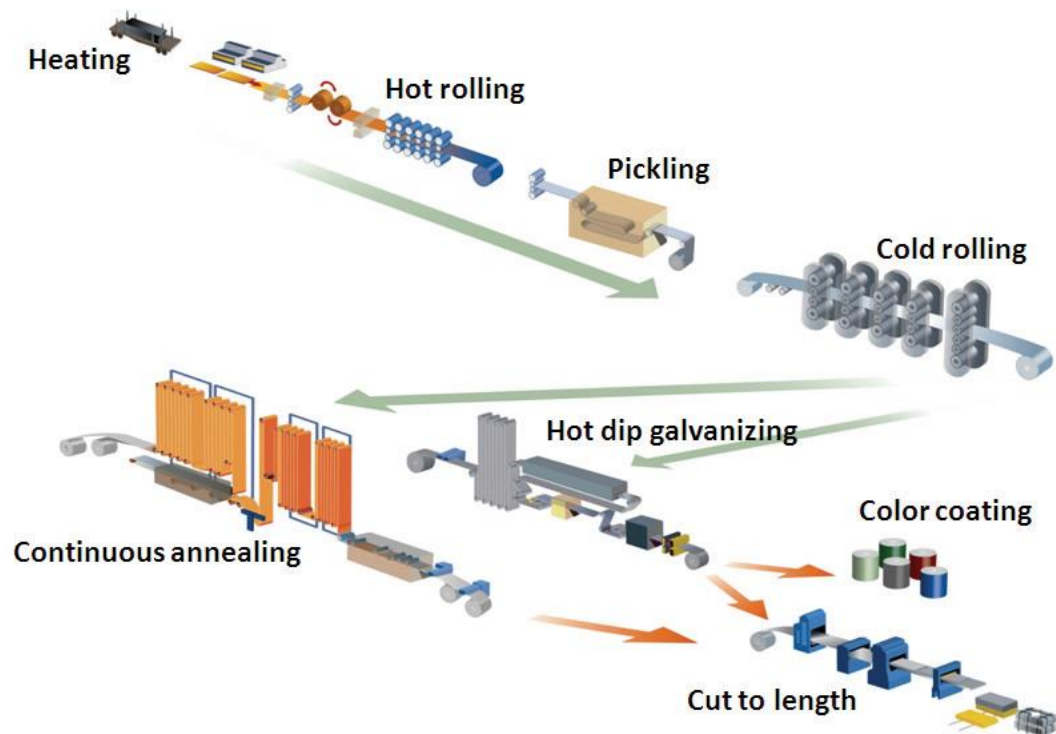


Figure 1: A schematic representation of the DP steel production. (10)

During the reheating process, slabs are hot rolled in the austenitic field and then cooled down to have ferritic and pearlitic phases (11) with required grain size and homogeneous alloying particle distribution. Upon going to cold rolling steel strips should be cleaned from oxide layers which are formed during the cooling cycle. To do so, hydrochloric acid is added to the steel in pickling rows. This increases the surface quality and from now on the material is ready for the cold rolling process. The thickness of the strip decreases in the cold rolling process, and thus the ferritic phase deforms and elongates through the rolling direction. This also represents a very significant step toward surface quality. Cold rolling steel is coiled and moved to the continuous annealing line. After that, firstly, the material is preheated at around 820 °C. The pre-

deformed ferritic matrix starts to recrystallize after heating. The degree of recrystallization depends on the degree of deformation, the chemical composition, and the rate of heating. The phase transformation from ferrite to austenite and carbide dissolution occurs during soaking. The amount of the austenitic phase is influenced by soaking parameters such as time and temperature. After the soaking stage, the material is quenched. This stage is crucial for the formation of the martensitic phase via the transformation of the austenitic phase. Lastly, the steel sheet is tempered to modify the final microstructural properties to add a bit more ductility (12).

3.1.2 Pipeline Steel

As seen in **Figure 2** a steel billet is heated to forging temperature (around 1150 °C) in the mandrel (Pilger) mill process, and placed between the rolls of a hot rotary piercing mill. The piercing point is mounted in the center of the billet, and the rotating rolls are designed to push the billet over the piercing point, creating a hole in the middle of the billet along its entire length as it passes through the tilted rolls. A mandrel with an outer diameter roughly equal to the finished pipe diameter is entered into the billet's pierced hole.

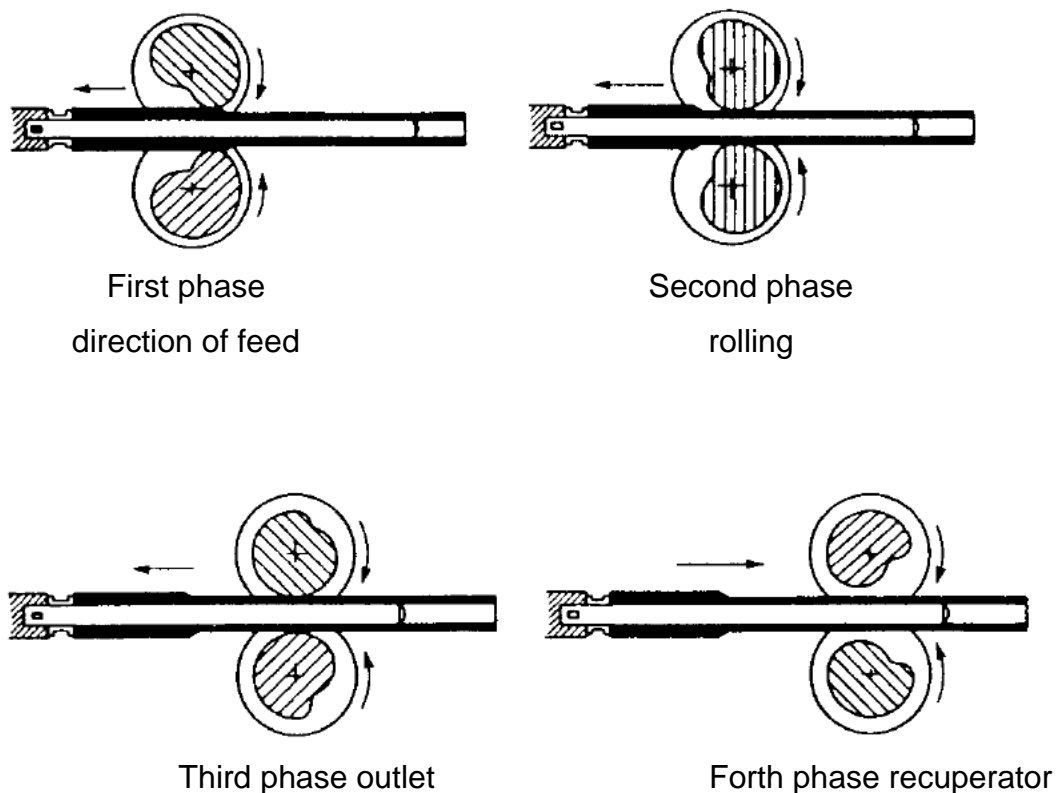


Figure 2: Production of seamless pipe steel. (9)

Then, mandrel and billet are mounted together between rolls of a pilger-mill mold with a cam-shaped contour and revolving counter to the direction in which the billet is driven through a hydraulic and pneumatic ram system. Later on, the rolls first grab the hot billet in the pilger-mill and form a shaft after some rotation. The roll pressure pushes the billet away, and the resultant tube segment in the corresponding portion of the roll groove is compressed and smoothed out. Once the cam shape has reached the open portion, the ram mechanism forces the billet into the rolls again. The tube is reheated after the pilger-mill cycle and pushed through a sizer to have a more consistent diameter (9).

3.2 Nanoindentation Test

The indentation or conventional hardness test is a type of characterization method that is relatively cost-effective, easy to set up, useful, and widely used since the 1900s (13). It serves to examine the hardness of materials which is highly important in the fields of mechanical and material engineering. The test procedure is relatively simple. An indenter with a precise shape and made of a hard material like diamond penetrates the sample under an exact pressure and is then drawn back. Next, the hardness of the material can be calculated by means of the deformed area. Based on this methodology different hardness testing methods were developed like the Vickers hardness test, the Knoop hardness test, and the Rockwell hardness test. (14)

The development of the nanoindentation method goes back to the beginning of the 1970s and since then especially with the help of accelerating developments in thin films, microelectronics, and microelectromechanical systems this characterization method gained popularity (1, 15, 16). In the late 90s, on the other hand, a new era of study became more and more famous which is called “Nanotechnology”. Since then, material properties at nanoscales became more attractive. Further technological developments such as the reduction of the tip size, eased the determination of the depth and load measurements of the indenter in nanoscales. Eventually nanoindentation test, in other words, depth-sensing indentation technique was found by Oliver et. al in 1992 (17). With this method, force-displacement data could be gathered with a computer and based on the theory of contact elasto-mechanics, elastic modulus, and hardness could be calculated. Moreover, analyzing the force-

displacement curve which is shown in **Figure 3**, further material properties like phase transformation, viscoelasticity, fracture toughness, strain hardening, creeping, residual stresses, and dislocation movements can also be gathered. (18)

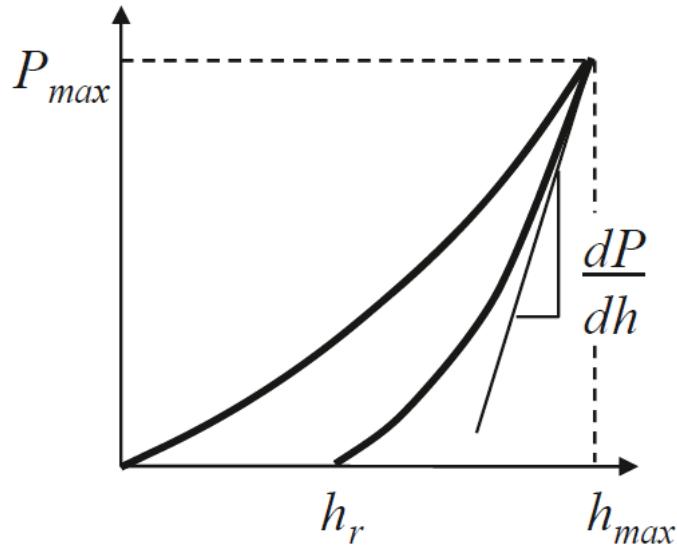


Figure 3:A general example of the force-displacement curve (19).

3.2.1 Instruments

As it is explained before the nanoindentation test can be concluded as collecting force and displacement data. For that reason, the experimental setup has vital importance. The forces which are involved during the test are in millinewton ($10^{-3} N$) range and for that reason, the sensitivity of the force sensor should be in nanonewton ($10^{-9} N$) range. Moreover, to measure penetration depth the sensitivity of the depth sensor should be in the nanometer $10^{-9} m$ range. (19)

The core components of the nanoindentation test are shown in **Figure 4** which are :

- Nanoindenter that serves for penetration,
- Optical Microscope (OM) for imaging the indents,
- Atomic Force Microscope (AFM) for analyzing 3D topography of indents at the nanoscale,
- Piezoelectric Sensor for determining the position of the indenter.

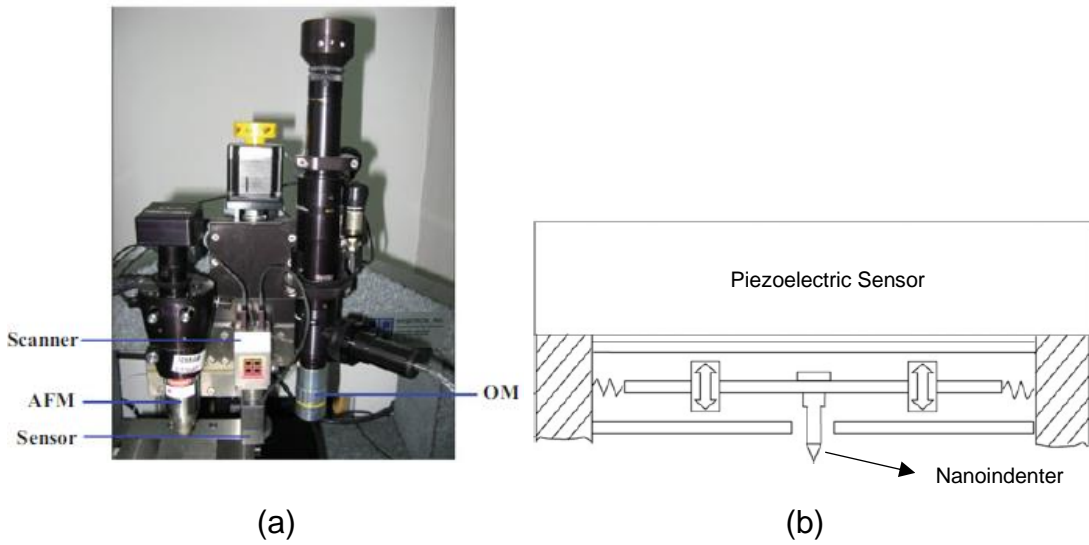


Figure 4: Core components of the nanoindentation test (a) inside view, (b) principle diagram (18).

When it comes to the indenter itself, it should be said that there are a few different types like the conventional indentation test. These are Berkovich, Vickers, Cube-Corner, Cone, and Sphere indenters which are illustrated in **Figure 5**. It is fundamentally important that based on the application a suitable nanoindenter must be chosen. The application ranges and shape features of different indenters are shown in **Table 1**.

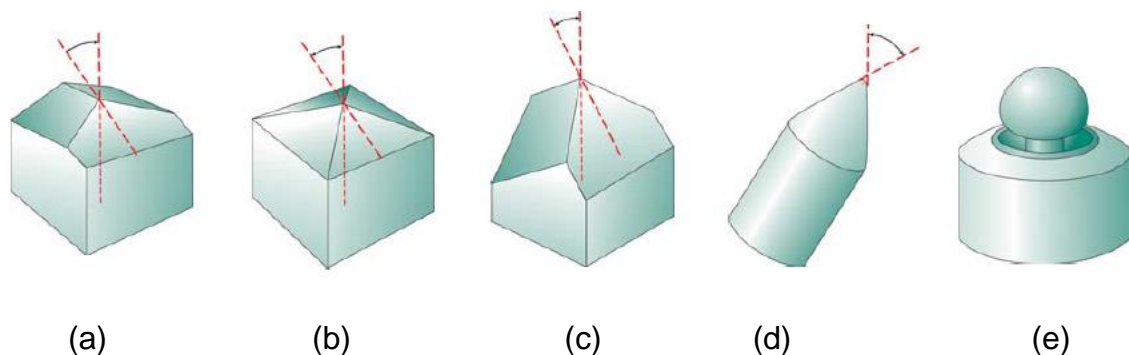


Figure 5: Types of nanoindenters respectively (a) Berkovich, (b) Vickers, (c) Cube-Corner, (d) Cone, and (e) Sphere (20).

Table 1: Shape and application ranges of different types of nanoindenters. (20)

Features	Berkovich	Vickers	Cube- Corner	Cone	Sphere
Shape	3-sided pyramid	4-sided pyramid	3-sided pyramid	Conical	Spherical
Applications	Bulk Materials, Thin Films, Polymers, Scratch Testing, Wear Testing, MEMS, Imaging	Bulk Materials, Films and Foils, Scratch Testing, Wear Testing	Thin Films, Scratch Testing, Fracture Toughness, Wear Testing, MEMS, Imaging Modeling	Modeling, Scratch Testing, Wear Testing, Imaging, MEMS	MEMS

3.2.2 Force-Displacement Curve

In the previous section, it was said that hardness and elastic modulus are calculated by means of the force-displacement curve. **Figure 6** presents an overview of the nanoindentation test. During the test, the load is applied from zero to maximum.

Firstly, the indenter penetrates the material and causes elastic deformation on the sample surface. Secondly, the plastic deformation occurs, and under the maximum load, h_{\max} is reached. These two types of deformations (elastic and plastic) cause the nonlinearity of the load curve. Finally, the load is turned back from maximum to zero and the recovery of the elastic portion of the deformation occurs and h_r is reached after total unloading. The indenter leaves the surface with tiny plastic deformation. This process should be repeated a few times in order to get reliable data from the experiment.

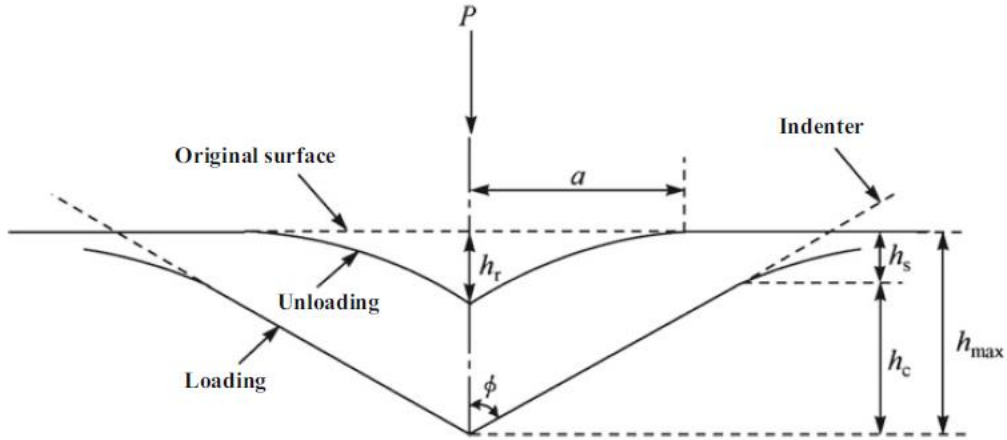


Figure 6: Illustration of the tested surface during and after the loading process (21).

In Figure 6 the symbols can be demonstrated as follows:

ϕ = cone semi angle,

a = radius of the indenter,

h_c = penetration depth,

h_s = the distance between the contact circle and surface.

Based on these data the contact stiffness can be calculated experimentally via the slope of the upper part of the unloading curve (Figure 3) which is described in **Eq. 1**:

$$S = \frac{dP}{dh} \quad 1.$$

where S stands for stiffness and P is force. Then the contact depth h_c can be calculated with the equation below:

$$h_c = h_{max} - \varepsilon \frac{P_{max}}{S} \quad 2.$$

In **Eq. 2**, h_{max} stands for total indent displacement, P_{max} is maximum force and ε is the geometrical parameter of the indenter e.g. $\varepsilon = 0.75$ for Berkovich indenter.

Based on these equations hardness can be calculated via the equation below:

$$H = \frac{P_{max}}{A_c} \quad 3.$$

where A_c stands for the projected contact area that is determined by the indenter geometry. Finally, the reduced elastic modulus that gives the elastic deformation of both indenter and sample can be calculated with the equation below:

$$E_r = \frac{S\sqrt{\pi}}{2\beta\sqrt{A_c}} \quad 4.$$

where β is a constant that is determined by indenter geometry e.g. $\beta = 1.034$ for the Berkovich indenter (18).

3.3 Metallurgical Fundamentals of Elastoplastic Deformation

The microstructure is a small scale structure that has a strong effect on mechanical properties such as strength, toughness, ductility, hardness, wear resistance, etc. Not only thermodynamic potentials but also kinetics play an important role in the evolution of microstructure and its properties such as its direction and formation. Due to the harmony between thermodynamic and kinetics, microstructures are not in fully thermodynamic equilibrium and this causes various lattice defects. These defects are beneficial for material engineering and contribute elastoplastic deformation of metals. Between these defects, the most important one is dislocations which are the main carrier of deformation, and for that reason, dislocation mechanisms should be emphasized. (22)

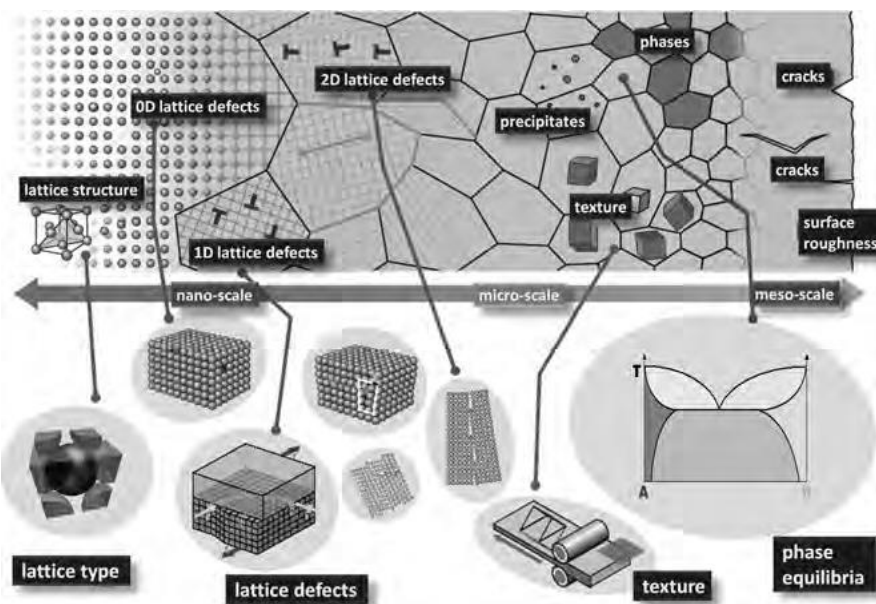


Figure 7: Illustration of some of the most important defects in material engineering. (22)

3.3.1 Dislocation Movement

The nanoindentation test is carried out on a single crystal and for that reason deformation mechanism in a single crystal gain importance. In order to move a dislocation, a force (F) is required and shear stress τ fulfills this requirement. The necessary shear stress can be calculated with the following equation:

$$W = \tau \cdot l_1 \cdot l_3 \cdot b \quad 5.$$

where l_1, l_3 stands for crystal lengths and b for the burgers vector (**Figure 8**), W is the required work in order to displace the upper part of the crystal by the distance b which is demonstrated in Figure 8c. Alternatively this equation can be written as:

$$W = l_1 \cdot l_3 \cdot F \quad 6.$$

By analogy, the last two equations show that:

$$F = \tau \cdot b \quad 7.$$

The general stress state σ with the force per unit length on any dislocation with sense vector s is described in the equation below:

$$F = (\sigma \cdot b) \times s \quad 8.$$

Eq. 8 is called the Peach-Koehler equation which gives the relation between the macroscopic and microscopic mechanism of deformation. In other words, this equation explains the effect of the force-displacement diagram of the dislocations on the stress-strain diagram (23).

The necessary shear stress that is required to move a dislocation on its slip plane called Peierls stress τ_p and it is formulated as:

$$\tau_p = \frac{2G}{1-\nu} \exp\left(-\frac{-2\pi}{(1-\nu)} \frac{d}{b}\right) \quad 9.$$

In **Eq. 9** ν stands for Poisson's ratio. Peierls stress increases with increasing shear modulus G , however, its relationship with the ratio of the lattice spacing d divided by the burgers vector b is exponential. So it can be said that with increasing the lattice plane distance and decreasing the burgers vector, the Peierls stress increases exponentially. Lattice spacing can be described with the help of Miller indices $\{hkl\}$ and lattice parameter a in the following equation:

$$d = \frac{a}{\sqrt{h^2 + k^2 + l^2}} \quad 10.$$

Based on **Eq. 10** it can be said that d becomes larger when index values are smaller. Furthermore, the burgers vector b becomes smaller through close-packed directions. For ferrite, which is the only phase in the scope of this study, the crystal structure is body-centered cubic crystal (bcc). In bcc crystals, the most densely-packed direction is the (111) direction and the most densely-packed planes are the {110} planes and then {112} and {123} planes. For that reason, 3 slip systems which are {110}(111), {112}(111), and {123}(111) observed in this structure as it is illustrated in **Figure 9**. A general overview of slip systems can be found in **Table 2**.

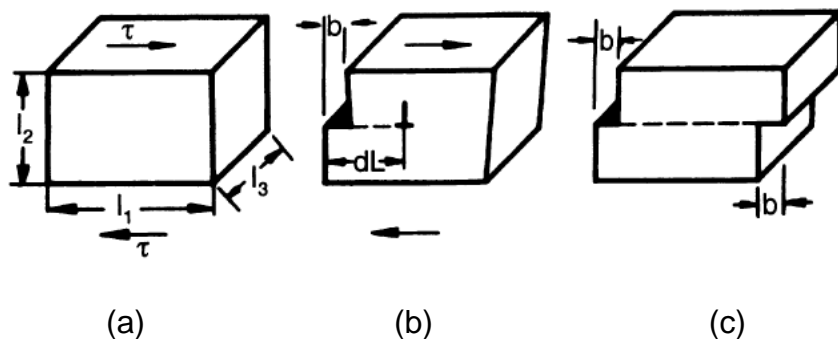


Figure 8: Step by step changes in the shape of the crystal during the dislocation movement. (23)

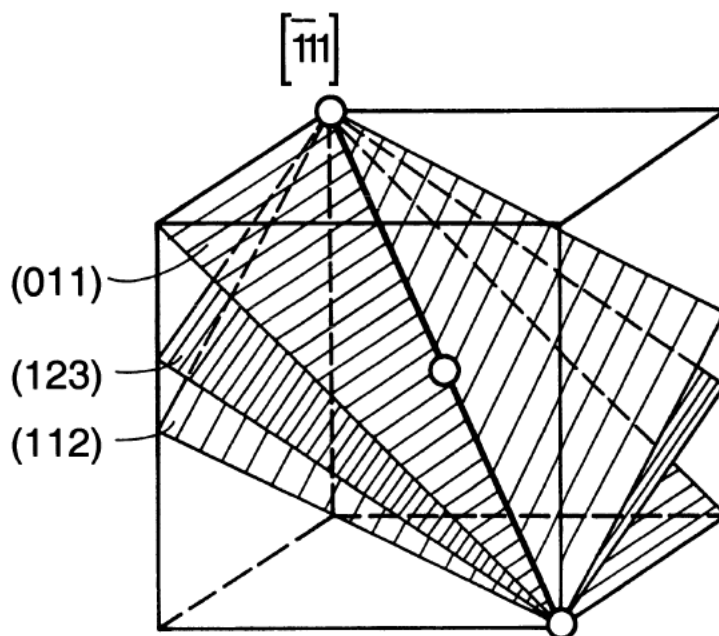


Figure 9: Demonstration of 3 slip systems in bcc lattice. (23)

Table 2: A general overview of lattice types with their slip systems. (23)

Crystal Structure	Slip Plane	Slip direction	Number of non-parallel planes	Slip directions per plane	Number of slip systems
fcc	{111}	$\langle 110 \rangle$	4	3	12
bcc	{110}	$\langle 111 \rangle$	6	2	12
	{112}	$\langle 111 \rangle$	12	1	12
	{123}	$\langle 111 \rangle$	24	1	24
hcp	{1000}	$\langle 11\bar{2}0 \rangle$	1	3	3
	{10\bar{1}0}	$\langle 11\bar{2}0 \rangle$	3	1	3
	{10\bar{1}1}	$\langle 11\bar{2}0 \rangle$	6	1	6

3.3.2 Schmid's Law

Schmid's law (**Eq. 11**) is used in order to determine the slip plane and direction of material which can resolve the highest shear stress τ (24). The resolved shear stress is influenced by the tensile stress applied to the material σ , the angle between tensile direction and slip plane normal k , and the angle between tensile direction and slip direction λ (**Figure 10**).

$$\tau = \sigma \cdot \cos(k) \cdot \cos(\lambda) = m\sigma \quad 11.$$

The applied force on the dislocation depends on the orientation of the slip system. If there are multiple slip systems in a crystal, then these systems exhibit different Schmid-factors m . In this case, the slip system with the highest Schmid factor would contain the highest shear stress and therefore, carry the plastic deformation if the resolved shear stress exceeds the critical shear value τ_0 . The critical shear stress is a constant and the same for all the slip systems. This is the proven statement of Schmid's law.

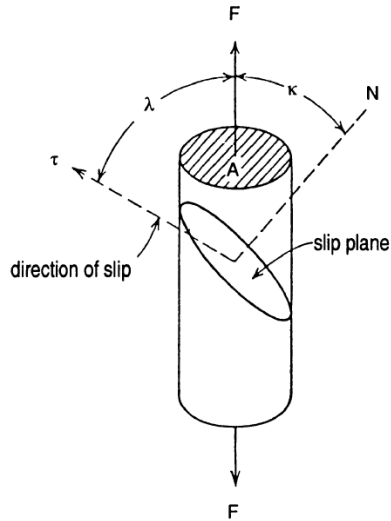


Figure 10: Explanation of Schmid's Law in a simple illustration. (23)

3.4 Crystal Plasticity Finite Element Method

The finite element was firstly proposed in 1943 (25). Then this method was developed by O.C. Zienkiewicz in 1967 with his publication “The Finite Element Method in Structural and Continuum Mechanics” (26) The CP theory can be coupled with the finite element method (FEM) and is then called the CPFEM (27). In 1982, for the first time, CPFEM simulations were carried out (28) but due to computational restrictions, the first simulations were simple. They consisted of two symmetric slip systems for simulating the tensile behavior of a single crystal. Thanks to increasing computation power, simulations became more complex and in 1988 Harren et al. (29) applied CPFEM to polycrystallines with two or three slip systems.

CPFEM is nowadays a widely used tool for investigating microscopic factors that affect the plastic deformation of metals (30). There is a wide range of application areas for CPFEM such as single crystal deformation, recrystallization, texture analysis, stamping, drawing, and finally nanoindentation which is in the scope of this study. Today, by means of the user-defined subroutines e.g. HYPELA2 in MSC. Marc or UMAT/VUMAT the CPFEM constitutive laws can be modeled in ABAQUS or other software.

3.4.1 Constitutive Model

In this study, CPFEM model formulation is constructed on dislocation slip which is explained in the previous section. The necessary equations, with tensors written in bold letters, are explained in the following (31):

$$\mathbf{F} = \mathbf{F}_e \mathbf{F}_p \quad 12.$$

where the force gradient \mathbf{F} is the ensemble of two parts which are pure elastic (reversible) \mathbf{F}_e and pure plastic (irreversible) \mathbf{F}_p . \mathbf{F}_p is the result of the plastic shearing on the crystallographic slip system and \mathbf{F}_e is due to the stretching and rotation of the crystal lattice. Shortly, deformation occurs in two steps. First, \mathbf{F}_p causes the movement of the material through the undeformed crystal lattice and then, both the lattice and material deform together which cause an increment on \mathbf{F}_e . The plastic deformation gradient rate $\dot{\mathbf{F}}_p$ can be derived as:

$$\dot{\mathbf{F}}_p = \mathbf{L}_p \mathbf{F}_p \quad 13.$$

where \mathbf{L}_p is the plastic velocity gradient and can be expressed as:

$$\mathbf{L}_p = \sum_{\alpha=1}^N \dot{\gamma}^\alpha \mathbf{m}^\alpha \times \mathbf{n}^\alpha \quad 14.$$

where for a slip system α , \mathbf{m}^α and \mathbf{n}^α stand for the unit vectors expressing the slip direction and normal direction to the slip plane. $\dot{\gamma}^\alpha$ represents the slip rate and N is the number of slip planes. The shear rate $\dot{\gamma}^\alpha$ is dependent on the resolved shear stress τ^α and the critical resolved shear stress τ_c^α . The kinetic law on the α slip system can be written as:

$$\dot{\gamma}^\alpha = \dot{\gamma}_0 \left| \frac{\tau^\alpha}{\tau_c^\alpha} \right|^m sgn(\tau^\alpha) \quad 15.$$

where $\dot{\gamma}_0$ and m represent respectively shear rate and the rate sensitivity for the slip system α . The resolved shear stress τ^α can be introduced as:

$$\tau^\alpha = \mathbf{S} \cdot (\mathbf{m}^\alpha \times \mathbf{n}^\alpha) \quad 16.$$

where \mathbf{S} represents the second Piola-Kirchhoff stress in the intermediate structure that is determined by \mathbf{F}_e . On the other hand, the micro-mechanical interactions between other slip systems should be taken into account with the following equation:

$$\dot{\tau}_c^\alpha = \sum_{\beta=1}^N h_{\alpha\beta} |\dot{\gamma}^\beta| \quad 17.$$

where $h_{\alpha\beta}$ represents the hardening matrix and defined as:

$$h_{\alpha\beta} = q_{\alpha\beta} \left[h_0 \left(1 - \frac{\tau_c^\beta}{\tau_c^s} \right)^a \right] \quad 18.$$

where h_0 , a and τ_c^s are slip hardening parameters. Furthermore, $q_{\alpha\beta}$ consist of the effect of self-hardening $\alpha = \beta$ and latent hardening $\alpha \neq \beta$ and equal to 1.0 for the coplanar slip otherwise 1.4. Finally, the hardening evolution law of the slip system α is determined by means of the following equation:

$$\tau_c^\alpha = \tau_0 + \int_0^t q_{\alpha\beta} \left[h_0 \left(1 - \frac{\tau_c^\beta}{\tau_c^s} \right)^a \right] |\dot{\gamma}^\beta| dt \quad 19.$$

where τ_0 stands for the initial critical resolved shear stress. So, it can be concluded that the CPFEM model consists of 6 parameters which are $\tau_0, \tau_c^s, h_0, a, \dot{\gamma}$ and m .

3.5 Data Analysis

In this, work hundreds of simulations are carried out based on a defined workflow. Results are analyzed based on machine learning approaches. Current methods are shown in **Figure 11** and **Figure 12**. The first step of the computational section is to identify which two of the CP parameters have a higher influence on the curve. To do so, Morris Sensitivity Analysis (MSA) was carried out. Afterward, a batch of simulation inputs generated in the range of values that are determined from the literature. For that purpose, Latin Hypercube Sampling (LHS) was carried out. Based on the provided inputs, simulations are carried out by ABAQUS with the user-defined subroutine. Later on, to determine which simulations are close to the experimental data, the root mean squared error (RMSE) approach is utilized as an error function. After getting all these data, a 3D surface plot is generated between the error function and the two most important parameters which are determined via MSA. At this stage, polynomial regression is performed. After creating the surface plot, a well-known optimization algorithm, called Particle Swarm Optimization (PSO) takes place, and do so, the parameter calibration process can be carried out automatically.

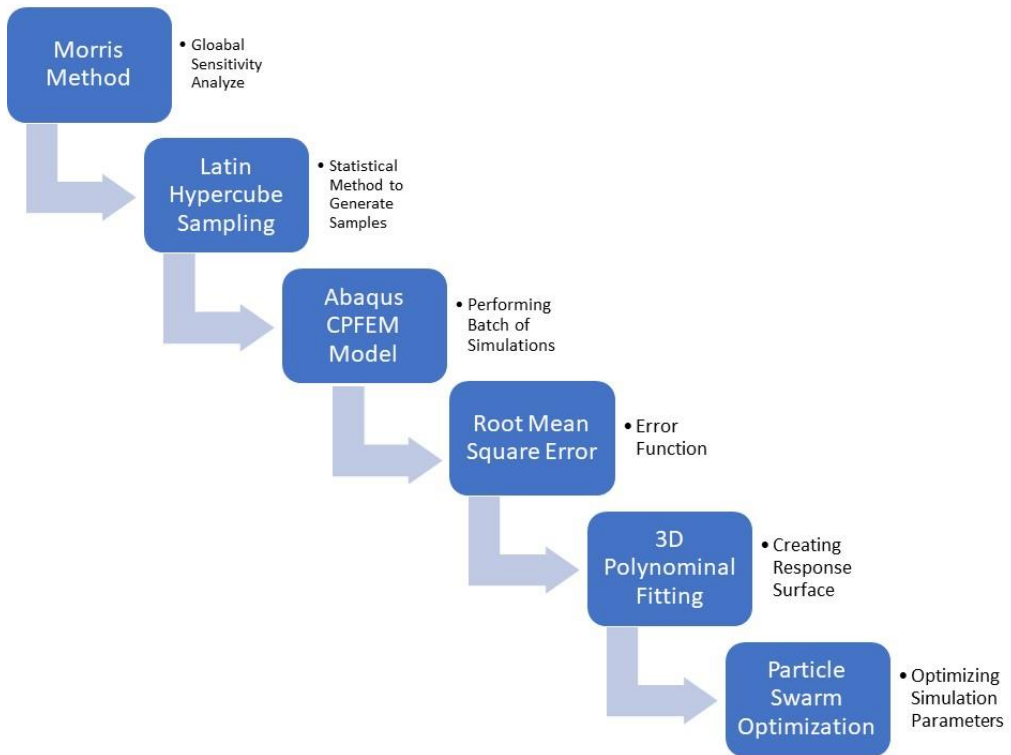


Figure 11: Flowchart of the performed methods and algorithms for the first model.

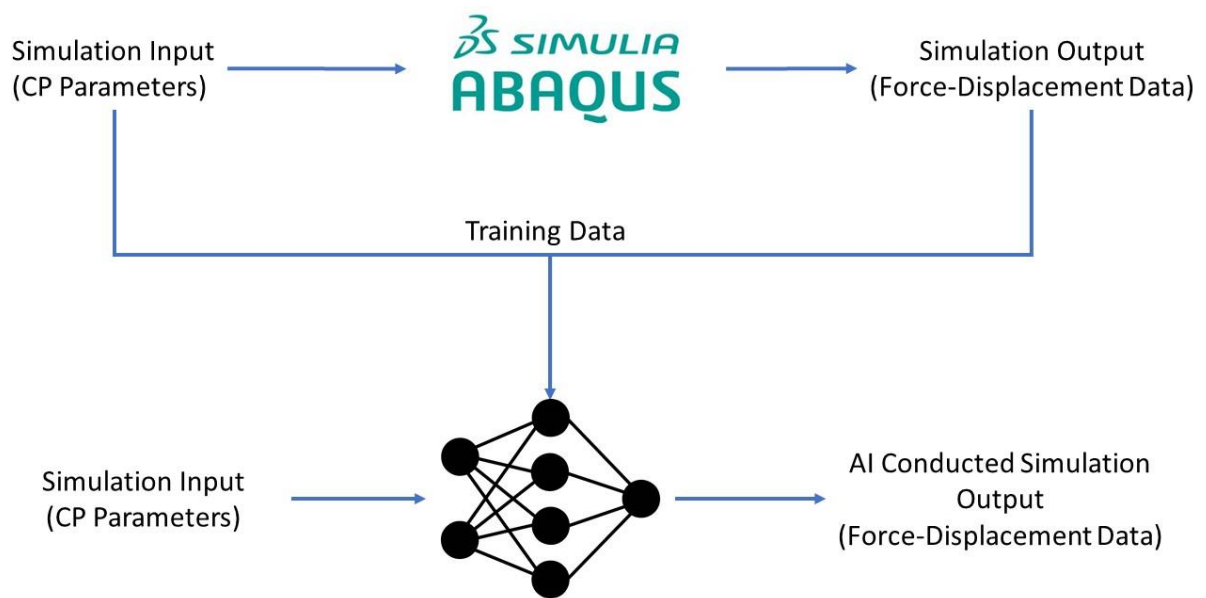


Figure 12: Simple workflow of the AI model.

The second model (Figure 12) requires fewer steps but more data. Just like the first approach, the input data set should be created via LHS and simulated in ABAQUS. Then based on the input data set and simulation outputs AI training starts. In the end, 10.000 dummy simulations will be created and for a given displacement and simulation data AI model predicts the Force data. These simulations are called AI Conducted Simulations (AICS). Between these AICS the ones which show better fitting to the experimental data will be chosen and submitted to the Abaqus CPFEM model to evaluate CP calibration.

After this broad overview, each methodology will be explained in the next sections for providing a rough theoretical backbone.

3.5.1 Response Surface Methodology

Response surface methodology was first introduced by George E. P. Box and K. B. Wilson in 1951 (32). It is a statistical model that helps the identification of the interaction between explanatory variables and response variables. RS can be used for the relevant objectives:

- Determining optimal parameters for a process
- Troubleshooting false or weak points of a process
- Making a process more robust so that external influences cannot affect it

With the aim of creating a response surface, firstly, the x and y-axis should be determined via Morris Sensitivity Analysis. The defined two most important variables are subjected to the x and y axes. The z-axis is determined as the error function. For the purpose of being computationally efficient, a modified Latin Hypercube Sampling Algorithm (33) is used to derive input data. Then with the help of polynomial regression, the response surface is created. Finally, optimization can be finalized via PSO algorithm. The mentioned steps for the RSM (Figure 11) and their scientific concepts will be explained as follows.

3.5.1.1 Morris Sensitivity Analysis

CPFEM models are in general numerically complex and the computational evaluation is highly expensive. To make it computationally more efficient, reducing the number of input factors (parameters) is highly practical. To do so, the factors should be sorted by their importance and the model can be evaluated with the most important

parameters. So the arisen question is: "Which factors among the many potentially important ones – are really important?" (34). To answer this question, in 1991 Max D. Morris came into the scene with his factorial design (35). The main purpose of the method is to determine which factors have a strong effect and which are negligible, linear, and additive, or non-linear or involved in interactions with other parameters (36). For that purpose, the algorithm changes one-factor-at-a-time and it is, therefore, possible to measure, one by one, the "elementary effect (EE)" of each parameter on the output, and finally determine the impact of all of them on the output. Each model input X_i ($i = 1, \dots, k$) is assumed to differ in the space of the input factors over selected p levels. Therefore the testing area, Ω , is a p -level and k -dimensional grid. The factors, on the other hand, are considered to be distributed uniformly within the range of [0, 1] and then converted from the unit hypercube into their actual space of distribution. The EE of the i th input factor on the model is calculated as follows for a given value of \mathbf{X} :

$$EE_i(\mathbf{X}) = \frac{f(X_1, \dots, X_{i-1}, X_i + \Delta, X_{i+1}, \dots, X_k) - f(\mathbf{X})}{\Delta} \quad 20.$$

Where Δ is a perturbation value which is determined from $\left\{\frac{1}{p-1}, \dots, 1 - \frac{1}{p-1}\right\}$

Following, two sensitivity measures μ and σ which stand respectively for the mean and standard deviation of $EE_i(\mathbf{X})$ are calculated. The higher the μ ratio, the greater the effect of the respective parameters on the model's output value. The higher the value of σ , the greater the relationship between a given parameter, and other parameters. Therefore the influence of a certain parameter on the performance of the model is nonlinear.

To be clear, as an example let the dimensional input space $k=2$, the level of grid $p = 5$, the value of $\Delta = 1/4$, and there are 20 elements for each F_i . The five-level input trajectory is represented in **Figure 13**. The horizontal and vertical arrows signify the 20 EE relative to x_1 and x_2 respectively. Campolongo et al. (36) took into account the absolute values of the elementary effect which is called G_i . So in order to find out the effect of the i 'th input factor on the result, both G_i and F_i distributions should be taken into account. Here, the most important sensitivity measure comes out, μ^* , which represents the mean of the distribution G_i , and the standard deviation of the distribution F_i is called σ . μ^* is used for determining the overall influence of the input factor on the output whereas σ is used for determining the factors that are in interaction

with other factors or has a non-linear effect on the output. It should be considered that when Morris first proposed this method, only the mean, μ , and the standard deviation, σ , of the F_i distribution was being calculated. However, this method contains a remarkable disadvantage, if μ is negative which occurs if the model is non-monotonic, the sensitivity analysis cannot be done correctly because some effects can cancel each other out. On the other hand, Morris suggested to combine these two sensitivity parameters on a graph and the point which has the highest μ and σ has the highest importance, and points which are close to the origin can be neglected because they have less effect on the output.

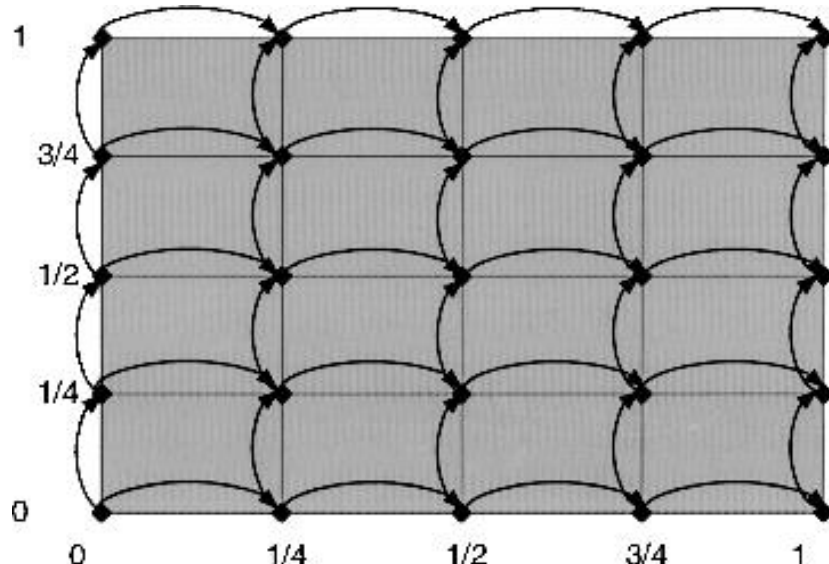


Figure 13: Trajectory in the input factor space for $k=2$, $p = 5$, $\Delta = 1/4$. (34)

For better understanding, a case study is provided (37). In that article, hydrothermal coupling parameters of the embankment dam are analyzed using the thermal monitors. In total there are 7 parameters and 10 monitors and for each monitor, Morris sensitivity analysis is applied. Finally, results can be seen in **Figure 14**. It can be seen that the K_s parameter which stands for the hydraulic conductivity has almost all the time the highest deviation and mean value which makes it the most important and effective parameter. So if an optimization wanted to be carried out, this parameter would be the starting point.

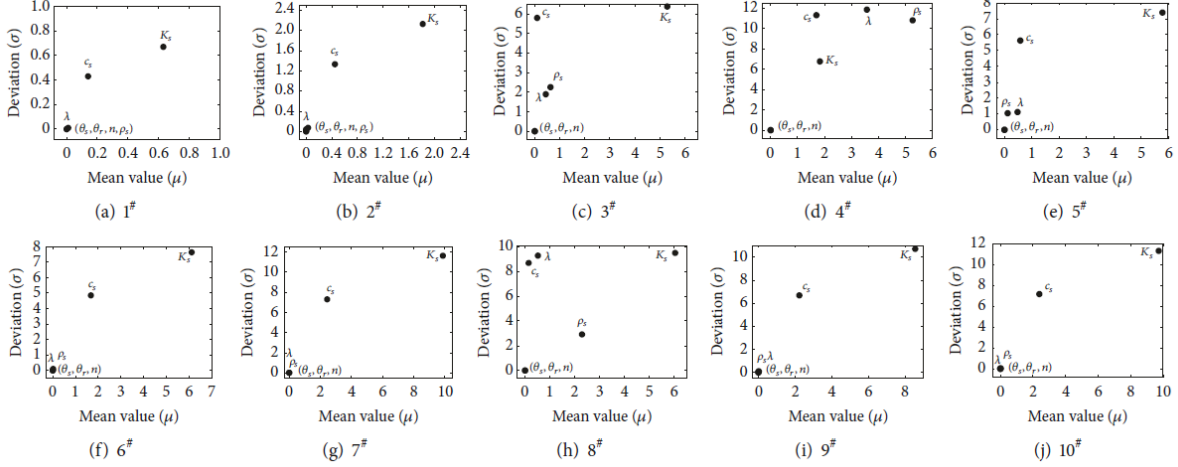


Figure 14: Morris sensitivity results for all the monitoring points. (37)

3.5.1.2 Latin Hypercube Sampling

LHS is a widely used sampling method in the fields of designing computer experiments, uncertainty analysis, adaptive metamodeling (38, 39). The main aim is to achieve better space-filling property, robustness, and convergence character in order to facilitate high computational efficiency. To understand how it can be built **Figure 15** provides a good example. There are two variables X_1 and X_2 respectively and both of them are cut into n sections and creating a grid. Here, n stands for the number of sampling points and for each section only one data point can be mentioned. The next data point can be situated neither in the same column nor the same row. Thus a better-distributed input data set can be achieved. However, the distribution of data points can be different for different LHS criteria. In this work, the enhanced stochastic evolutionary-based LHS algorithm is used due to its optimized design, the distribution of the input data points are better in terms of space-filling property. (33)

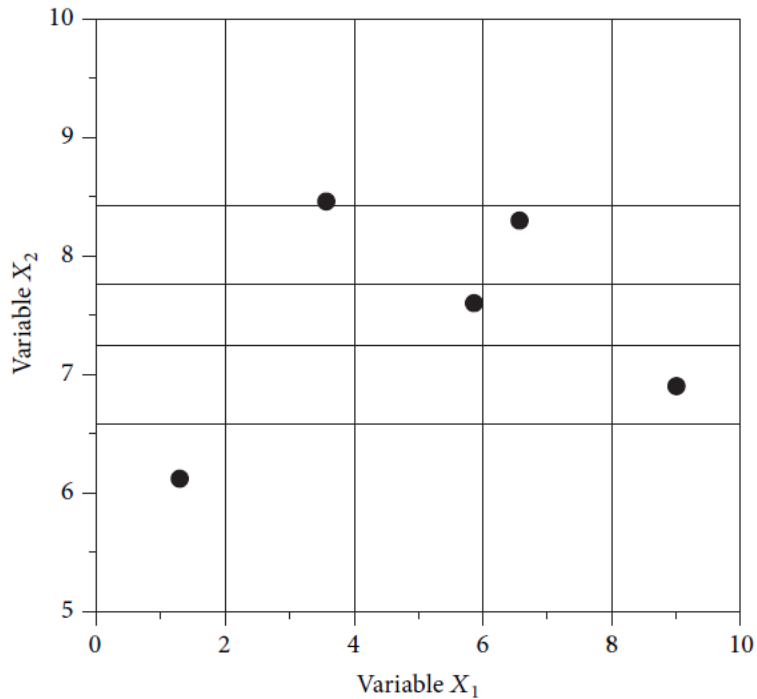


Figure 15: A simple demonstration of the LHS. (40)

3.5.1.3 Root Mean Square Error

The Root Mean Square Error (RMSE) is a widely used performance evaluation tool which in this case, evaluates the performance of the simulation predicting the force-displacement data in comparison with the experimental data. High RMSE value stands for inaccurate results and vice versa. RMSE can be expressed as:

$$\sqrt{\frac{1}{N} \sum_{k=1}^N (y_k - \hat{y}_k)^2} \quad 21.$$

where y_k and \hat{y}_k are respectively actual and predicted force-displacement data points. Finally, N is the number of data points (41). In this work, this approach is used for evaluating curve fitting properties.

3.5.1.4 Polynomial Regression

There are different types of regression analysis and Polynomial Regression is one of them. The relation between the independent input variable x and dependent output variable y is statistically modeled as n^{th} degree polynomial in x . It is also considered as a sort of multiple linear regression. It can be expressed as:

$$y = \beta_0 + \beta_1 x + \beta_2 x^2 + \beta_3 x^3 + \cdots + \beta_n x^n + \varepsilon \quad 22.$$

where ε is an unobserved random error (42). In this work, polynomial regression is used for creating RS.

3.5.1.5 Particle Swarm Optimization

PSO is a nature-based stochastic optimization method that is inspired by the analysis of the behavior of birds searching for food by two American scholars Kennedy and Eberhart in 1995 (43). During their investigation, they find out that suddenly, birds were scattering, concentrating, or changing their directions which seemed at first meaningless. They have realized that the speed of the flock and the distance between birds were constant. Similar behaviors were also detected for the other social animals, such as fishes and ants. It was obvious that there was an information-sharing methodology between these animals. Based on these findings, they persistently simulated the behavior of birds and introduced the PSO concept (44).

In recent years, PSO has been developed and applied to various optimization areas and can be combined with many other existing algorithms. For the convenience of the study, in the algorithm, birds are considered as particles that are looking for an optimal solution (food). Their position can be determined by their search directions and speed. Particles tend to move randomly, however, they are influenced by their ‘personal best position’ (P_{best}) and ‘group best position’ (G_{best}). A particle i can be defined by its current position x_i , current velocity v_i and best-achieved position $P_{best,i}$. At first, the position of the particle is initialized randomly, then, after each iteration, the velocity and position are changed based on P_{best} and G_{best} via the following formula:

$$\begin{aligned} v(k+1) &= v(k) + c_1 \cdot rand() \cdot [P_{best}(k) - present(k)] \\ &\quad + c_2 \cdot rand() \cdot [G_{best}(k) - present(k)] \end{aligned} \quad 23.$$

$$present(k+1) = present(k) + v(k+1) \quad 24.$$

where $v(k)$ is the velocity of the particle, $present(k)$ is the current position of the particle, c_1 and c_2 are learning factors and should be bigger than 0, $rand()$ is a random number between [0,1]. **Figure 16** demonstrates the two-dimensional illustration of particle i . It shows how G_{best} and P_{best} influences the direction and the velocity of the particle over the iteration.

Shortly, the PSO algorithm can be defined in 5 steps (see **Figure 17**):

1. Initialize the parameters: The position and the velocity of the particles should be initialized to the random numbers in the search space.
2. Evaluate the particle's position: Determine the particle's position via using a fitness function.
3. Update the optimal position: Compare the fitness value of the previous step with the particle's current P_{best} and adjust new P_{best} if the new fitness value is better. Compare all P_{best} values and update G_{best} if it is necessary.
4. Update the particle position: Use **Eq. 23-24** in order to update the particle's velocity and position.
5. Termination conditions: Repeat all processes from step 2 if the termination condition is not met, otherwise terminate the algorithm.

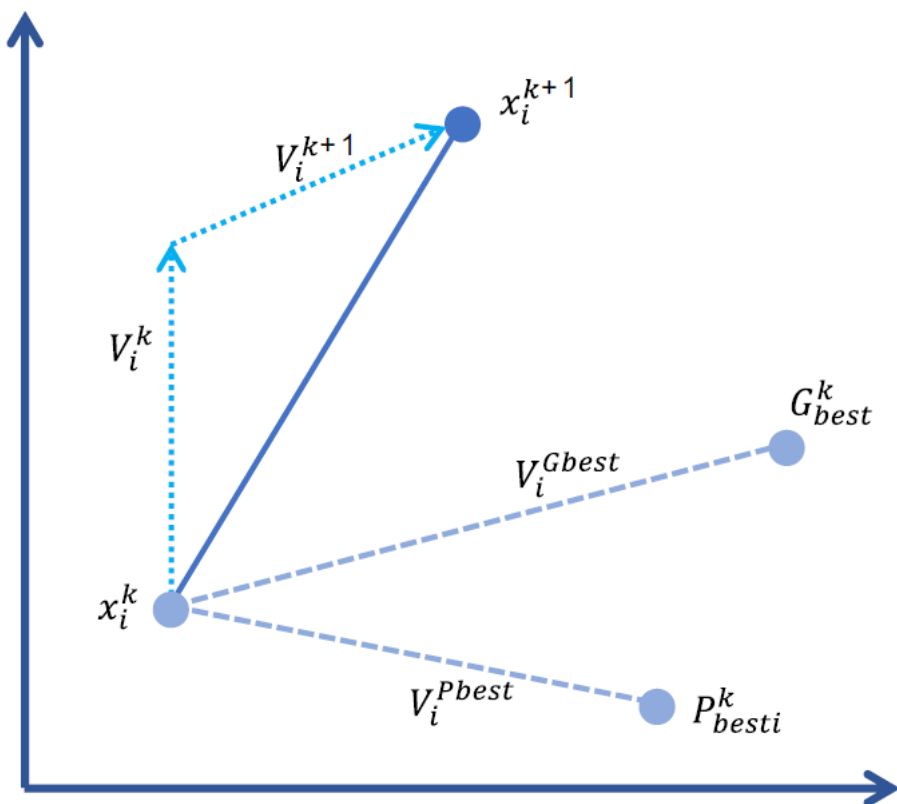


Figure 16: Demonstration of the position and velocity vectors of particle i after one iteration from k to $k + 1$. (45)

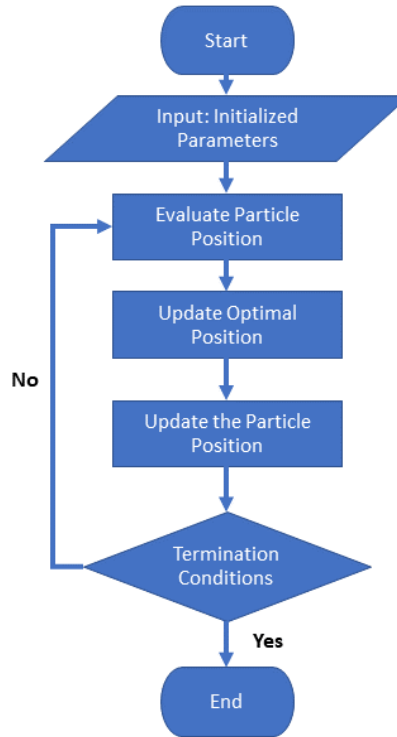


Figure 17: The algorithm behind the PSO (44).

3.5.2 Machine Learning

In the last two decades, Machine Learning (ML) has become one of the mainstays of information technology and a very important, but typically secret, part of our lives. As ever-increasing amounts of data become available, there is a good reason to believe that smart data analysis will become even more widespread as a necessary ingredient for technological progress (46). It is a field focused on building algorithms which make data-based predictions. The aim of a machine learning task is to identify (learn) a function $f: X \rightarrow Y$ that maps the input domain X (of data) to the output domain Y (of possible predictions) (47). ML methods are historically classified into three specific categories:

- Supervised Learning: Example inputs and their desired outputs are introduced to the machine and the aim is to learn a general rule that maps inputs to outputs.
- Unsupervised Learning: The learning algorithm is not given any labels, allowing it to find order in its data on its own.

- Reinforcement Learning: A computer program comes into contact with a dynamic environment in which it has to accomplish a certain objective. As it navigates its problem space, feedback is given to the system which is similar to awards, which it is seeking to optimize. (48)

There are different types of functions that are chosen from various function groups, depending on the type of learning algorithm used. In this work, deep learning methodology is preferred to carry out supervised learning.

Deep learning is part of a larger family of methods in machine learning, focused on artificial neural networks (ANN) (49). As can be seen in **Figure 18** an artificial intelligence (AI) model is composed of three types of layers. These are the input layer, hidden layer, and output layer. If a model includes more than one hidden layer this model is called “Deep Learning Neural Network” and in each label, there are single or multiple nodes or the so-called “Perceptrons” (50).

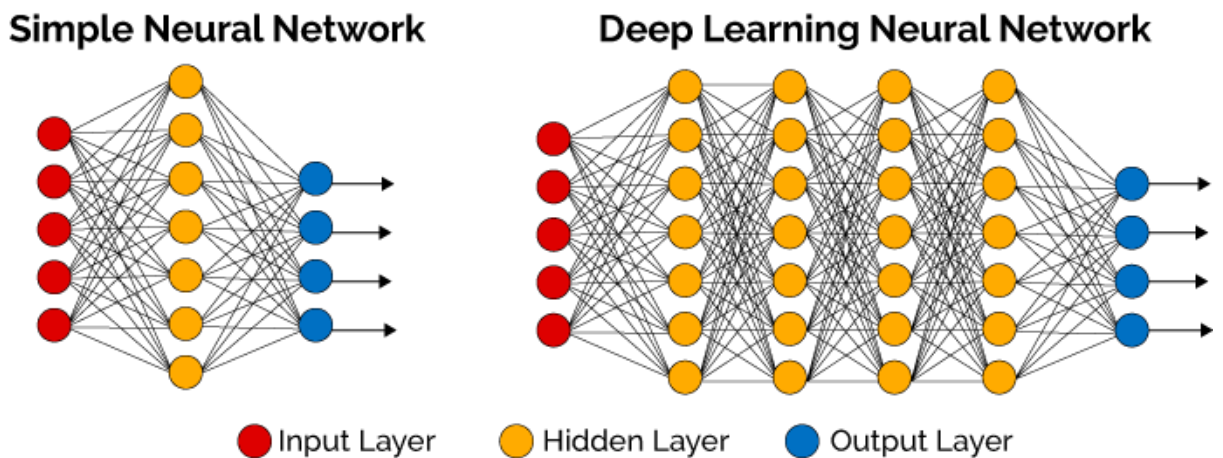


Figure 18: Representation of a deep learning model. (50)

Perceptron is an algorithm used for creating a neural network and the name “Artificial Neural Network” is a multilayer perceptron. It is an algorithm used for supervised learning to linearly classify the given data.

As it is seen in **Figure 19** they consist of 4 main components which are:

- Input values
- Weights and bias
- Net sum

- Activation function

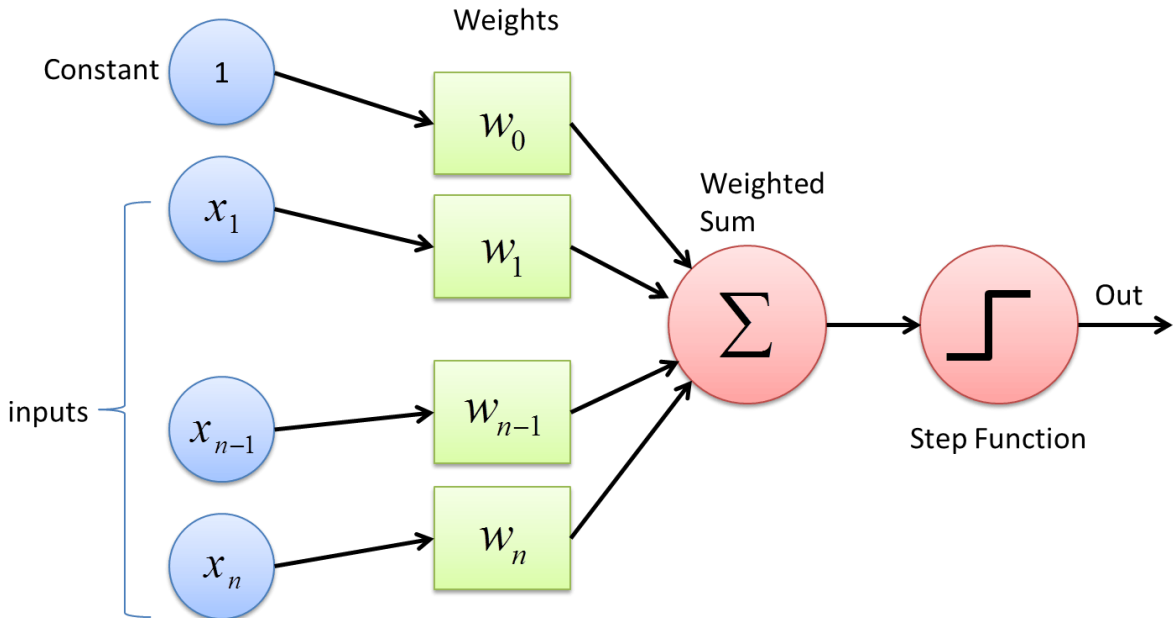


Figure 19: Graphical representation of the Perceptron Algorithm. (51)

The cycle starts by taking and multiplying all the input values by their weights. These values are then added together in order to create the weighted sum. Then the weighted sum is applied to the activation function which produces the output of the perceptron. The activation function plays an integral role in ensuring a mapping of the output between necessary values such as (0,1) or (-1,1). Based on the output value, the weights and biases are updated (52).

4 Experimental Procedure

4.1 Materials Setup

In the previous section, the thermomechanical routes of DP and PL steels are explained and in this section, the influence of these applied processes and chemical compositions on the microstructure and phase transformation is covered utilizing figures that are collected from the literature.

4.1.1 Dual Phase Steel

DP steel is high-strength steel in which the microstructure consists of ferrite and martensite. They are produced from low or medium carbon steels which in this

case represented with DP800, DP780, and their chemical compositions are tabulated in **Table 3**. Alloying elements contribute to some changes in microstructure due to their influence on Time-Temperature-Transformation behavior (**Figure 20**). Their influence on mechanical properties can be specified as follows (53):

- C: A strong austenite stabilizer as it extends the γ area.
- Mn: Another austenite stabilizer, moreover, it inhibits pearlite formation.
- Cr, Mo: They have similar effects, both of them increase significantly strain hardening, corrosion resistance, and wear resistance of the steel.
- Si, P: They are used for solid solution hardening.
- Ti, Nb: They used for grain refinement and dispersion of carbides precipitates.

Table 3: Chemical composition of DP800 and DP780 (in wt %). (54, 55)

Steel	C	Si	Mn	P	S	Al	B	Ti+Nb	Cr+Mo
DP800	0.1	0.8	2.5	0.05	0.01	0.015-1.0	0.005	0.15	1.4
DP780	0.2	0.8	2.6	0.05	0.01	0.015-1.0	0.005	0.15	1

DP steels are quenched from a temperature above A1 to below A3 (Figure 20) as defined by the diagram of continuous cooling transformation. This heat treatment procedure leads to a microstructure consisting of a soft ferrite matrix with martensite islands as the second phase which can be seen in **Figure 21**. The ferrite phase causes several distinctive properties, like high strength, a continuous yielding behavior, a high work-hardening rate, and better ductility. Martensite, on the other hand, increases the tensile strength. The volume fraction, composition, grain size, and carbon content thus control the overall behavior of DP steels (56).

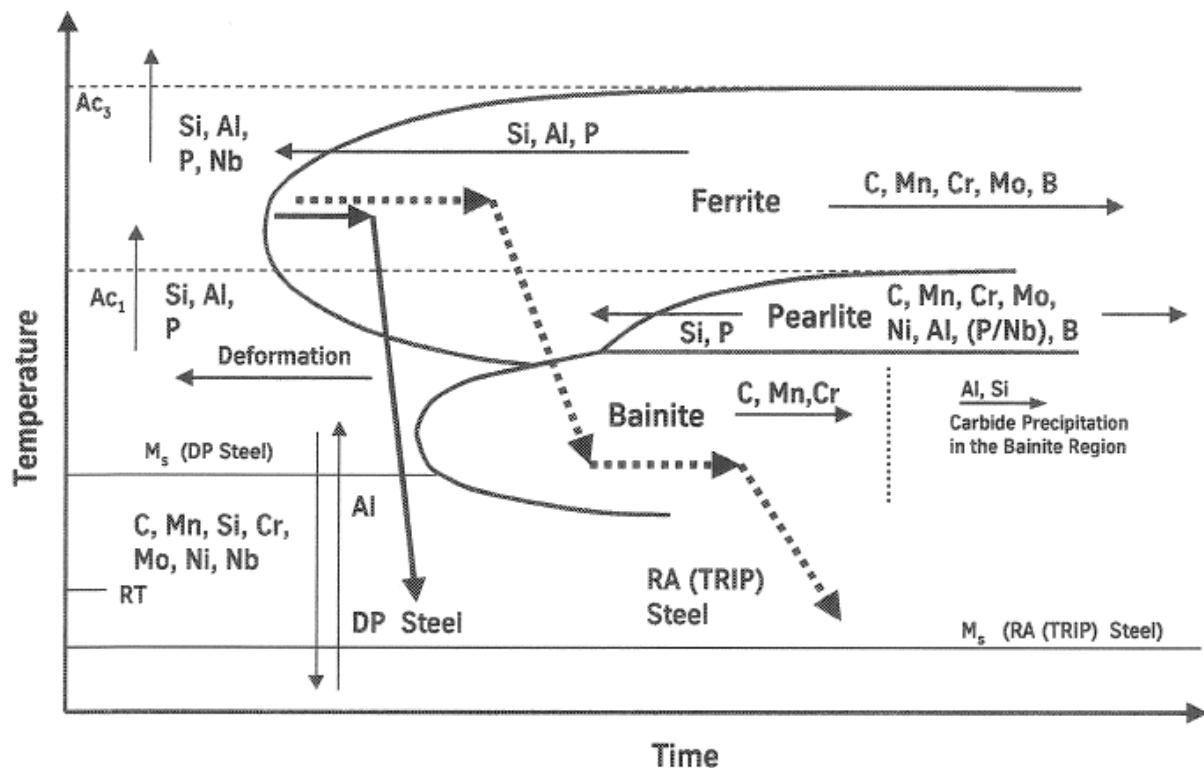


Figure 20: The effect of alloying elements on the TTT diagram. (57)

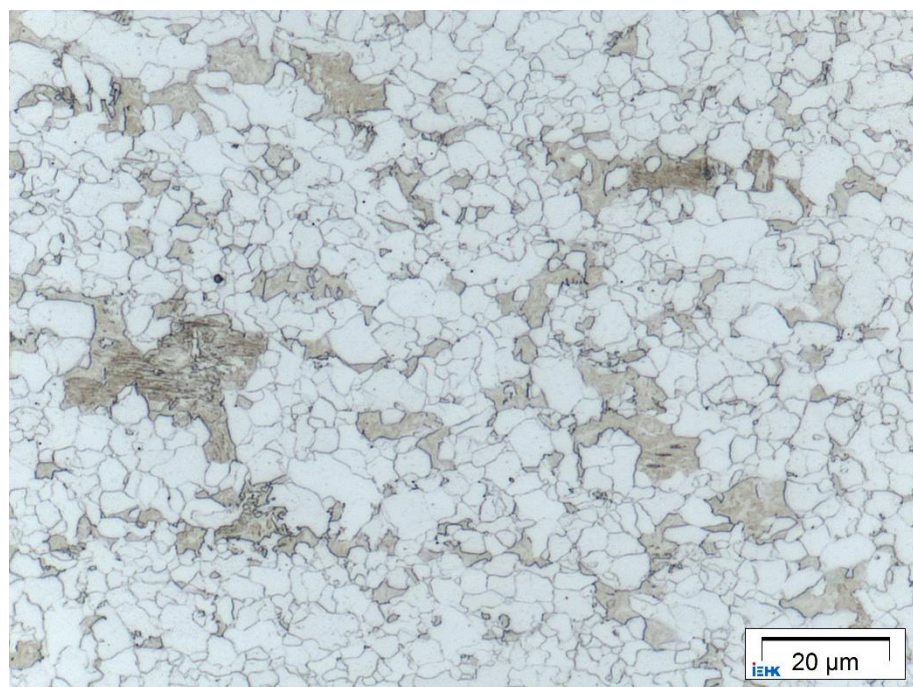


Figure 21: Microstructure of DP780 under the optic microscope.

4.1.2 Pipeline Steel

X65 is high-strength low alloy carbon steel in which the microstructure consists of bainite. It is produced from low carbon steels, and its chemical compositions are tabulated in **Table 4**. While C is mainly contributing to precipitation hardening, manganese slows down the austenitic fall during accelerated cooling and has a solid solution hardening effect. Furthermore, Mn enables the formation of fine-grained bainite by reducing the critical cooling rate required for its formation. Si, on the other hand, is used for solid solution hardening and to suppress cementite formation. Although P in the presence of Cu increases the corrosion resistance of structural steels and has a solid solution strengthening effect, it must be kept as low as possible, just like S, due to its high melting interval and segregation behavior. The alloying element Al is used for deoxidation like Si and Mn. Nickel lowers the critical cooling rate and has a grain refinement effect. In combination with phosphorus, copper increases wear resistance, strength, and hardenability. Cr forms strength-increasing carbides and increases hardenability. Besides their function in thermomechanical treatment, Ti and V are strong ferrite formers.

Table 4: Chemical composition of X65 (in wt %).

Steel	C	Mn	Si	S	Al	P	Ni	Cr	Cu	Nb	V	Ti
X65	0.04	1.4	0.25	0.002	0.04	0.01	0.5	0.02	0.09	0.04	0.06	0.01

Pipeline steels are hot rolled above the critical eutectoid temperature to get a fully austenitic microstructure and then quenched. During the cooling phase, austenite transforms into proeutectoid ferrite and pearlite which can be seen in **Figure 22**. The pearlite is consist of pearlitic ferrite (not proeutectoid ferrite) and cementite (58).

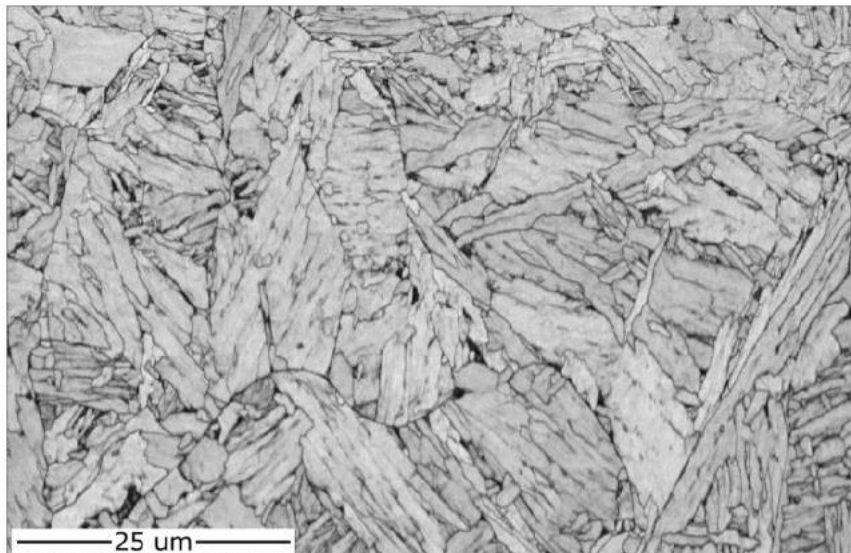


Figure 22: SEM picture of X65 pipeline steel. (58)

4.2 Nanoindentation Setup

In this work, the nanoindentation test was performed on three different steel grades. The procedure has been completed within two main steps with the help of two institutes. Firstly, samples are prepared at the IEHK institute. Secondly, the nanoindentation test was carried out at the MCH institute and all the necessary data was collected. These two steps are explained briefly.

4.2.1 Sample Preparation

The samples that are used for the investigations were taken from rough plates and then cut into pieces. For better handling for the following metallographic preparation, specimens are cold embedded (see **Figure 23**). Then they are ground using ATM polishing machines and SiC abrasive paper. This is done in several grinding stages, which differ in the increasing grain size of the abrasive paper. The sample is then polished with an alumina suspension until the surface of the sample appears flat and scratch-free under the light microscope.



Figure 23: The prepared samples for characterization tests.

4.2.2 Nanoindentation Test

Isotropic quartz glass with a proven elasticity modulus of 72 GPa and Poisson's ratio of 0.17 is evaluated for the calibration of the tip shape of the nanoindenter, which may deviate from its ideal symmetrical shape due to manufacturing tolerances. The Hysitron TI980 Triboindenter, the indenter tip of which has a conical angle of 90° and an indenter radius of 1 μm, is used for material testing as part of this work. The schematic representation of the indenter tip can be seen in **Figure 24**.

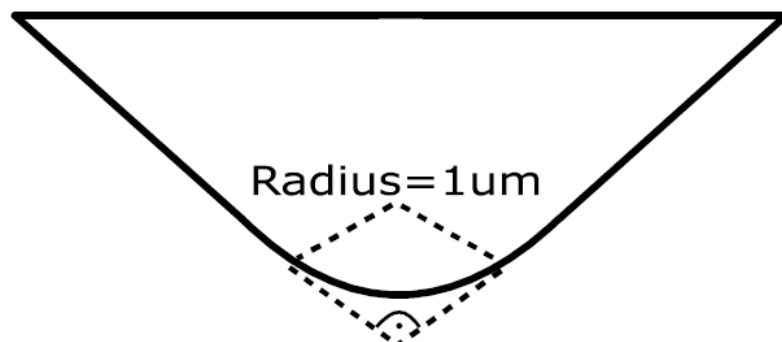


Figure 24: Representation of the nanoindenter tip. (59)

For a qualitative representation of the sample properties, the indentations are created explicitly in grains that have the most varied orientations possible. For grain identification, the Mtex-toolbox is used. In addition, in order to consider a wide variety of material reactions to the load application, grains of various orientations have to be checked. The test parameters can be seen in **Table 5**, however, it should be noted

that these are exemplary values for PL steel and they might differ depending on steel grade.

Table 5: Nanoindentation test parameters.

Test time	407 s
Maximum penetration depth	400 nm
Load time	400 s
Load rate	1 nm/s
Holding time at the maximum penetration depth	2 s
Relief time	5 s

4.3 Simulations Setup

Imputation is an important issue when it comes to data analysis. In this work, the range of the parameters set is determined by conducting the literature review. After determining the parameter ranges a batch of simulations with different quantities was submitted. In total, more than 1000 simulations were conducted in less than 5 months. To achieve this goal, a shell script is written in Unix format for the automation of the simulation process. These two aspects will be explained under this topic.

4.3.1 Simulation Inputs

Due to the quasi-static loading condition, the strain rate effect is not studied in this work, and for that reason $\dot{\gamma}$ and m are determined from the literature (60) and the parameter calibration is performed with 4 remaining parameters. Based on **Table 6** the range of the CP parameters are determined and they are demonstrated in **Table 7**.

It should be taken into account that τ_0 cannot be greater than τ_s for that reason when the input parameter set has generated the difference between these two parameters was taken at least 207 MPa which is found by taking the average difference between τ_0 and τ_s from Table 6.

Table 6: CP parameters that are gathered from literature.

Index	h_0 , MPa	α	τ_0 , MPa	τ_s , MPa	Ref.
1	460	2		420	(60)
2	1518		43.58	203.5	(61)
3			190		(62)
4			280		(62)
5	180	2.25	55	148	(63)
6	1000	2.25	96	412	(64)
7	1000	2.25	95	222	(64)
8	610	1			(64)
9	940				(65)
10	475				(66)
11	555				(66)
12	802				(66)
13	880				(66)
14	500		102.5	410	(67)
15			250	380	(68)
16			214		(69)
17	900	1	110		(70)
18	500		52	400	(71)
19	372	5			(72)
20	1000	2	354	837	(73)
21	180		65	148	(74)
22	300		100	150	(74)
23			113	226	(75)
24			51	400	(76)
25			200		(77)

Table 7: The range of the simulation parameters

Parameter	Min	Max
a	1	5
h_0 , MPa	180	1518
τ_0 , MPa	43	354
τ_s , MPa	148	837

To create an input dataset based on a given range (see Table 7) a Python Surrogate Modeling Framework that contains the LHS method has been used (78). To demonstrate the output of the LHS method a 2D graph with 200 data points created (see **Figure 25**). It is seen that LHS with Enhanced Stochastic Evolutionary algorithm does a great job in terms of space-filling.

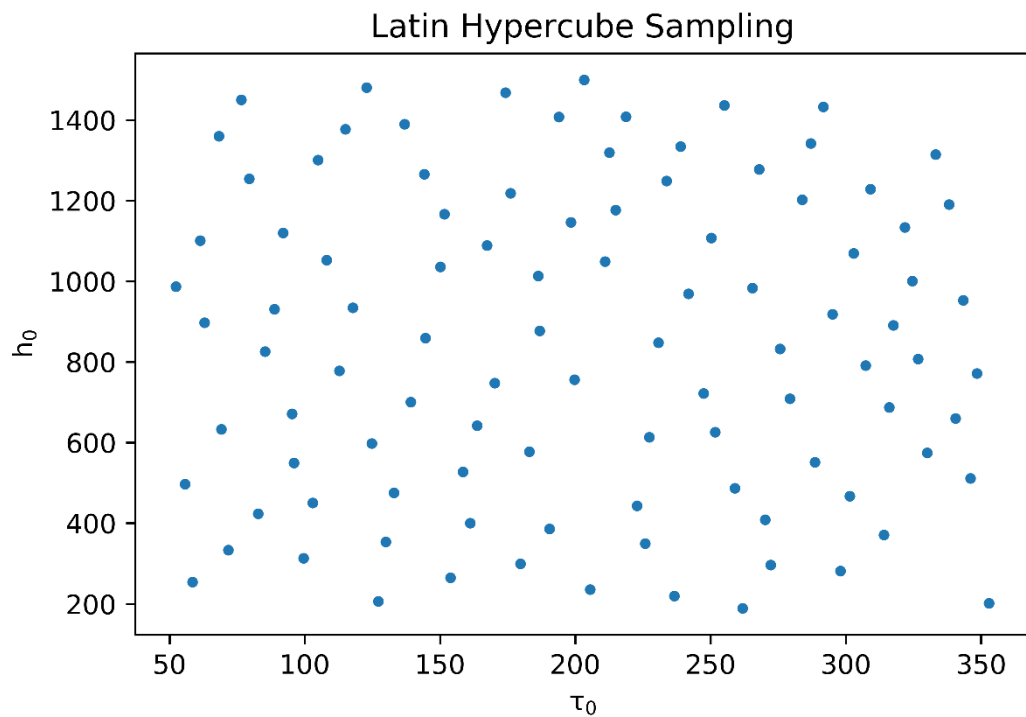


Figure 25: Illustration of the generated data points via LHS.

4.3.2 Automating Simulation Process

In this project, all the simulations are carried out with Abaqus FEA 2019. In order to automate the simulation procedure and enhance the quality of all simulations, 2 shell scripts and 3 python scripts have been coded which are available on the RWTH-Git server via this <https://git.rwth-aachen.de/orkunkaragullu/master-thesis>. The main automation script which is called “control.sh” submit simulations based on the desired number. The implemented automation algorithm is explained via a flowchart in **Figure 27**. For this Project this number set to 43. On the Putty terminal when the “squeue -u user” command is entered, it shows the jobs that are submitted by the user (see **Figure 26**). In addition to this, when the “squeue -u user|wc -l” command is written, it shows how many lines does the output of the “squeue -u mj890808” contains. As an example in Figure 26, there are 5 lines. The first line is the job features like their name and status, the second line is the “counter” script which submits the automation script every three hours. Three hours is chosen in order to process the log file of the automation script otherwise, it cannot be opened due to its high size. The third line is the automation script. It checks all the simulation folders if one simulation is finished, it submits the next simulation. Furthermore, it runs another python script that checks whether the finished simulation is successfully completed or not. If not the script erases all the output files and sends it back to the input folder. And the fourth line is the Abaqus simulation and the fifth line is the “Abort” script which checks the progress of the simulation. If for some reason the simulation runs slowly, the script stops the simulation, erases all the output files, and resubmit the simulation. So with the given number of 43, it is ensured that in total 20 Abaqus simulations run parallelly. Simulations were performed with computing resources granted by RWTH Aachen University under project thes0839.

Figure 26: The display of the Putty terminal

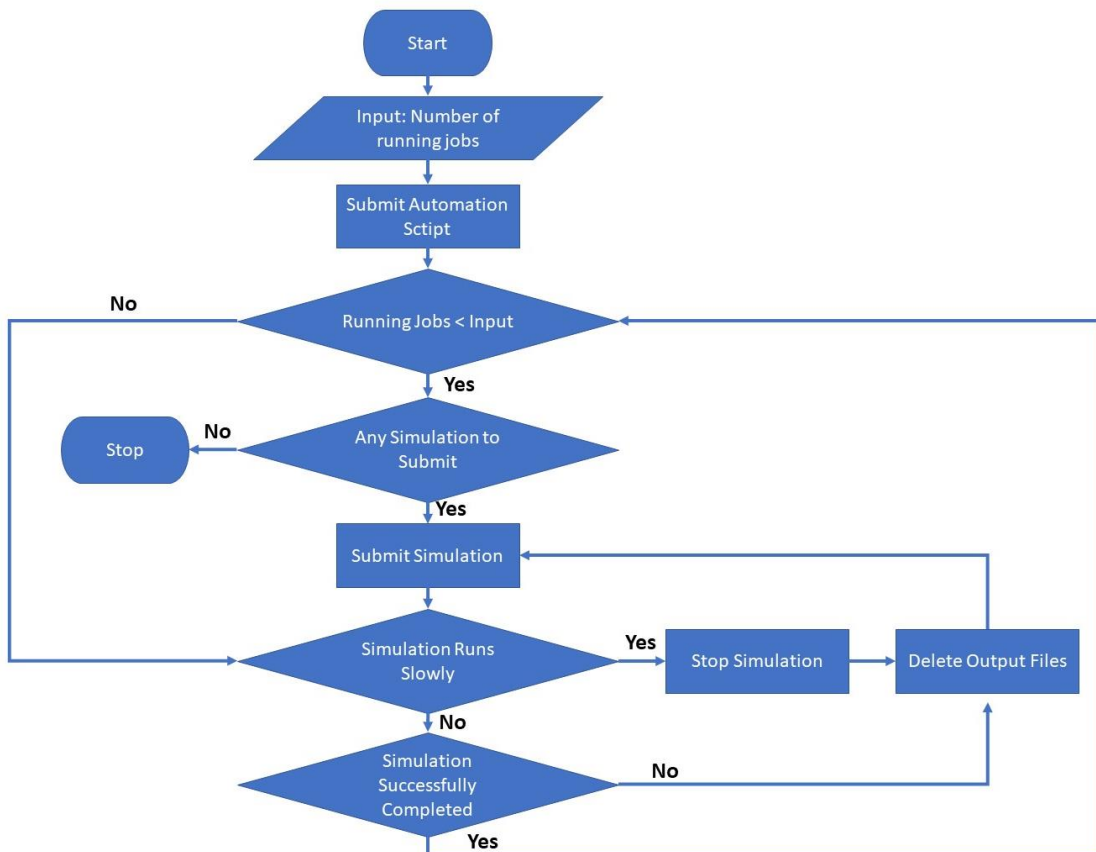


Figure 27: Flow chart of the automation script.

4.4 Artificial Intelligence Model

After running all the simulations with the determined simulation parameter set. Force-displacement data was extracted automatically via Python script using Abaqus Framework. In total, around 63000 data points have been extracted from 500 simulations that are used for AI training. **Figure 28** shows the steps that are followed during the development of the AI model. First of all preprocessing of the AI input data had to be conducted. To show the structure of the AI input dataset **Table 8** is prepared. There are 12 rows and six columns, the first six belong to one simulation and the last six rows belong to another one. It can be seen that in this table for one simulation parameter set 6 force-displacement data are obtained. So, the rate between the number of simulation parameters set and force-displacement data is 1/6. In reality, this rate is around 1/126 which is not ideal for an AI model. For that reason instead of determining simulation parameters set directly from force-displacement data which means 2 input and 4 output parameters, only Force is taken as output and all the rest is taken as input. After preprocessing the AI input data, 30 % of the data set is separated as the test set and the rest 70 % is the train set. Test set will be used for the evaluation of the model at the final stage.

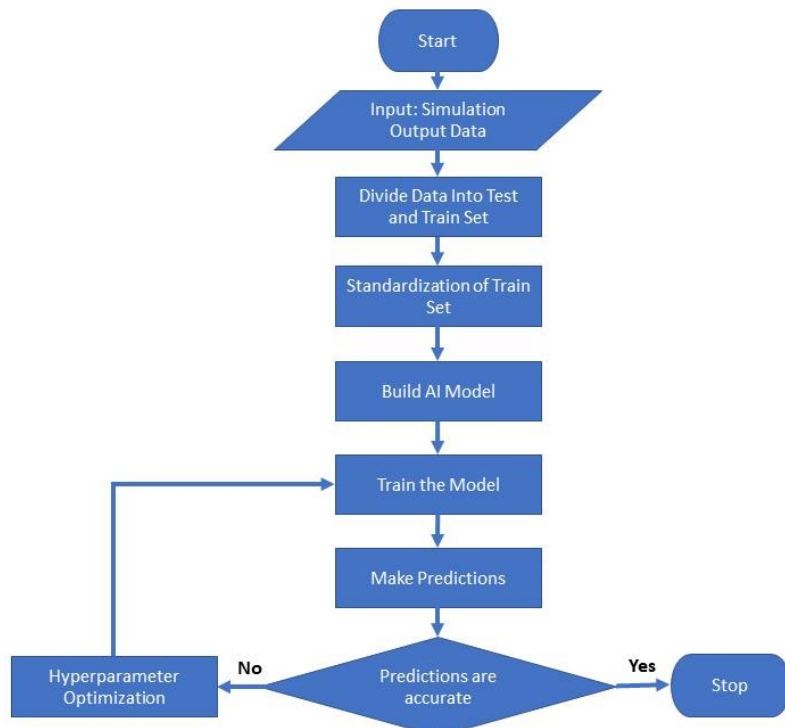


Figure 28: Workflow of the AI model.

Then apart from the output column (Force) and test set, all the data is standardized based on the following equation:

$$x' = \frac{x - \bar{x}}{\sigma} \quad 25.$$

Where \bar{x} is the mean value of x vector and σ is the standard deviation. The main purpose of doing so is to put all the data in the same range. As an example the range of h_0 is between 180 to 1518 and a is from 1 to 5. In this example h_0 outweighs a due to its higher range however, when both features are standardized around 0 with a standard deviation of 1, this problem won't occur. On the other hand, the test set should not be scaled with the training set because that could change the mean value \bar{x} which is not desired. The model should have no idea about the test set. After scaling the train set, the \bar{x} and σ value of the training set should be used for scaling the test set.

Table 8: Some data points from 2 different simulations separated with grey and blue.

Displacement [mm]	Force [N]	τ_0	τ_s	a	h_0
0.000141	0.003452	352.95	584.58	1.26	733.64
0.000144	0.003492	352.95	584.58	1.26	733.64
0.000147	0.003583	352.95	584.58	1.26	733.64
0.000151	0.003749	352.95	584.58	1.26	733.64
0.000154	0.003914	352.95	584.58	1.26	733.64
0.000158	0.004102	352.95	584.58	1.26	733.64
0.000263	0.003798	191.87	365.42	2.62	605.3
0.00027	0.003858	191.87	365.42	2.62	605.3
0.000279	0.003942	191.87	365.42	2.62	605.3
0.000286	0.004011	191.87	365.42	2.62	605.3
0.000291	0.004054	191.87	365.42	2.62	605.3
0.000296	0.004105	191.87	365.42	2.62	605.3

Finally, the AI model is generated via Python with the TensorFlow framework (version 2.2.0). As it is mentioned before, in this work the AI model is a multilayer perceptron model, consists of 4 layers, can be seen in **Figure 29**. The first layer is the input layer and containing one node per input parameter. The second and third layers are hidden layers and containing 64 and 32 nodes respectively. Finally, the fourth layer is the output layer which predicts the Force value. The activation function is chosen “Rectified Linear Unit”, the loss function is “mean squared error” and the optimization algorithm is “Adam”. In order to avoid overfitting, validation, and training losses are recorded and if validation loss gets significantly higher than training loss, the training phase stops automatically. After creating the model next step was training and optimizing.

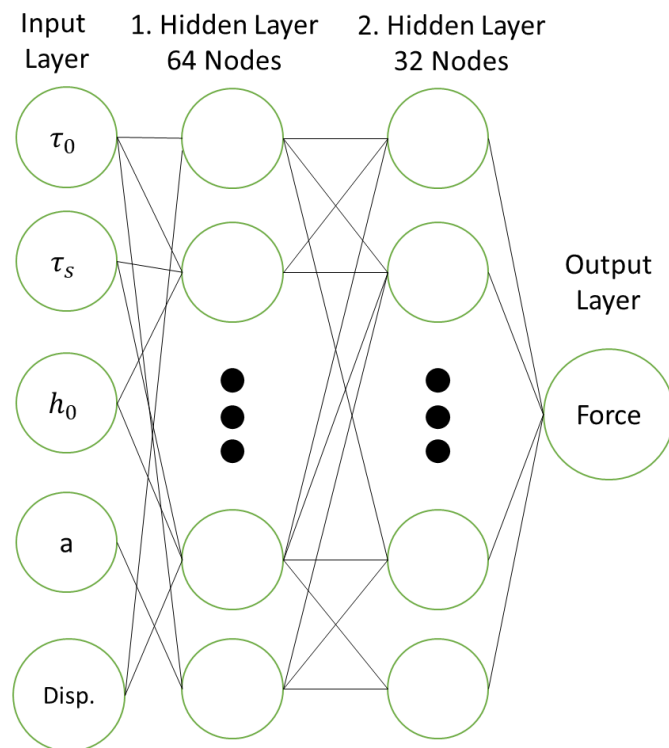


Figure 29: Architecture of the AI model.

A grid search approach is used for hyperparameter optimization and for each parameter set 10 models were created and their average r^2 score (coefficient of determination) is used for the evaluation of the model.

r^2 score can be explained as follows:

$$\bar{y} = \frac{1}{n} \sum_{i=1}^n y_i \quad 26.$$

where \bar{y} is the mean of the real or observed data. Then the variability of the data set should be measured via sums of squares SS_{tot}

$$SS_{tot} = \sum_i (y_i - \bar{y})^2 \quad 27.$$

Then the residual sum of squares SS_{res} have to be measured as:

$$SS_{res} = \sum_i (y_i - f_i)^2 \quad 28.$$

where f_i is the predicted data and finally, r^2 score can be represented as:

$$r^2 = 1 - \frac{SS_{res}}{SS_{tot}} \quad 29.$$

In the best case, the predicted values exactly match the observed values, which results in $SS_{res} = 0$ and $r^2 = 1$. If $r^2 = 0$ it means the model always predicts \bar{y} and if $r^2 < 0$ the model has the irrelevant predictions (see **Figure 30**).

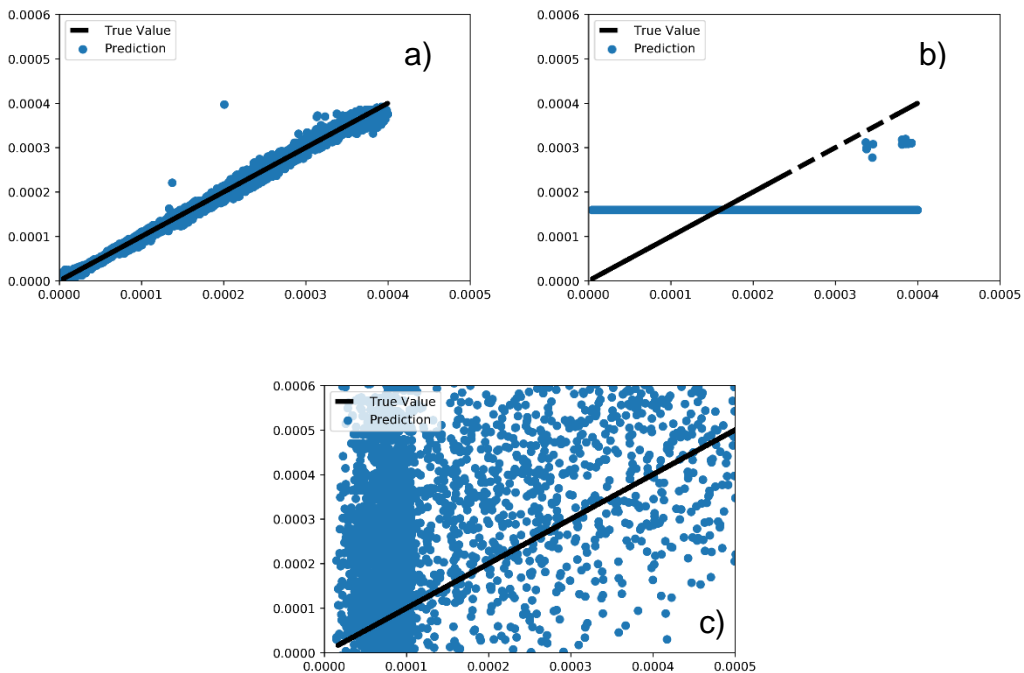


Figure 30: 3 Different models with r^2 scores respectively a) 0.9967 b) 0.0058 c) <0.

After training and optimizing the AI model it is time to begin the optimization phase. Now the AI model can mimic Abaqus CP analysis. So, LHS is used to create 10.000 input data set for dummy simulations that contain 4 unique simulation parameters and displacement data from 0 to 0.0004 mm. Based on these 5 parameters the AI model predicts Force for each Displacement data and in the end, a force-displacement curve is achieved. This procedure is called AI Conducted Simulation (AICS) and processing 10.000 AICS takes only a few minutes. After finishing all the AICS the obtained curves are compared with the experimental data (see **Figure 31**). To evaluate their fitting capability a modified RMSE is used because the number of the data points of each curve is not equal. Experimental data consists of 80000 data points where for AICS it is only 1000. So another RMSE script had to be written. For a given AICS data point, firstly the script finds the closest data on the x-axis (Displacement data) and then calculates the difference between these two points based on their y-axis (Force data). After doing this for all the data points, all the AICS are sorted based on their RMSE and a new table is created (see **Table 9**). Based on this table, the first 10 AICS are simulated on Abaqus and the results are once again compared in between.

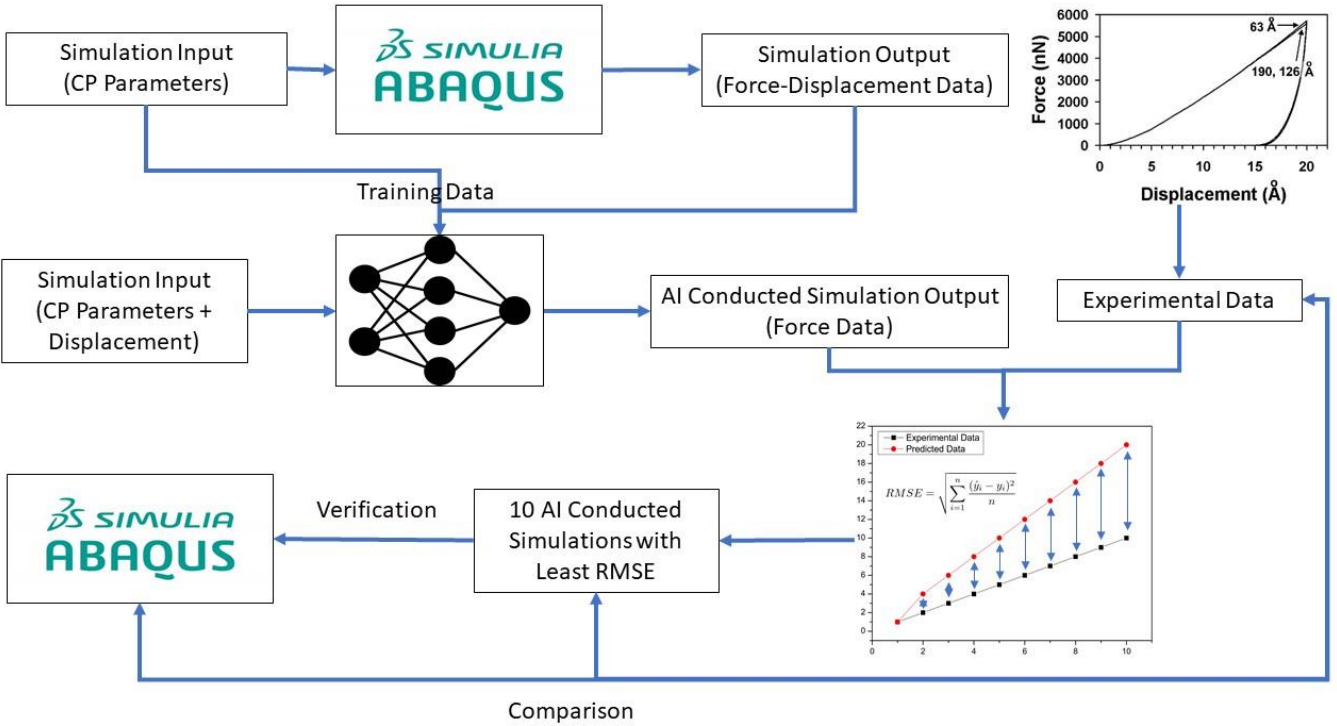


Figure 31: The complete AI optimization workflow.

Table 9: Sorted AICS and parameter sets based on their RMSE.

Files	τ_0 , MPa	τ_0 , MPa	a	h_0 , MPa	RMSE
AICS_2845	56.82	834.66	1.54	1371.99	0.000212
AICS_8085	80.01	804.06	1.35	1115.34	0.000217
AICS_6091	62.96	792.31	1.54	1396.75	0.000225
AICS_8599	73.37	794.81	1.98	1469.27	0.000226
AICS_8580	67.12	824.66	1.27	1260.3	0.000231
AICS_5285	126.47	812.51	1.58	818.74	0.000242
AICS_5046	87.6	816.94	2.31	1485.18	0.000247

4.5 Response Surface Model

The second model is a modified response surface model which is inspired by the commercial robust design optimization tool optiSLang®. It can be said that the model consists of 3 main parts which are sensitivity analysis, exploration, and exploitation. First of all, Morris Sensitivity Analysis took place in order to find out which simulation

input parameters (τ_0, τ_s, a, h_0) have a higher influence on the output. Then parameters are split into two groups based on their importance. The most two important parameters were called “essential parameters” (EP) and would be optimized. The rest were called “inessential parameters” (IP) and stayed constant. The sensitivity analysis was carried out with 100 simulations and the Python SALib framework (version 1.3) was used for pre and post-processing. Once the sensitivity analysis was terminated the 500 simulations which were used for training the AI model were used as a database to determine the IP. For this purpose, the RMSE script was used between experimental data and 500 simulations. The parameters of the simulation which shows the lowest RMSE value was taken and IP was determined from this parameter set. This was the final step of the first stage and then, the exploration stage begins with creating 100 simulations via LHS. It is worth remembering that only EP changes and IP are constant. Then all the simulations were submitted. When they were finished RMSE script was used to find out all the RMSE values of the conducted simulations. Then the simulation parameters and their RMSE values were gathered and represented in a 3D graph as can be seen in **Figure 33**. For that purpose, all the data had to be standardized and 4th-degree polynomial regression was used to identify the surface equation. For the polynomial regression Python NumPy framework (version 1.16.4) and for creating 3D graphs Python Matplotlib framework (version 3.1) was used. The exploration phase is terminated with the creation of the response surface and the exploitation phase starts. PSO was used in order to find out the minima of the surface. The algorithm is implemented to Python from scratch, and parameters are optimized. The number of swarm particles was set to 10 to decrease the chance of getting a local minimum, the iteration was set to 100 and the algorithm was successfully tested on the Ackley function (79). PSO finds successfully the minima and to exploit the area around this point a small batch of simulations was created with LHS and submitted. And then once again simulation results were evaluated via RMSE script. If the results are accurate, then the parameter set of the simulation which has the least RMSE value can be taken. If the results are not satisfying, once again the exploration phase can take place.

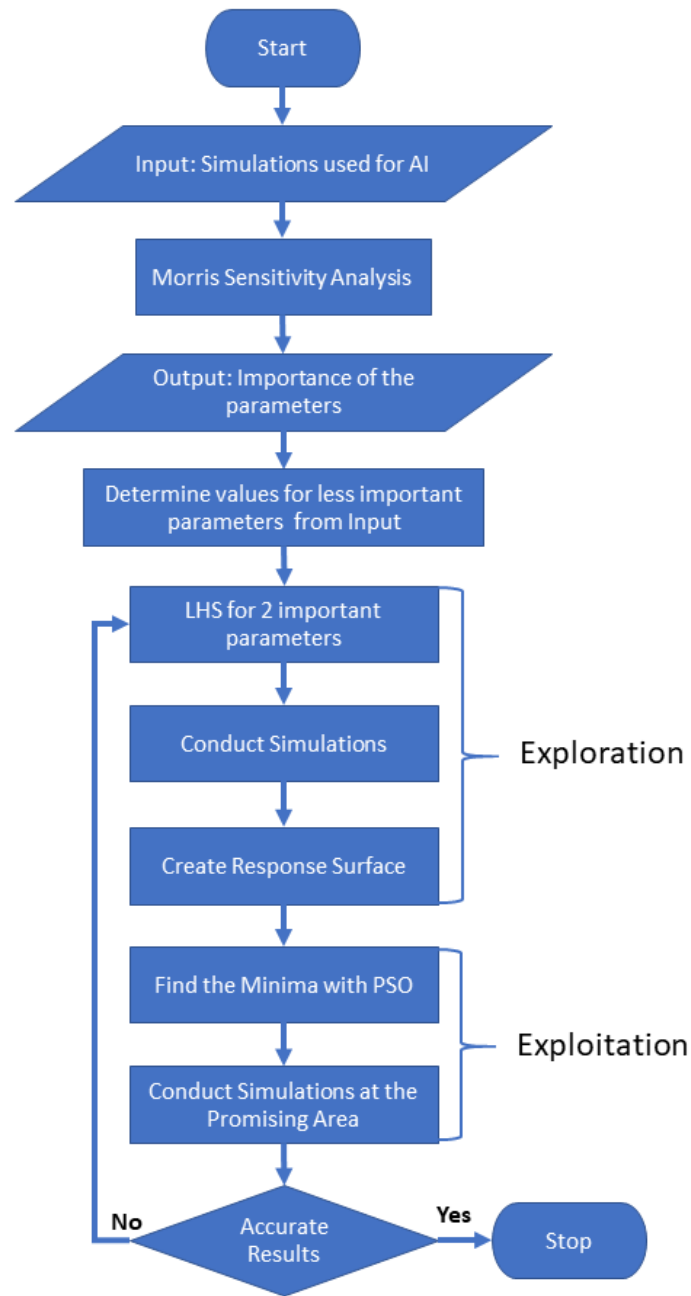


Figure 32: Workflow of the RS model.

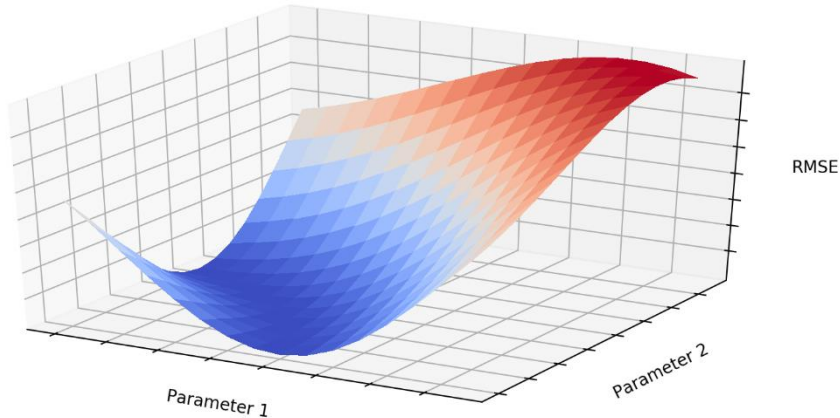


Figure 33: Example of a 3D response surface.

5 Results

In this section firstly, material characterization test results will be shown. Then these tests will be simulated and lastly, CP calibration will be introduced. Before starting this section it should be mentioned that there are 2 different DP steel grades which are DP 780 and DP 800. To create the basics of the two optimization models, a preexist force-displacement data of DP 800 steel was used however, the orientation data was missing so the first evaluated models did not take the orientation parameter into account. After successfully creating the basic models, the next step was making it more complex and for that reason, the orientation data was taken into account for the PL steel. After finding CP parameters of the PL steel, it was planned to analyze DP 780 steel. For that purpose, some microstructure analysis and nanoindentation tests were carried on, however, the calibration of the previous samples consumed all the available computational sources for that reason no more simulations could be submitted and as a result, CP calibration of the DP 780 steel could not be completed and its nanoindentation test results are not analyzed.

5.1 Mechanical Test Results

Nanoindentation tests were carried out on DP 800 and PL steels. The data for the PL steel was driven from previous work (59). In **Figure 34** the EBSD picture of the PL steel can be seen. The band contrast image (see Figure 34a) was created with Matlab and the mtex toolbar with the corresponding color keys. The grains were enumerated from 1 to 4 by their color keys and these numbers serve as the basis for

the following nanoindentation tests. After completing the microstructure analysis, the next step was conducting nanoindentation tests. For all the enumerated grains, at least 2 nanoindentation tests were conducted and demonstrated in **Figure 35**. Figure 35(1-4) represents the enumerated grains that were determined in Figure 34b. Figure 35(a-d) show the areas where the nanoindentation took place, and finally, Figure 35(e-h) demonstrates the same areas after the nanoindentation tests. Moreover, the orientation data of the grains are shown in **Table 10**.

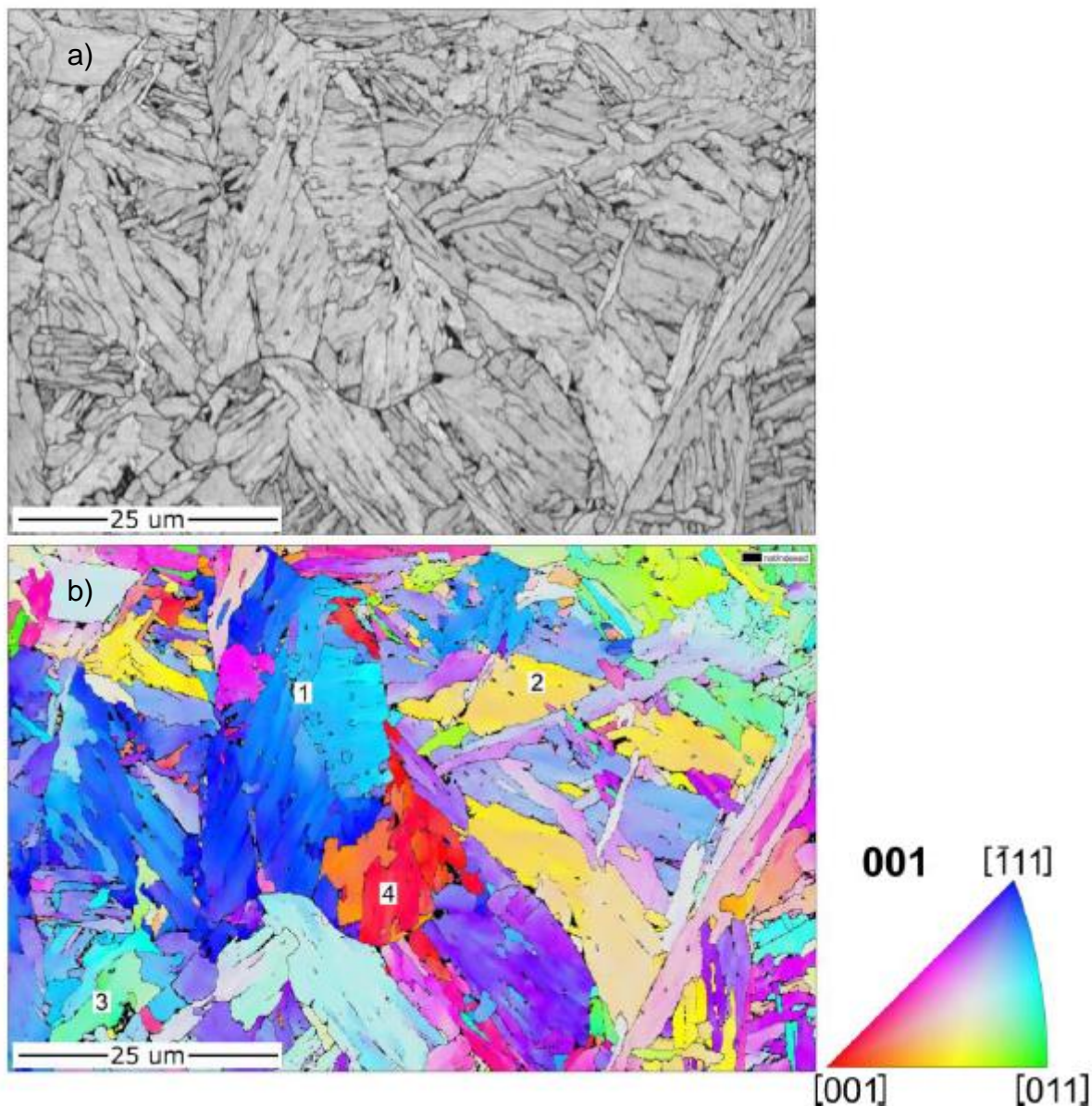


Figure 34: The EBSD picture of the X65 PL steel a) the band contrast and b) inverse pole figure in 001 direction with the color code of the microstructure of grade. (59)

Table 10: Euler angels of the represented grains. (59)

Grain No.	φ_1	θ	φ_2
1	320.70°	129.15°	232.83°
2	56.19°	156.67°	189.91°
3	3.97°	139.90°	195.38°
4	357.16°	172.22°	119.08°

All the gathered data from the nanoindentation test are illustrated in **Figure 36** with their grain numbers. As can be seen in the figure, force-displacement curves within Grain 1 and 2 (see Figure 36a,b) are similar, but when it comes to Grain 3 and 4 (see Figure 36c,d) there is a deviation between the curves. The reason for that significant deviation will be mentioned in the Discussion part. Based on these indentation results, it can be said that Grain 1 and 2 are ideal for calibration, and Grain 1 was chosen for the CP calibration because it exhibits three indentation tests and all of them are compatible.

As it is mentioned before force-displacement data for DP 800 was gathered from a previous experiment and without any characterization feature, optimization models are first constructed on this reference data and then models are optimized based on more reliable data which is gathered from Grain 1. Both reference curves from DP and PL steels are shown in **Figure 37**.

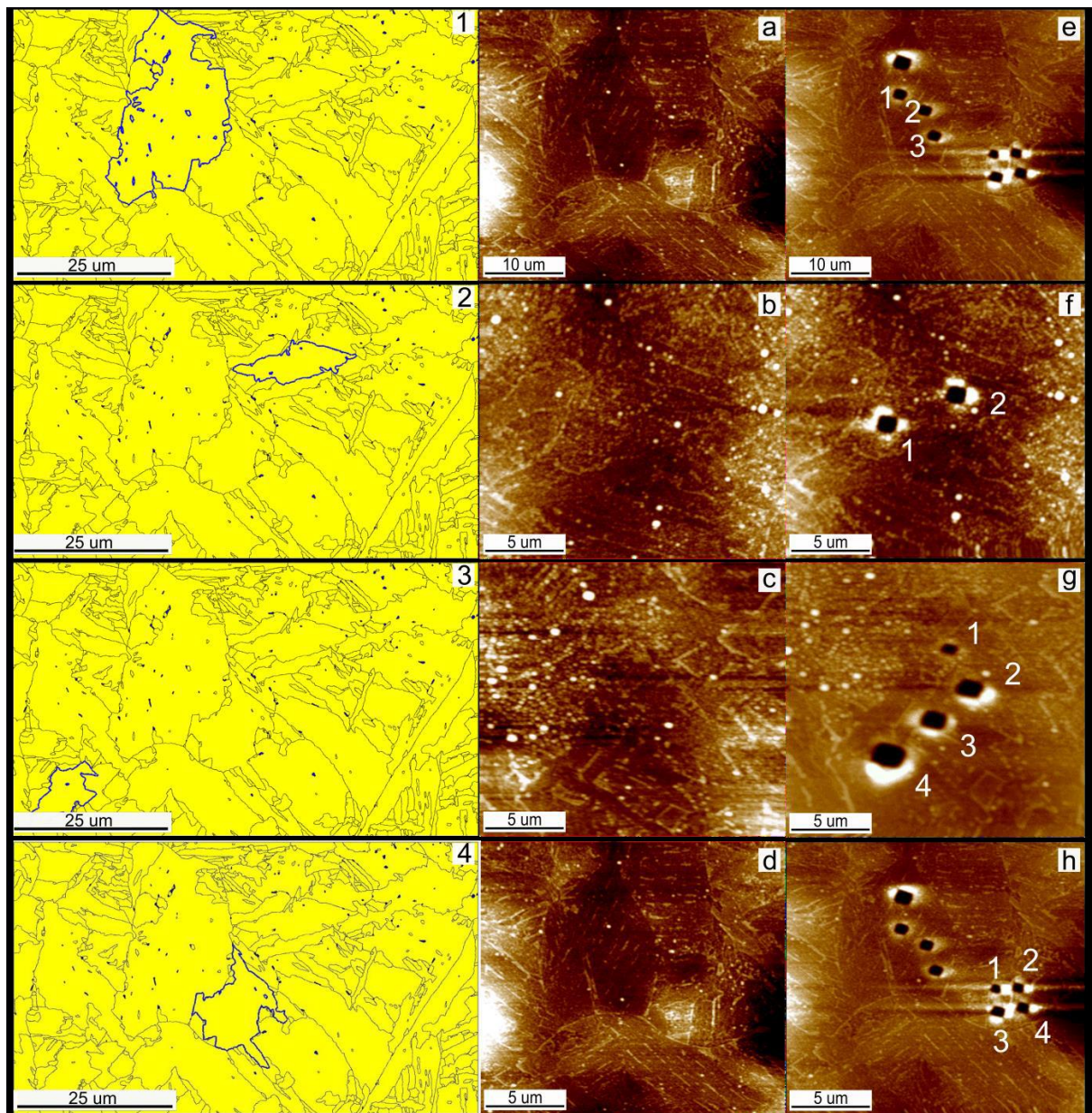


Figure 35: The conducted nanoindentation tests on the enumerated grains. (59)

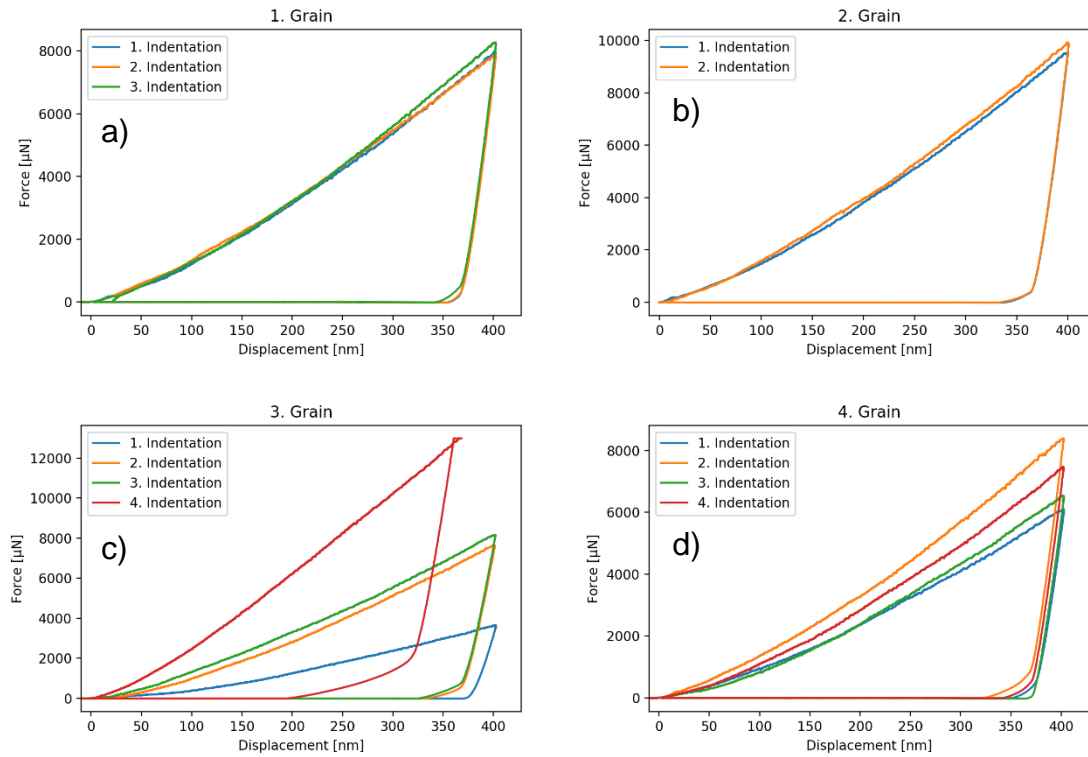


Figure 36: Nanoindentation test results of the PL steel. (59)

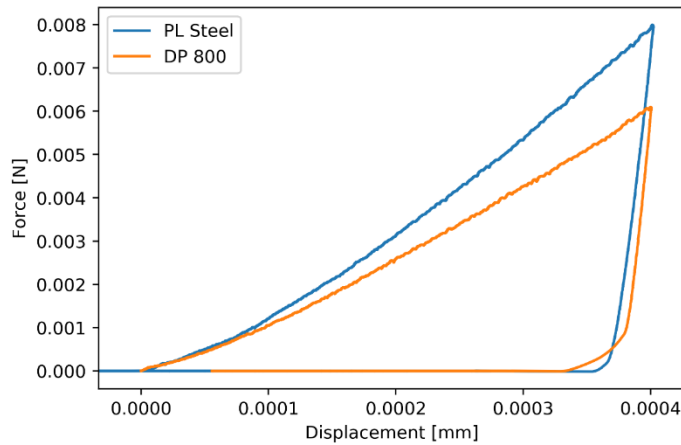


Figure 37: Force-displacement curves of the reference grains.

5.2 Simulation Results

For both AI and RS models more than 1500 simulations have been successfully conducted by means of the automation script. As an example, a snapshot from a simulation is demonstrated in **Figure 38**. At the top, a conical-shaped nanoindenter is

situated and at the bottom, the grain can be seen. One batch of simulation which is consists of 500 simulations has been submitted to train the AI model for DP steel and another batch of simulation with the same parameter set but different orientation data have been submitted for the AI model of the PL steel. From these 1000 simulations, a total number of 110,091 data points were collected. However as it was mentioned before, the distribution of the input data set is vital for a successful AI model. For that reason, the distribution plot of the force data for PL and DP steels are illustrated in **Figure 39**. It shows that the data is not equally distributed and there are significantly more data close to 0 N and with the increasing force the amount of the data points decreases steadily. This trend is valid for both PL and DP steel variants.

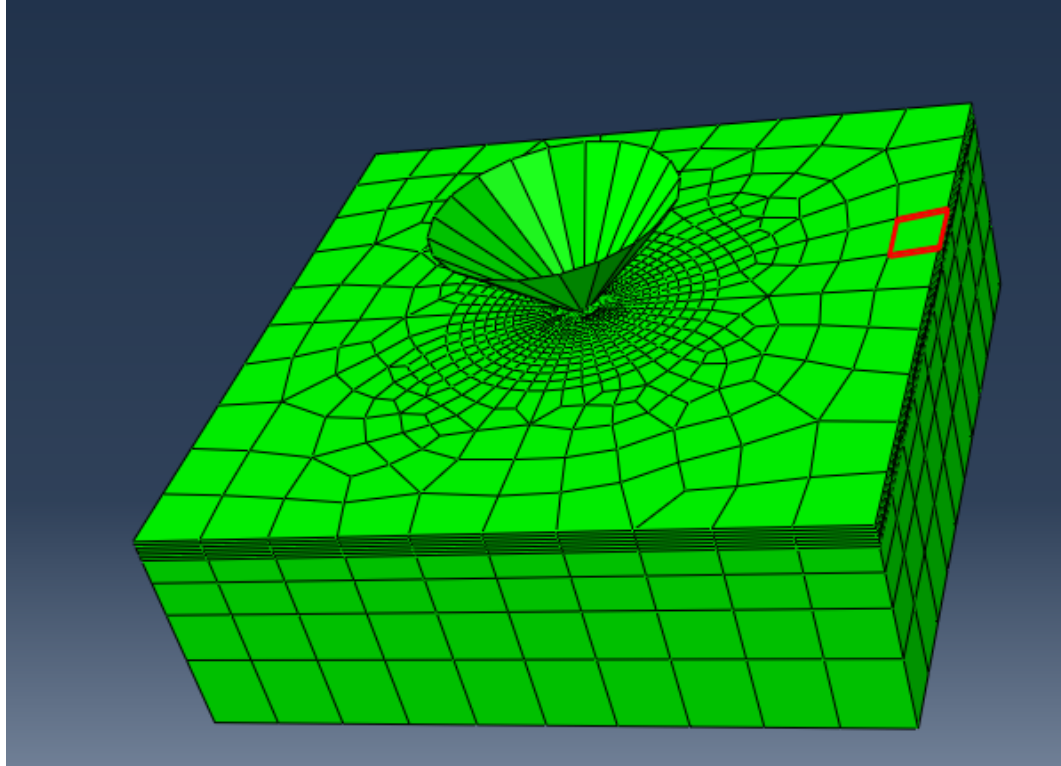


Figure 38: Visual demonstration of the simulation model.

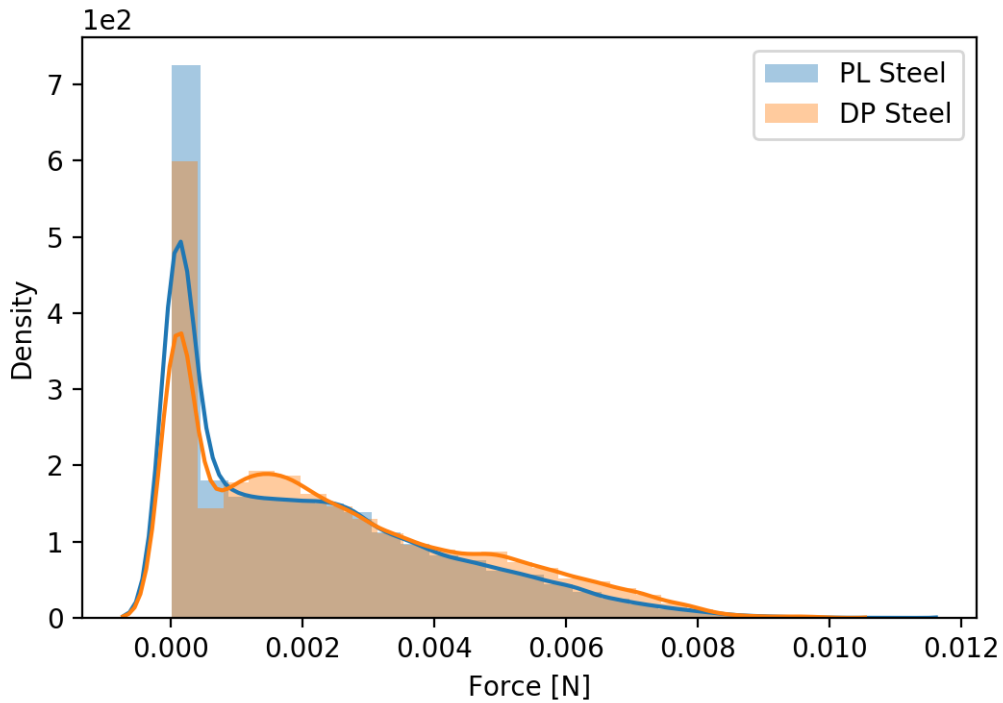


Figure 39: The distribution plot of the Force data for PL and DP steels with kernel density function.

5.3 Artificial Intelligence Model

Two AI models have been created for DP and PL steels and their prediction capabilities were evaluated. Based on the output data from CPFEM simulations AI models were trained.

5.3.1 Dual-Phase Steel Artificial Intelligence Model

Firstly, the AI model was developed in order to predict experimental force data. After training the model the r^2 score was evaluated and 0.9993 achieved. The model seems to be able to mimic Abaqus CPFEM analysis. The evaluation of the model can be seen in **Figure 40**. It was already mentioned that the available data were divided into a test set and a train set. Figure 40 shows that AI can predict test data accurately.

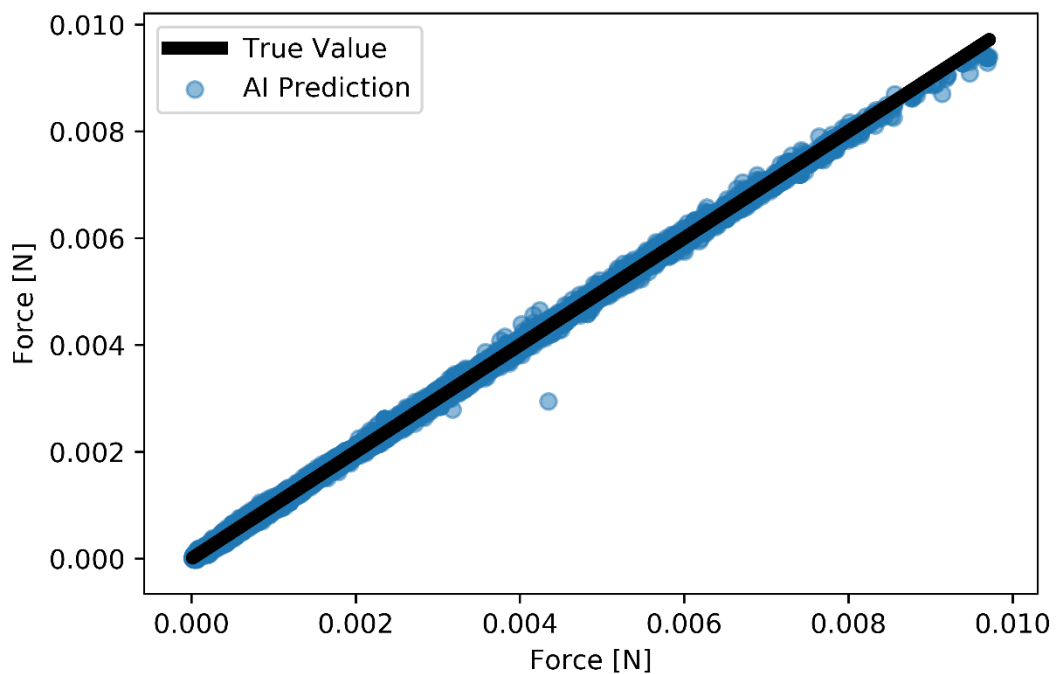


Figure 40: Test data and AI predictions for DP steel variant.

After creating the AI model the next step was submitting AICS. For that reason, 10.000 simulation input data sets have been created via LHS and submitted to the AI model. After getting the results, RMSE between experimental data and AI prediction was calculated. The best 25 predictions out of 10.000 AICS with the least RMSE are shown in **Table 11**. Then these parameter sets were indexed from 1 to 25 and simulated in the Abaqus CPFEM model.

Table 11: Ranking of top 25 AICS predictions sorted by RMSE.

AICS No.	Simulation No.	τ_0 , Mpa	τ_s , MPa	α	h_0 , MPa	RMSE
3760	1	81.57	822.14	1.31	504.8	4.94e-05
3880	2	101.06	748.5	1.21	406.1	8.36e-05
2530	3	74.48	828.97	1.89	660.69	8.88e-05
3604	4	58.76	782.72	1.05	598.21	9.17e-05
2845	5	89.85	819.69	1.47	523.67	0.0001
3550	6	76.1	787.34	1.44	557.2	0.0001
8761	7	124.4	777.04	1.51	272.09	0.000111
1100	8	57.81	696.89	1.33	794.36	0.000114
6305	9	44.24	815.67	1.48	871.34	0.000117
7735	10	79.2	692.46	1.28	647.88	0.000118
1583	11	94.82	742.35	1.61	560.11	0.000122
1039	12	63.13	811.31	3.64	1272.85	0.000129
4690	13	52.78	749.94	3.67	1509.45	0.00013
0096	14	60.52	695.84	1.1	777.94	0.000134
6016	15	76.45	758.35	3.92	1315.06	0.000137
3776	16	54.52	822.87	2.81	1032.67	0.000138
7805	17	65.16	767.67	2.61	1025.8	0.000138
8778	18	102.89	690.89	1.4	501.63	0.00014
2181	19	61.75	716.6	3.59	1446.15	0.00014
9483	20	50.75	691.52	1.01	716.69	0.00014
9200	21	69.75	780.07	4.25	1507.37	0.00014
9580	22	74.75	816.49	4.51	1496.77	0.000141
8600	23	51.19	608.33	2.03	1215.49	0.000141
4778	24	61.05	730.4	2.74	1145.07	0.000141
7480	25	47.4	727.48	1.65	986.31	0.000142

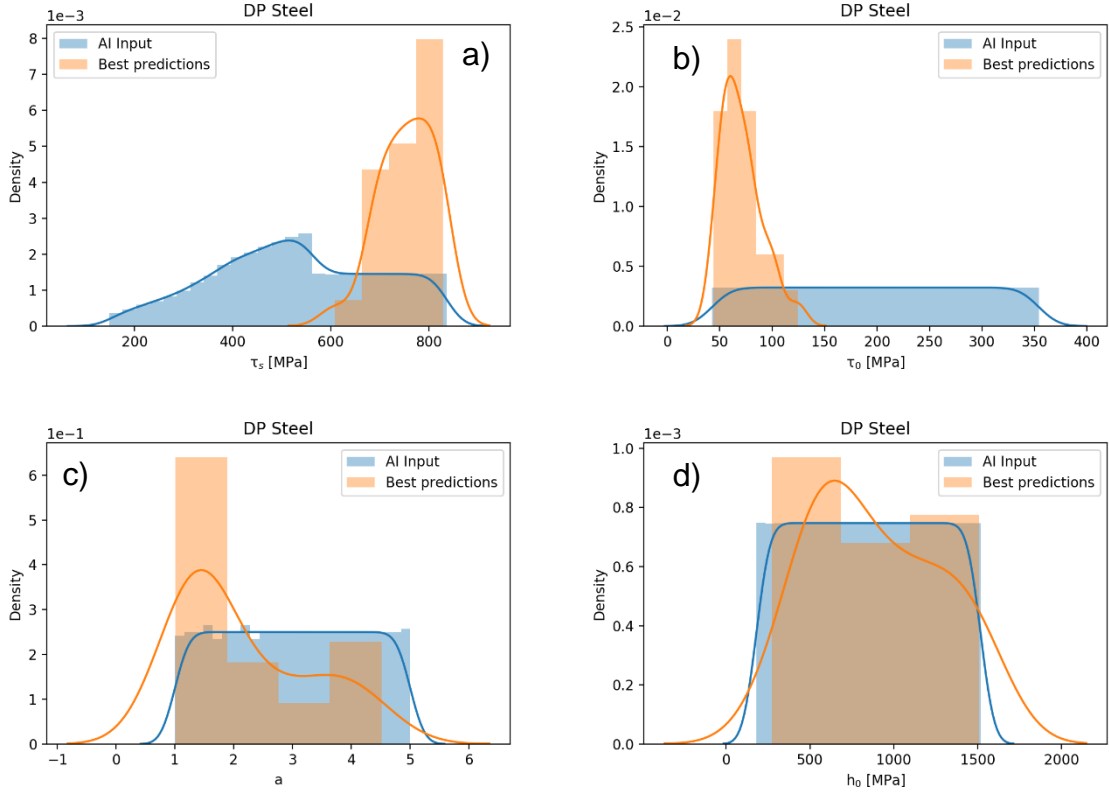


Figure 41: Distribution plots of the simulation input parameters which are mentioned in Table 11 with kernel density estimation function.

To have a better understanding of the results which are mentioned in Table 11 the CP parameter columns are visualized in **Figure 41**. The blue color represents the parameter range which is used for training the AI model. From Figure 41a, it can be said that the model finds high τ_s values which are close to 800 more accurate for the current CP model. Furthermore, the AI input dataset is not equally distributed because τ_s value cannot be smaller than τ_0 that is why when $\tau_0 > \tau_s$ the script adds 207 MPa to the current τ_s value. For that reason, there are more input data in between 400 and 600 than any other range. But despite this unbalanced distribution, the best AICS results show that a parameter range between 600 and 800 MPa is optimal for τ_s . On the contrary, Figure 41b shows that for τ_0 , a parameter range between 50 and 100 MPa is more suitable and there is not even one data above 150. For the α parameter (see Figure 41c) it is seen that the values between 1 and 2 more successful compared to other parameter ranges. Lastly from Figure 41d, it can be said that for h_0 , the parameter range around 500 MPa is more precise, however, there are no significant differences between parameter ranges.

Table 12: Abaqus simulation results of the top 25 AICS sorted by RMSE.

Simulation No.	τ_0 , MPa	τ_s , MPa	a	h_0 , MPa	RMSE
25	47.4	727.48	1.65	986.31	5.55E-05
9	44.24	815.67	1.48	871.34	6.29E-05
14	60.52	695.84	1.1	777.94	6.38E-05
8	57.81	696.89	1.33	794.36	6.66E-05
5	89.85	819.69	1.47	523.67	7.31E-05
10	79.2	692.46	1.28	647.88	7.67E-05
17	65.16	767.67	2.61	1025.8	8.19E-05
24	61.05	730.4	2.74	1145.07	8.27E-05
11	94.82	742.35	1.61	560.11	8.49E-05
21	69.75	780.07	4.25	1507.37	9.00E-05
23	51.19	608.33	2.03	1215.49	9.07E-05
2	101.06	748.5	1.21	406.1	9.23E-05
3	74.48	828.97	1.89	660.69	9.24E-05
12	63.13	811.31	3.64	1272.85	9.56E-05
1	81.57	822.14	1.31	504.8	9.88E-05
15	76.45	758.35	3.92	1315.06	0.000103
18	102.89	690.89	1.4	501.63	0.000104
22	74.75	816.49	4.51	1496.77	0.000105
13	52.78	749.94	3.67	1509.45	0.000109
6	76.1	787.34	1.44	557.2	0.000111
16	54.52	822.87	2.81	1032.67	0.000114
19	61.75	716.6	3.59	1446.15	0.000115
4	58.76	782.72	1.05	598.21	0.000138
20	50.75	691.52	1.01	716.69	0.000169
7	124.4	777.04	1.51	272.09	0.00021

After determining the best AICS predictions, real simulations took place, and all the 25 parameter sets were submitted to the Abaqus CPFEM model. The results are mentioned in **Table 12** based on their RMSE and at first sight, it can be said that there is a deviation in terms of RMSE between AICS and Abaqus simulations. For example,

Simulation 25 has the highest RMSE based on AICS (see Table 11), however, in the real simulation it shows the lowest RMSE (see Table 12). So in order to see the difference between experimental data, AICS and Abaqus results; 6 simulations with the least RMSE from Table 12 are illustrated in **Figure 42**.

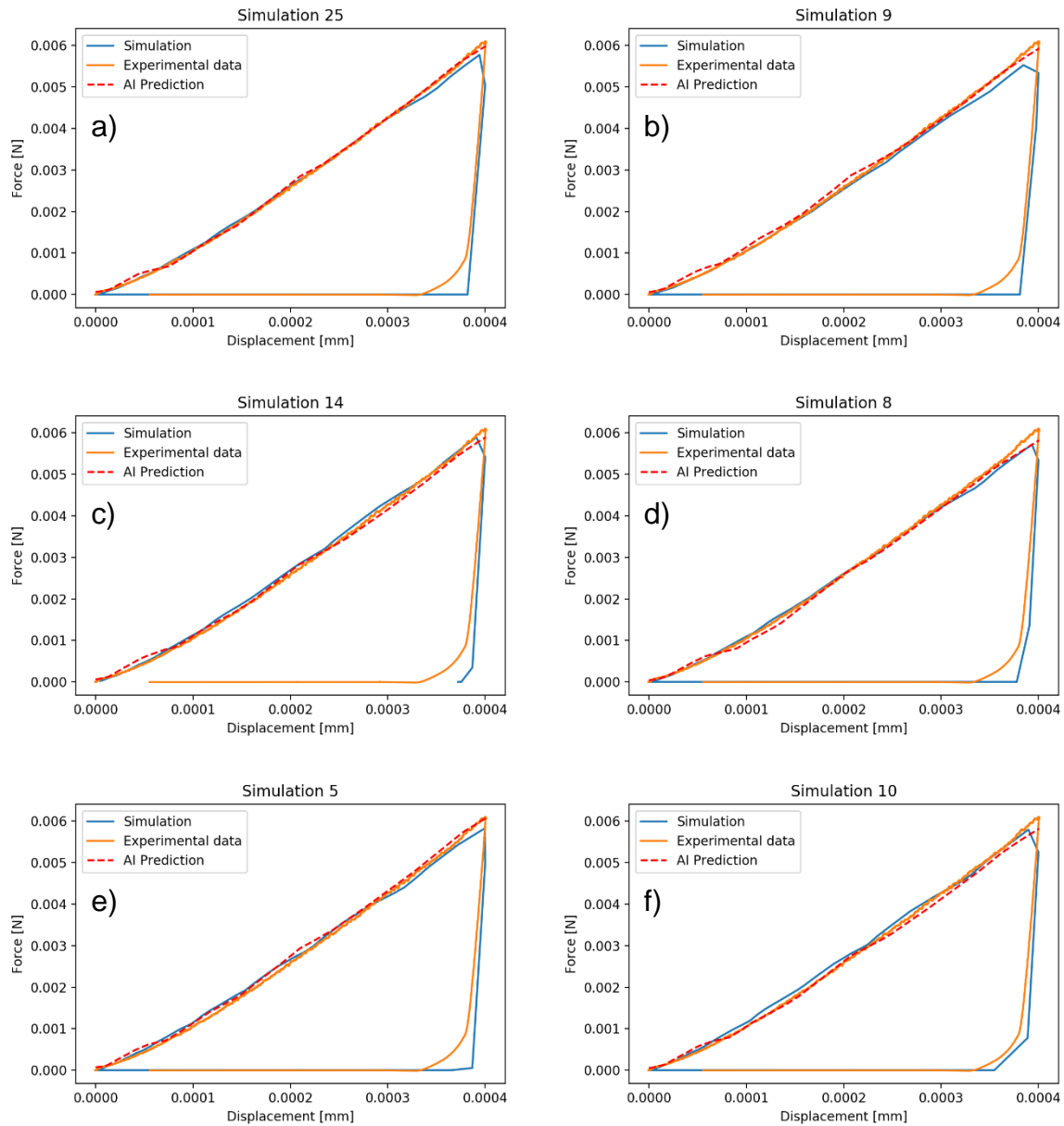


Figure 42: Demonstration of the Abaqus simulation results with AICS and experimental data.

From Figure 42, it can be seen that there is a good agreement between the AICS, Abaqus, and experimental results for all the mentioned graphs. All three curves increase linearly with increasing Displacement. However, it should be noted that when

the curve comes closer to the highest Force area which is in this case around 0.006 N some deviations become visible especially for Simulation 9 (see Figure 42b). But below that area, all the three curves are more or less identical for all the six simulations. The reason for this deviation will be discussed in the Discussion section.

5.3.2 Pipeline Steel Artificial Intelligence Model

The same AI model which is evaluated for DP steel was used in the current case. The model was trained with the same parameters set but this time orientation data is also included. For that reason, another 500 simulations were conducted. Then, the training of the model took place. To ensure that the previous model is compatible with the PL CPFEM output data, 40 AI models were created and their average r^2 score was found 0.998375689. This score proves that the previous model is also able to mimic Abaqus CPFEM analysis for PL steel. Between these 40 models the model with the highest r^2 score (0.9991) was chosen. And it is seen in **Figure 43** that AI can predict test data accurately.

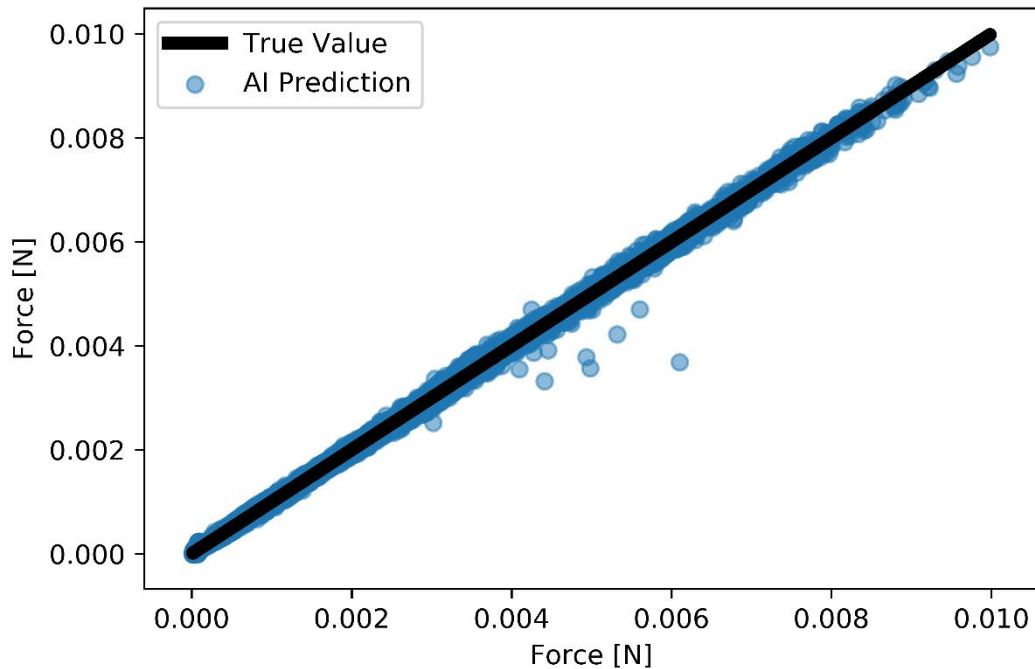


Figure 43: Test data and current AI predictions for the PL steel variant.

After creating the AI model the next step was submitting AICS. For that reason, the same 10,000 simulation input data set have been used and submitted to the current AI model. After getting the results, RMSE between experimental data and AI prediction was calculated. The best 25 predictions out of 10,000 AICS with the least RMSE are shown in **Table 13**. Then these parameter sets were indexed from 1 to 25 and simulated in the Abaqus CPFEM model.

Table 13: PL steel top 25 AICS predictions sorted by RMSE.

AICS No.	Simulation No.	τ_0 , MPa	τ_s , MPa	α	h_0 , MPa	RMSE
2845	1	56.82	834.66	1.54	1371.99	0.000211977
8085	2	80.01	804.06	1.35	1115.34	0.000216533
6091	3	62.96	792.31	1.54	1396.75	0.000224636
8599	4	73.37	794.81	1.98	1469.27	0.000225792
8580	5	67.12	824.66	1.27	1260.3	0.000231281
5285	6	126.47	812.51	1.58	818.74	0.000241839
5046	7	87.6	816.94	2.31	1485.18	0.000246807
5587	8	59.76	786.89	1.18	1369.34	0.000252357
7126	9	100.76	721.19	1.06	940.23	0.000256529
6694	10	109.01	759.19	1.74	1138.53	0.000257565
5292	11	89.49	759.63	1.51	1271.34	0.000257644
3735	12	111.35	777.42	1.9	1022.51	0.000260291
7743	13	105.66	775.52	2.67	1466.43	0.000260714
2332	14	87.34	835.61	1.93	1103.04	0.000266764
5880	15	84.2	718.67	1.37	1371.26	0.000267977
4115	16	139.8	773.11	1.55	721.33	0.000270358
1426	17	63.57	764.53	1.65	1334.45	0.000271394
6616	18	112.67	714.14	1.32	926	0.000271717
5120	19	46.85	798.73	1.52	1357.18	0.000272496
0943	20	120.26	689.7	1.44	1012.68	0.000273048
2384	21	116.95	776.98	2.95	1509.64	0.000273491
5877	22	146.01	801.73	1.82	805.8	0.000274916
5860	23	119.32	767.63	2.67	1295.36	0.000275236
8918	24	118.3	687.37	1.2	908.35	0.000275291

5171	25	127.36	757.28	1.75	989.5	0.000275335
------	----	--------	--------	------	-------	-------------

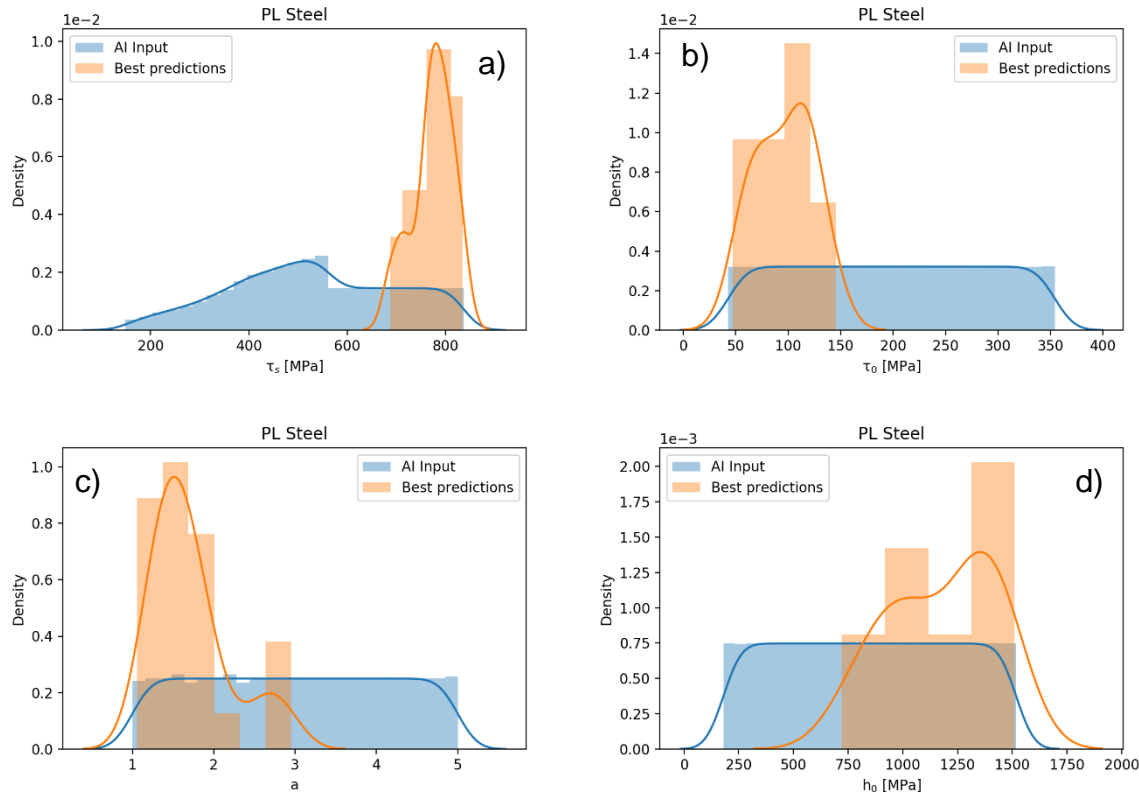


Figure 44: Distribution plots of the simulation input parameters which are mentioned in Table 13 with kernel density estimation function.

To illustrate the results which are mentioned in Table 13 the CP parameter columns are visualized in **Figure 44**. From Figure 44a, it can be said that high τ_s values which are close to 800 MPa more precise for the current CP calibration. On the contrary, Figure 44b illustrates that the τ_0 values between 50 and 150 MPa more suitable and there is not even one demonstrated data above 150 MPa. For the a parameter, as shown in Figure 44c, it is seen that the values between 1 and 2 more precise compared to other parameter ranges. Lastly from Figure 44d, the h_0 parameter was found in a range between 1000 and 1500 MPa. After determining the best AICS predictions and their data set, real simulations took place, and 25 simulations were submitted to the Abaqus CPFEM model. The results are mentioned in **Table 14** and sorted by their RMSE. At first sight, it can be said that there is a good agreement in terms of RMSE between AICS and Abaqus simulations. Simulation 1,2,3,4,5 has the lowest RMSE based on AICS prediction (see Table 13), and these predictions is supported by the real Abaqus simulations (see Table 14). So to make a comparison

between experimental data, AICS, and Abaqus results; 6 simulations with the least RMSE from are illustrated in **Figure 45**.

Table 14: Abaqus simulation results of the top 25 AICS sorted by RMSE.

Simulation No.	τ_0 , MPa	τ_s , Mpa	a	h_0 , MPa	RMSE
5	67.12	824.66	1.27	1260.3	0.000121
2	80.01	804.06	1.35	1115.34	0.000138
3	62.96	792.31	1.54	1396.75	0.000145
4	73.37	794.81	1.98	1469.27	0.000155
1	56.82	834.66	1.54	1371.99	0.000156
12	111.35	777.42	1.9	1022.51	0.000165
8	59.76	786.89	1.18	1369.34	0.000166
7	87.6	816.94	2.31	1485.18	0.000173
17	63.57	764.53	1.65	1334.45	0.000175
9	100.76	721.19	1.06	940.23	0.000181
14	87.34	835.61	1.93	1103.04	0.000185
13	105.66	775.52	2.67	1466.43	0.00019
10	109.01	759.19	1.74	1138.53	0.000195
18	112.67	714.14	1.32	926	0.000196
23	119.32	767.63	2.67	1295.36	0.000198
20	120.26	689.7	1.44	1012.68	0.000202
6	126.47	812.51	1.58	818.74	0.000204
24	118.3	687.37	1.2	908.35	0.000208
16	139.8	773.11	1.55	721.33	0.000218
21	116.95	776.98	2.95	1509.64	0.000222
25	127.36	757.28	1.75	989.5	0.000231
11	89.49	759.63	1.51	1271.34	0.000232
22	146.01	801.73	1.82	805.8	0.000242
15	84.2	718.67	1.37	1371.26	0.000262
19	46.85	798.73	1.52	1357.18	0.000346

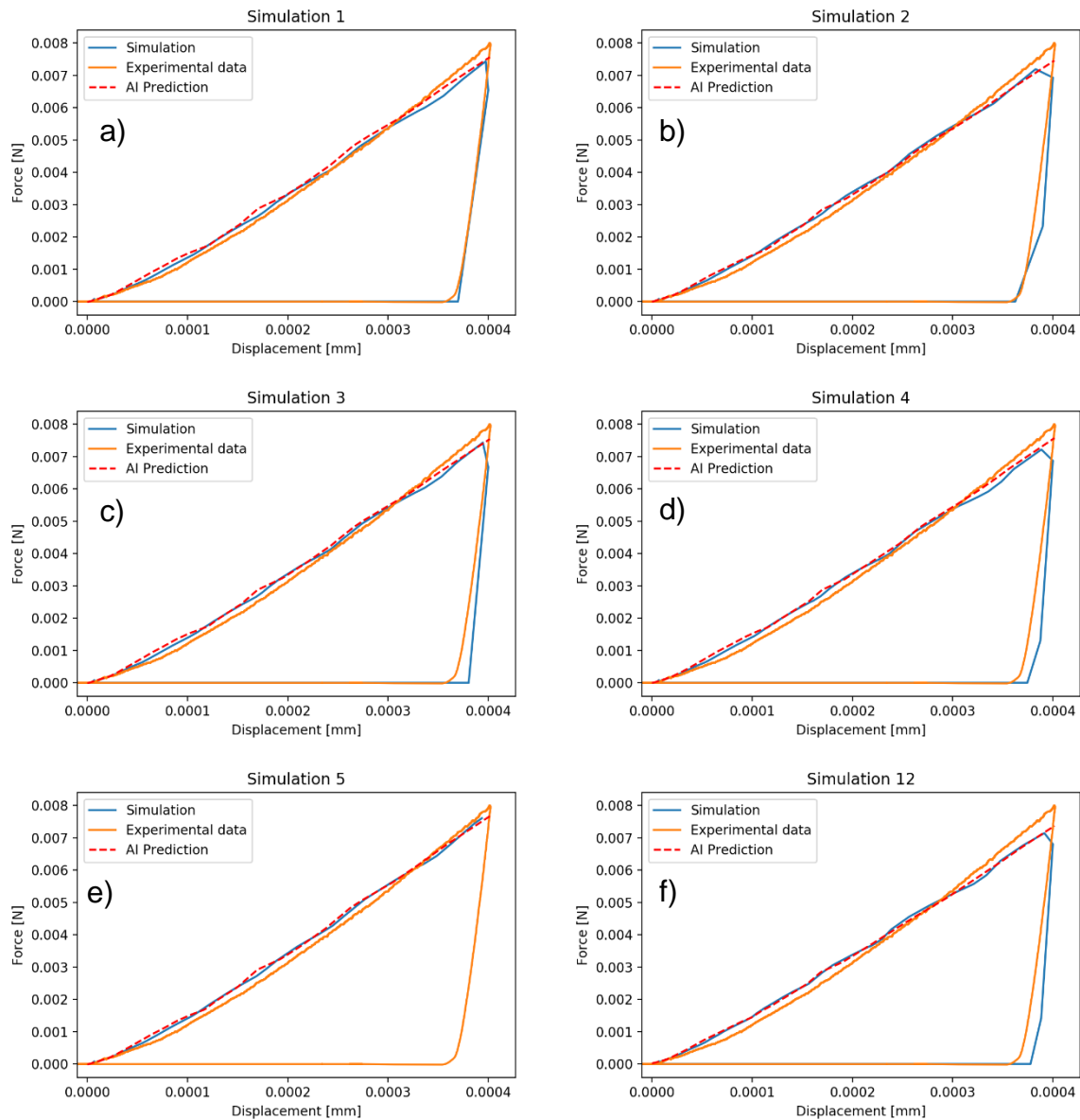


Figure 45: Demonstration of the Abaqus simulation results with AICS and experimental data gathered from the PL steel.

From the graphs in Figure 45, it can be said that there is good agreement between the AICS and CPFEM results. In Figure 45e the fitting between the AICS and the simulation curve is better compared to the other simulations. However, the experimental curve looks slightly different compared to the other two curves. This deviation becomes clear at the highest force value which is 0.008 N. Especially Simulation 12 (see Figure 45f) goes until 0.007 N which is far from the experimental data. On the other hand, Simulation 5 (see Figure 45e) shows a good fitting property,

however, due to the convergency error arising from the software the unloading part cannot be mentioned.

5.4 Response Surface Model

As it was mentioned before, the RS model is composed of 3 stages which are sensitivity analysis, exploration, and exploitation. In this chapter first of all sensitivity analysis will be introduced and then the two stages will be mentioned for DP and PL steels separately.

5.4.1 Morris Sensitivity Analysis

MSA was conducted with 100 simulations and the range of the input parameter set is mentioned in **Table 15**. Concerning some convergency errors, the minimum τ_s value was set to 561 so that it gets always higher values than τ_0 .

Table 15: Input parameter range of the MSA.

Parameter	Min.	Max.
τ_0 , MPa	43	354
τ_s , MPa	561	837
a	1	5
h_0 , MPa	180	1518

After conducting, simulations results are gathered and mentioned in **Figure 46**. As it was said before the higher distance from the origin represents higher sensitivity for that reason all the numerical data gathered in **Table 16** and euclidian distance calculated. The μ value represents the direct effect of the parameter on the output. If it is positive there is a positive correlation between parameter and output. On the other hand, if it is negative there is a negative correlation. Based on these results it can be said that only a parameter is inversely correlated with the slope and the rest is directly proportional. From Table 16 and Figure 46, it can be concluded that τ_0 and h_0 parameters have higher effect on the output. The output in this equation is the slope of the provided force-displacement curve during loading phase. Based on these results the optimization task will be conducted by changing τ_0 and h_0 parameters, and the rest will stay constant.

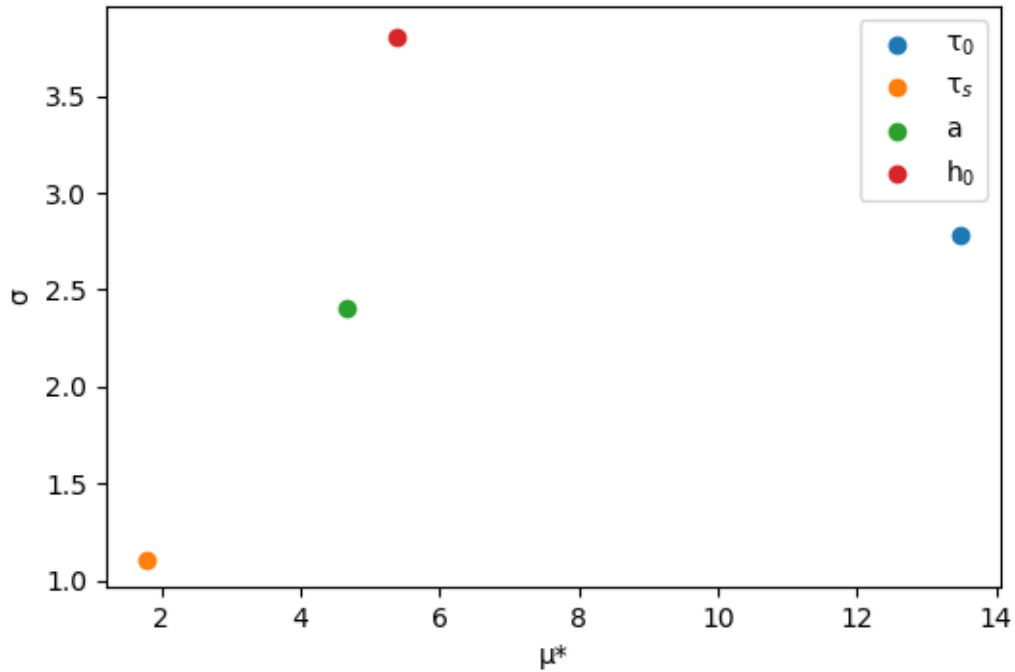


Figure 46: Demonstration of the MSA results.

Table 16: Numerical demonstration of the MSA.

Parameter	μ	μ^*	σ	Distance
τ_0 , MPa	13.470015	13.470015	2.781607	13.754223
τ_s , MPa	1.793891	1.793891	1.102315	2.105503
a	-4.670695	4.670695	2.400427	5.251422
h_0 , MPa	5.393419	5.393419	3.801918	6.598754

5.4.2 Response Surface Model for Dual-Phase Steel

After conducting MSA, the next step was finding the initial parameter set. For this, a previously optimized model was taken as the initial parameter set and mentioned in **Table 17**. The simulation data versus experimental data is illustrated in **Figure 47**. So for the DP steel a and τ_s are 4.57 and 1000.86 respectively. As to, τ_0 , h_0 parameters, they will be optimized within exploration and exploitation stages.

Table 17: The initial parameter set for the DP steel.

τ_0 , MPa	τ_s , Mpa	α	h_0 , MPa
50	1000.86	4.57	1500

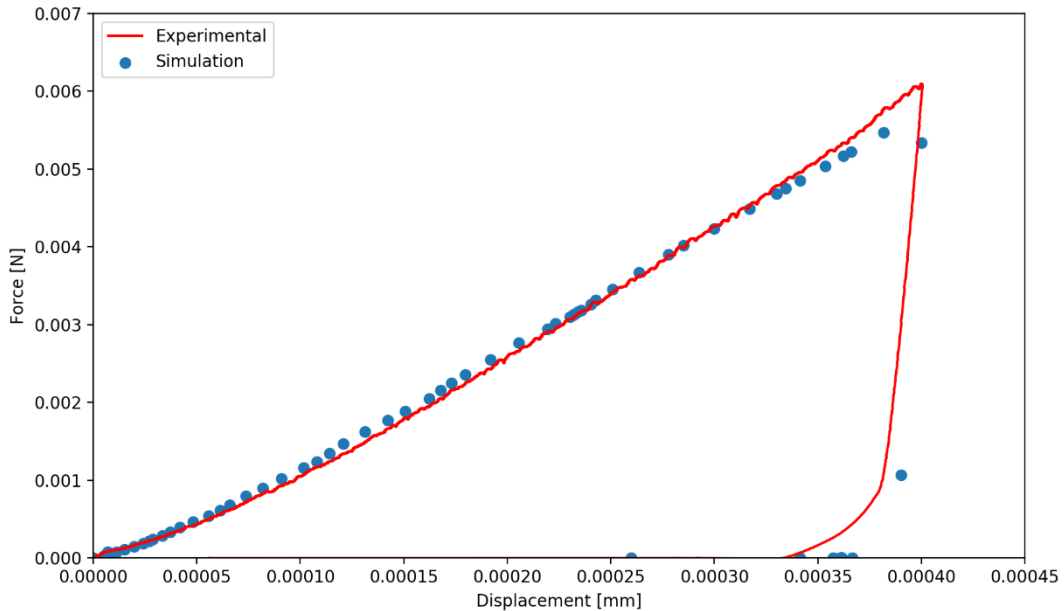


Figure 47: Experimental curve and initial simulation results.

The exploration stage took place with 100 simulations. Then each simulation's RMSE was calculated and a 3D graph which can be seen in **Figure 48** was generated. In the graph, the red color represents high RMSE and the blue color represents low RMSE. It is seen that with increasing τ_0 , RMSE increases for all the h_0 values. On the other hand, with increasing h_0 , RMSE decreases continuously for low τ_0 variants and increases for τ_0 high variants. From the graph, it is clear that the area where low τ_0 and high h_0 situated is the place where the exploitation stage should take place. But this should be also supported by the PSO algorithm. The current data integrated into the algorithm and the global minima found 1499 and 51 for h_0 and τ_0 . The exploration stage is finished here and the last stage which is called exploitation takes place.

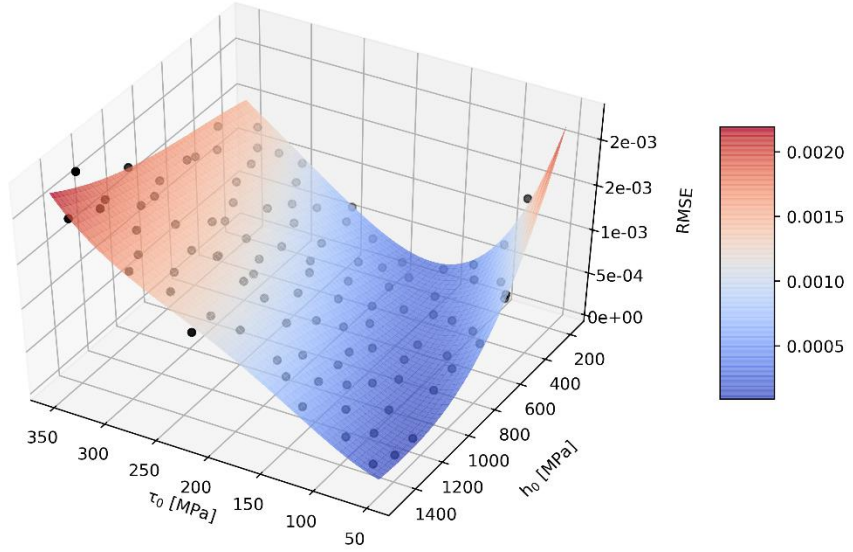


Figure 48: Exploration stage of the current DP steel.

For the exploitation phase once again LHS was used to create input data sets based on previous PSO results. As a range, for h_0 it is known that with the decrement of this value RMSE increases (see Figure 48) for that reason the new range is set between 1400 and 1600. For the τ_0 parameter, a parameter set between 30 and 70 was preferred. Based on these parameter ranges 30 simulations have been created and submitted. When all the simulations were completed RMSE of all the simulations has been calculated and the results are illustrated in **Figure 49**.

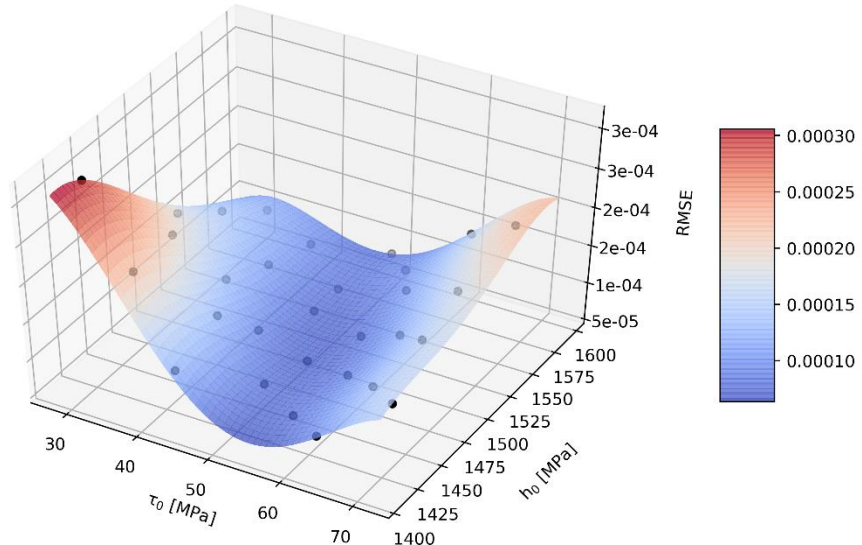


Figure 49: First exploitation phase based on given PSO results.

From the graph, it can be said that the highest and lowest τ_0 values cause high RMSE and with increasing h_0 , RMSE increases as well. At first sight, the optimum range seems to be between 50 – 60 MPa for τ_0 and for the h_0 it is around 1400 MPa. To find the exact global minimum PSO once again used and results are 1404 MPa for h_0 and 54 MPa for τ_0 .

Based on these results the exploitation range became denser and for the last time LHS is used for creating 30 simulations within the range of 40-70 MPa for τ_0 and 1300-1400 for h_0 .

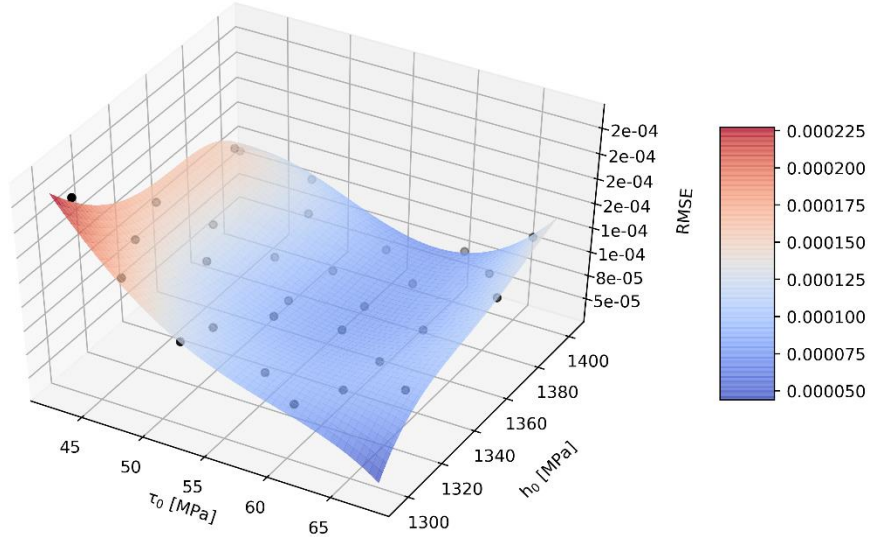


Figure 50: Second exploitation phase based on the PSO results.

When all the simulations were completed their RMSE has been calculated and the results are mentioned in **Figure 50**. It can be seen that the surface is almost totally blue and the provided RMSE is low. Only the lowest τ_0 value contains the highest RMSE and beginning from 50 MPa the surface presents low RMSE. Based on these results it can be said that no more exploration or exploitation phase is required. For the final stage, 6 simulations that exhibit the least RMSE have been compared with the experimental data, and results are mentioned in **Figure 51**. All the simulations show good agreement with the experimental data, especially Figure 51a,c exhibit better curve fitting properties compared to the other simulations. Apart from this, in Figure 51b,d,e,f the curves are identical at the beginning but in the end, a slightly higher deviation around maximum force (0.006 N) becomes visible. Especially in

Figure 51d, the deviation between 0.0003 and 0.0004 mm is significant. The reason for this deviation will be discussed in Discussion section.

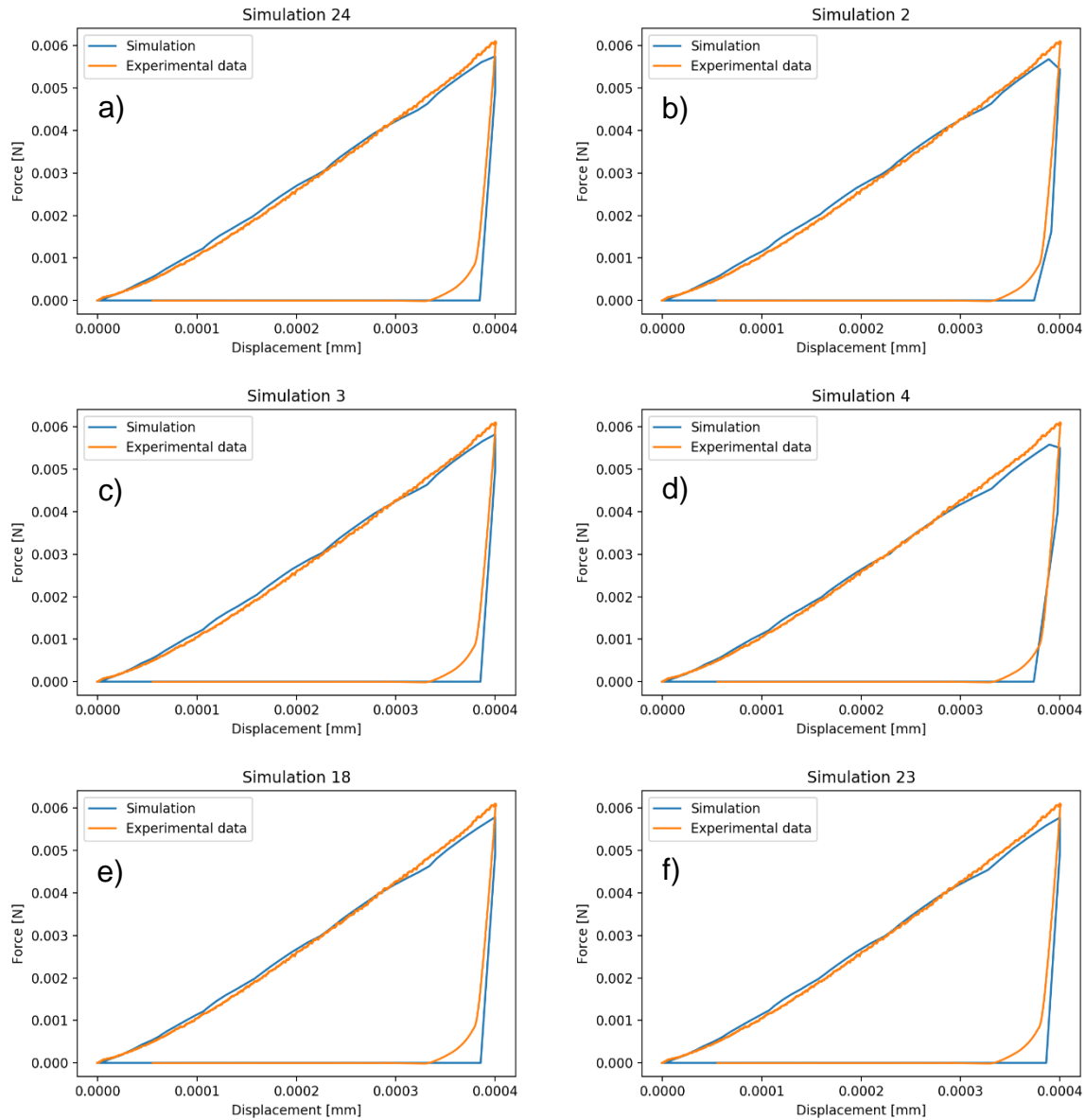


Figure 51: Best 6 RS model predictions for DP steel.

5.4.3 Response Surface Model for Pipeline Steel

After finishing the RS model for the DP steel, the next step was implementing this model to the PL steel. Just like the previous case first of all the initial parameter set should be determined via pre-submitted simulations. RMSE was calculated between experimental data and 500 Simulations which were used for training the AI model for

PL steel, and once again the parameter set of the simulation which gives the least RMSE was taken as the initial parameter set.

After calculating RMSE the initial parameter set was determined and mentioned in **Table 18** and the simulation data versus experimental data is illustrated in **Figure 52**. For the PL steel α and τ_s are 1.57 and 822.17 respectively. The other two parameters, (τ_0, h_0) will be optimized within exploration and exploitation stages.

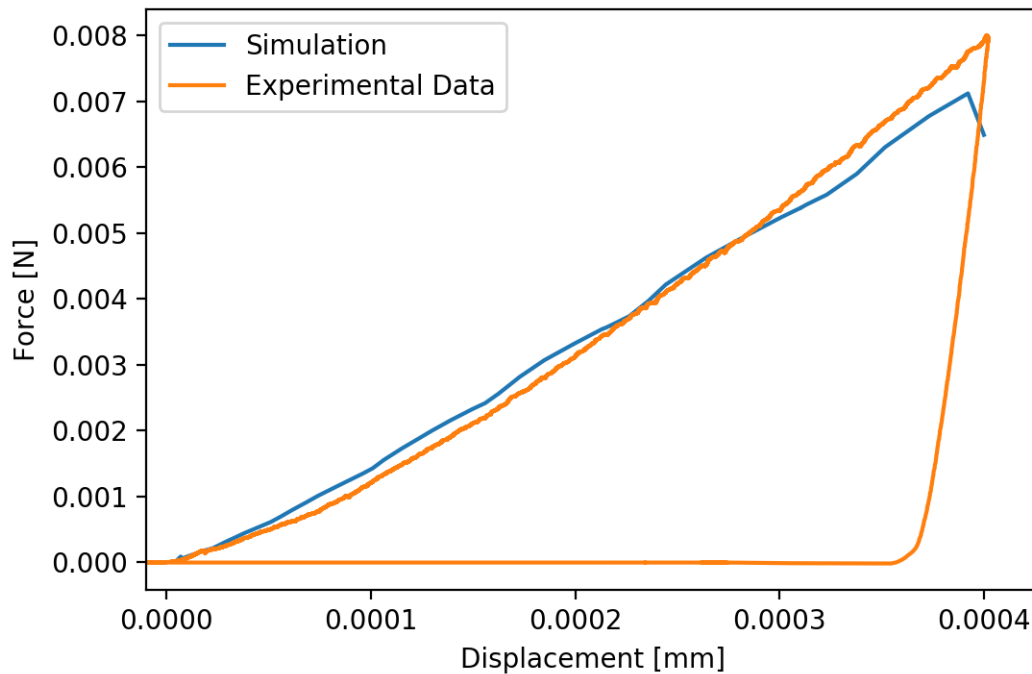


Figure 52: Demonstration of experimental and the result of the simulation with the initial parameter set.

Table 18: Initial parameter set for the PL steel.

τ_0 , MPa	τ_0 , Mpa	α	h_0 , MPa
104	822.17	1.57	881.96

The exploration stage took place with the same amount of simulations and within the same parameter range which is used for DP steel. Then each simulation's RMSE was calculated and the results are mentioned in a 3D graph which can be seen in **Figure 53**. It can be seen that with increasing τ_0 , RMSE increases for all the h_0 values. On the other hand, with increasing h_0 , RMSE decreases continuously for low

τ_0 values and increases for high τ_0 values. The current data was submitted into the PSO algorithm and the global minima found 1500 and 50 for h_0 and τ_0 respectively. The exploration stage is finished here and the next stage, exploitation, took place.

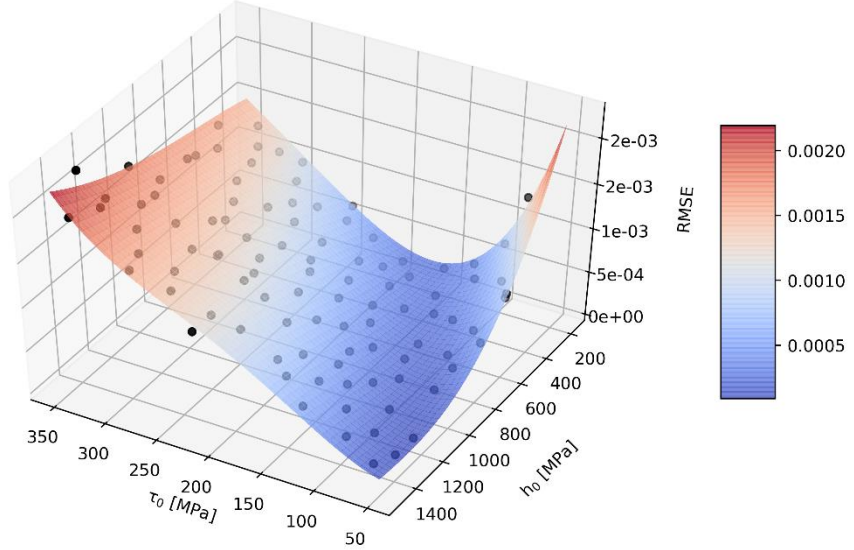


Figure 53: Exploration stage of the PL steel.

For the exploitation stage, the dataset from the first exploitation phase of the DP steel was used due to the same PSO results and a similar response surface. So the range of the τ_0 parameter is between 30 and 70 and for the h_0 it is between 1400 and 1600. Based on these parameter ranges 30 simulations have been submitted. When all the simulations were completed RMSE of all the simulations has been calculated and the results are presented in **Figure 54**. From the graph, it can be noticed that with for all the h_0 values, and beginning from 60 MPa decreasing τ_0 , cause increase of RMSE. But also through the highest point of τ_0 RMSE increases. To find the exact global minimum PSO once again used and results are 1444 MPa for h_0 and 58 MPa for τ_0 . So for the next exploitation phase the τ_0 parameter is ranged between 46 and 70 MPa and h_0 is set between 1388 and 1600 and a new parameter set was created with the LHS algorithm.

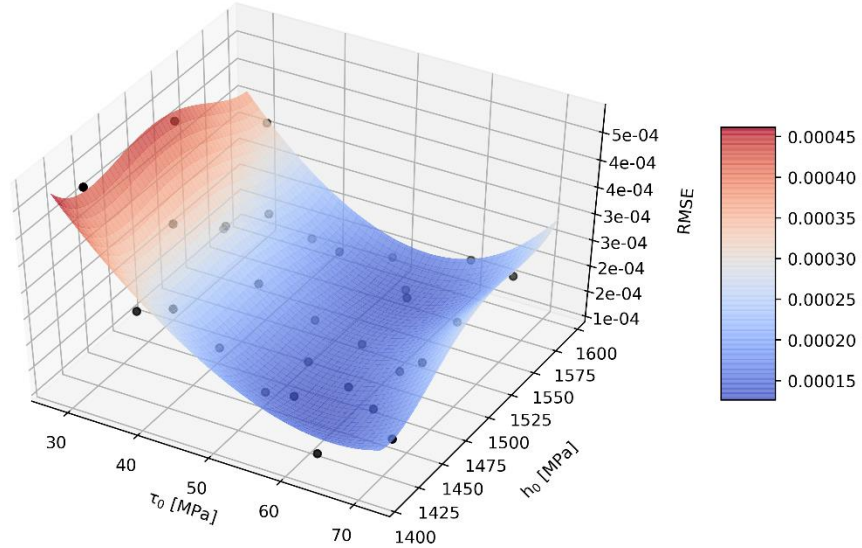


Figure 54: First exploitation phase of the PL steel.

After completing all the simulations, their RMSE has been calculated and the results are mentioned in **Figure 55**. It is seen that apart from the highest value of h_0 and the lowest value of τ_0 the surface is mostly blue and minimum error is achieved almost all over the surface. Based on these results it can be said that no more exploration or exploitation stage is required. For the final stage, 6 simulations that show the least RMSE have been compared with the experimental data, and results are mentioned in **Figure 56**. All the mentioned graphs show good agreement between experimental and simulation data until 0.003 mm and then, significant deviations between 0.003 – 0.004 mm. Especially at the maximum displacement point, the minimum deviation between experimental and simulation data is 0.000633 N (see Figure 56c) which is relatively high for this work. The reason for these undesired results will be discussed in the Discussion section.

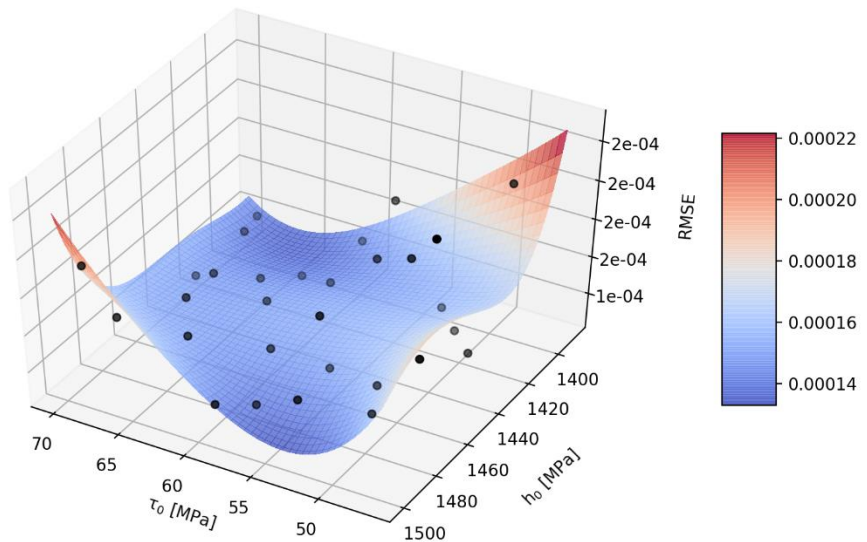
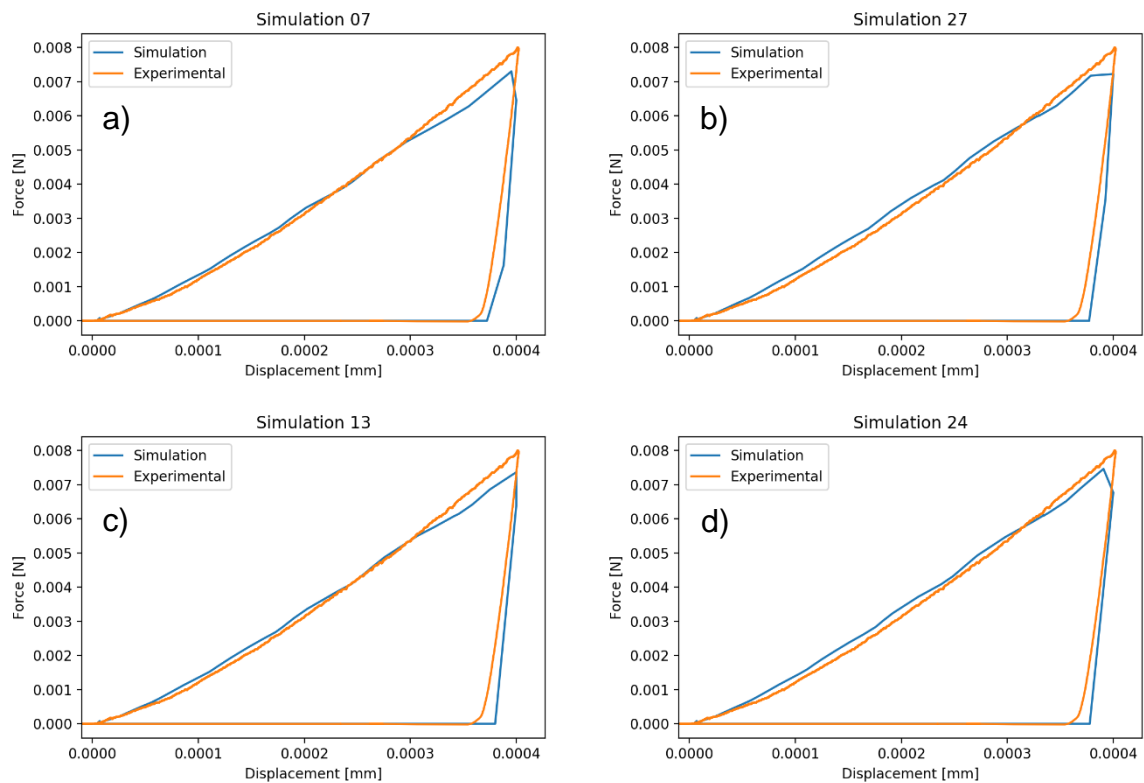


Figure 55: Second exploitation phase of the PL steel.



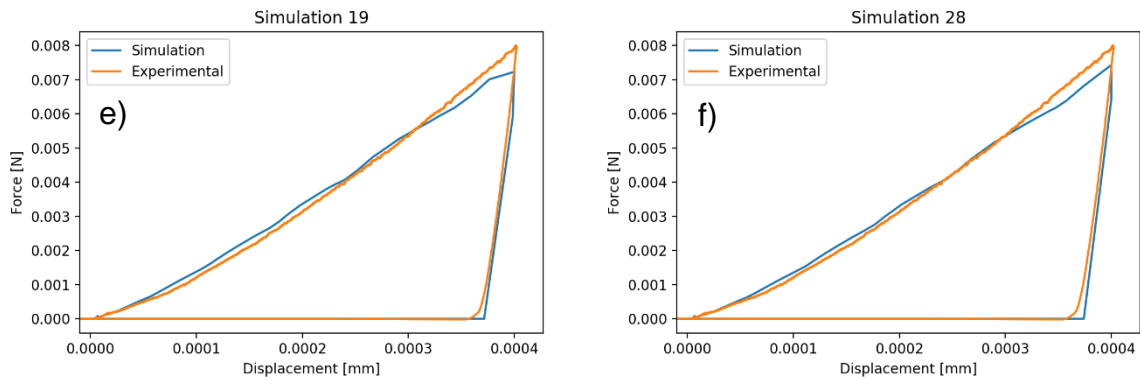


Figure 56: Best 6 RS model predictions for PL steel.

6 Discussion

In this chapter, both models will be discussed in terms of curve fitting capabilities. First of all, the experimental test results will be evaluated. Then, the AI models will be analyzed and the RS models will follow. Lastly, evaluated parameter sets will be compared in between.

6.1 Nanoindentation Test

It has been mentioned that in some nanoindentation tests, resulting curves show high deviations. To understand this phenomenon it should be taken into account that the grain size has a notable influence on the nanoindentation experiment. When the grain size gets smaller it is getting hard to identify it and, on the other hand, placing the indenter tip on the grain becomes more challenging. If a grain boundary is hit with the indenter instead of the grain matrix, the force-displacement diagram shows a different course. The reason is the difference in hardness between grain boundary and grain matrix. Another problem with the small grains arises due to the interaction between close indentations. After performing a nanoindentation test the material hardens locally. If the next indentation takes place close to that area, a different force-displacement curve can be recorded due to the local hardening. The reason for the significantly different curves that have been gathered from PL steel grains 3 and 4 (see Figure 36) can be due to their small size compared to grains 1 and 2.

As to the difference between the DP and PL force-displacement curves (see Figure 37), it can be said that their different production routines which are explained previously in the State of the Art, lead to different microstructure and hardening. From

Figure 34, and Figure 21 it can be seen that PL steel is more elongated compared to DP steel due to the higher deformation rate. This higher deformation leads to high hardening and naturally higher force values for the same displacement depth.

6.2 FEM Simulations

As it is mentioned before simulations are conducted to generate necessary data for the AI and RS models. For that reason, their input, output data, and also the fitting evaluation gain importance. Due to the convergency error, not all the simulations could be successfully terminated. For that reason, as it can be seen in **Figure 57a** there are two peaks at the beginning, and then, the density curve continues steady, however, for the PL steel, the density curve decreases sharply around 0.0004 mm. This might cause some prediction issues at 0.0004 mm for the PL steel. Force data represents a similar behavior (see Figure 57b). In the beginning, data density shows a peak and then it decreases continuously for both steel variants. The most significant outcome of this graph is that there are hardly enough data points at 0.008 N which is crucial for the PL steel variant because during the nanoindentation test force-displacement curve reaches 0.008 N and then the unloading stage takes place. This issue does not valid for the DP steel because the maximum force reaches 0.006 N and there are enough data points at that range. So, based on these distribution curves, it can be concluded that the AI model for the DP steel can be more accurate compared to the PL steel due to the distribution of the output data set.

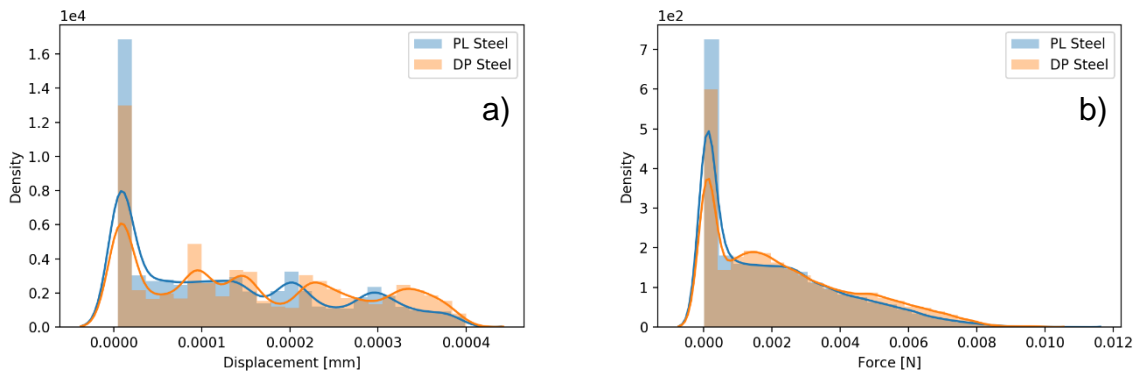


Figure 57: Distribution of the simulations output data for a) Displacement b) Force data.

Another issue that can be arisen due to the unbalanced data density is the effectiveness of the error function. To evaluate the curve fitting capability RMSE is used for both AI and RS models. In 2015, Li *et al.* (80) published a paper in which they identify elastic and plastic parameters using the nanoindentation test followed by simulation and differential evolution optimization to fit the simulation result to the experimental data. As the error function, they have combined RMSE, the difference between the area under the curves, and maximum loads. For each error function, they have assigned different weights and curve fitting is conducted based on decreasing this error function. For reasons of simplicity at the beginning of this study, RMSE was taken as the error function. However, during the postprocessing, this turned out to be an inaccurate method. Due to the short amount of time given for this thesis, this could not be replaced completely by the weighted error function. Therefore, this will be left for future works.

Figure 58 compares the results obtained from the second exploitation stage of PL steel. It is evident that Simulation 2 exhibits better fitting than Simulation 1, however as it can be seen in the figures, RMSE of Simulation 1 is less than Simulation 2. To investigate this issue their data distribution is visualized in **Figure 59**. It is seen that the data density of Simulation 1 is concentrated between 0 - 0.0001 and 0.0002 – 0.0003 mm. If in these two ranges, RMSE is low and outside of these ranges there is a significant deviation, the RMSE will be still low because few data points do not have much influence on the RMSE. Despite having higher RMSE the Simulation 2 fits better because most of the data concentrated between 0.0003 – 0.0004 mm for that reason it shows better fitting at higher displacement values.

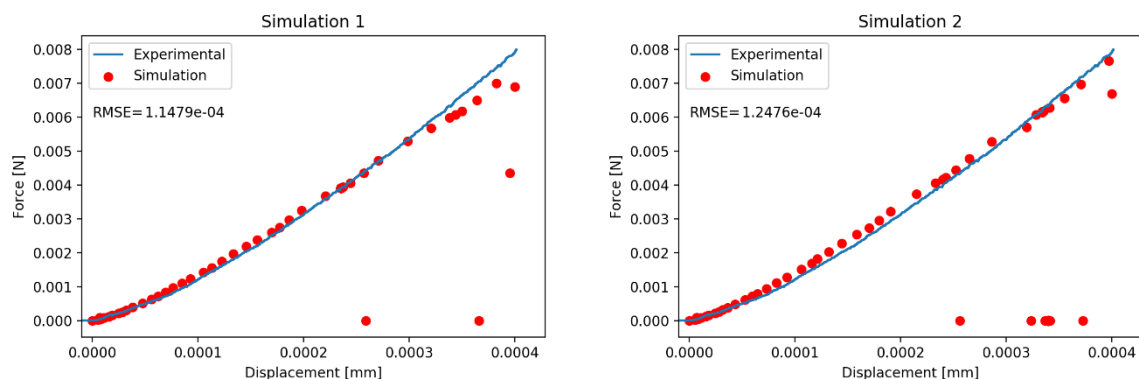


Figure 58: Two conducted simulations of PL steel and their RMSE values.

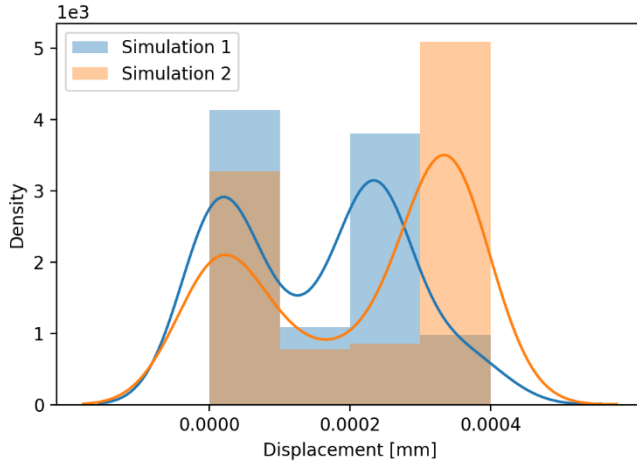


Figure 59: Distribution plot of the CP data of Simulation 1 and 2 based on their Displacement values

These findings support previous research (80) which links three error functions together in order to achieve better results in terms of curve fitting. It should be noted that using only RMSE is not wrong but lack of accuracy. So a new error function was created based on RMSE, the area under the curve (AUC), and the difference in maximum loads (DML). Alternatively, after calculating these three errors, based on their functions the data mentioned in three columns, and each column scaled between zero and one. Finally, the results are weighted based on the mentioned article (80), and the new error function is called Weighted Error (WE).

$$WE = 0.8 * (AUC) + 0.1 * (DML) + 0.1 * (RMSE) \quad 30.$$

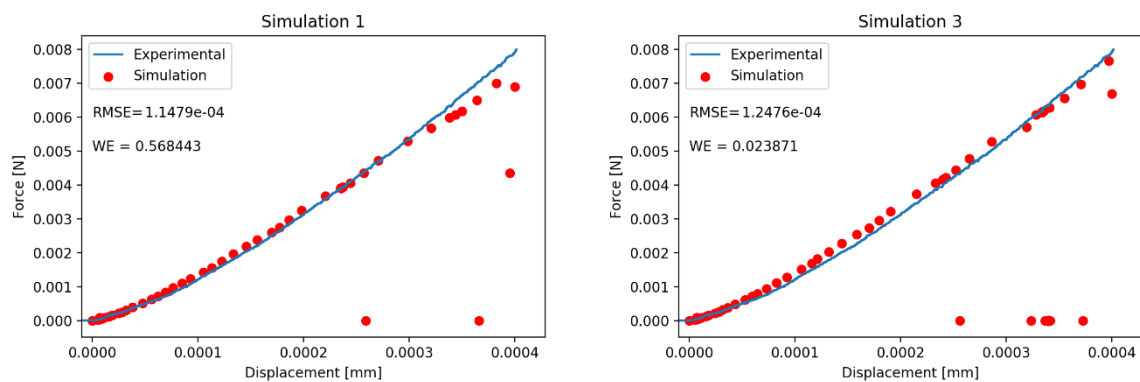


Figure 60: Comparison of the two error functions with conducted simulations.

As shown in **Figure 60**, the WE is significantly higher in Simulation 1 than Simulation 3, on the other hand, its RMSE is lower than Simulation 3. Because it can be seen that

in Simulation 1 data points are almost equal with the experimental data until 0.0003 mm then the deviation increases notably but because there are few data between 0.0003 and 0.0004 mm the RMSE is not influenced too much. On the contrary, for Simulation 3, despite showing a better fitting its RMSE is higher because of the slight deviation from 0.0001 mm. However, when DML and AUC are added to the error function, a better curve fitting evaluation can be done and the result also supports that Simulation 3 is better in terms of curve fitting. Despite the great success of the WE, all the optimization procedures carried on by using RMSE and there are neither time nor computational power left for resubmitting any simulations based on the new error function. For that reason, both error functions will be used for the evaluation of the models.

6.3 Artificial Intelligence Model

In order to compare the results of the AI model with the relevant literature (59 – 76), all the parameter data from Table 6 are compared with the results of the two AI models. For DP and PL steels, the data is collected from Table 11 and Table 13. The results obtained from these three tables are labeled by their parameters and summarized in **Figure 61**. In each graph, the parameters that are gathered by the literature are compared with the predictions of AI models by using distribution plots with kernel density estimators. As shown in Figure 61a both model's predictions overlap between 1 and 2 on the x-axis which is coherent with the literature. However, the PL curve is sharper compared to the other two curves. In Figure 61b, the DP and literature curves match each other, on the other hand, the PL curve significantly differs from these two curves. It has already been mentioned that PL steel exhibits a higher force compared to DP steel (see Figure 37). For that reason, the AI model tries to increase the maximum force by decreasing a parameter and increasing h_0 which is also supported by the MSA in **Figure 62**. So based on these facts, it can be seen that AI prioritizes a , h_0 parameters for the curve fitting. Figure 62c three curves overlap 50 – 150 MPa. DP curve is sharper than the PL curve but this difference does not play an important role. So apart from Figure 61d, the AI distribution curves are more or less similar to the literature curve. That shows that for three parameters the AI predictions are compatible with the literature for parameters a, τ_0, h_0 . When it comes to the τ_s , there is only one article that supports current findings (73). In that work, Diehl et al. gathered CP parameters from Tasan et al. (81), however, both τ_s and τ_0 have been modified based

on the elongated microstructure which can be seen in **Figure 63** and linked high τ_s values with elongated grains. Furthermore, their elongated microstructure matches with the current sample's microstructure (see Figure 34) and therefore high τ_s values make sense.

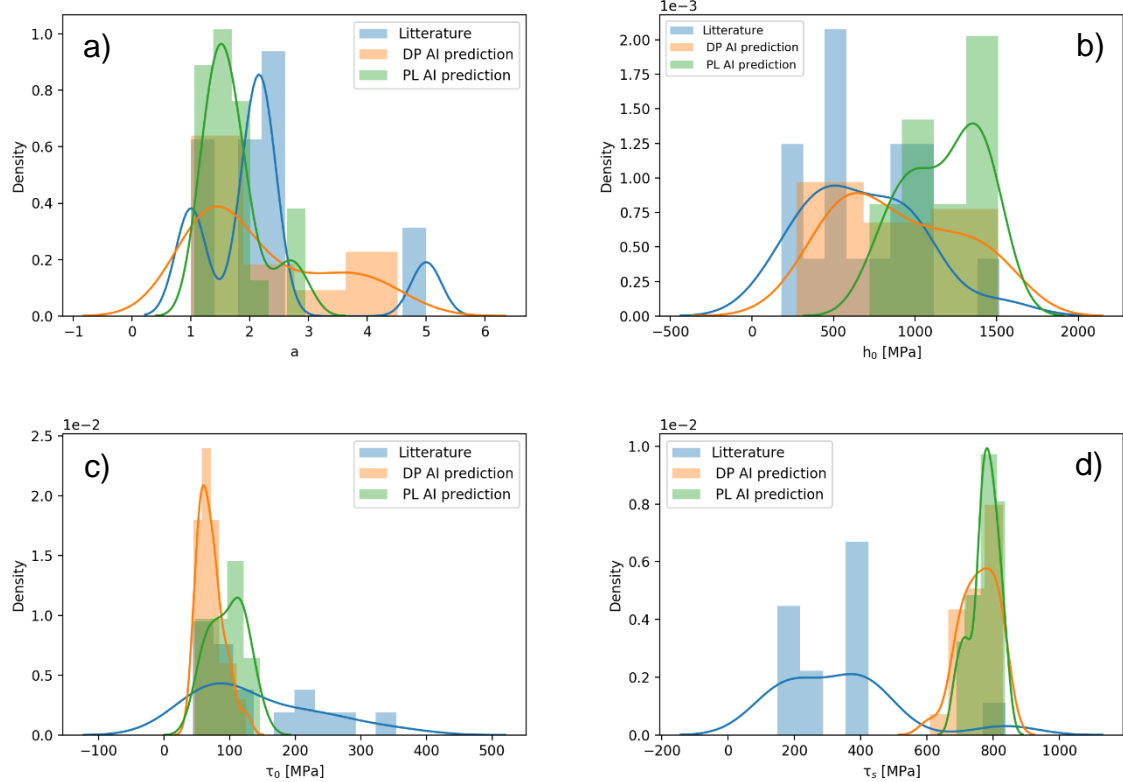


Figure 61: Comparison of AI models with the literature values.

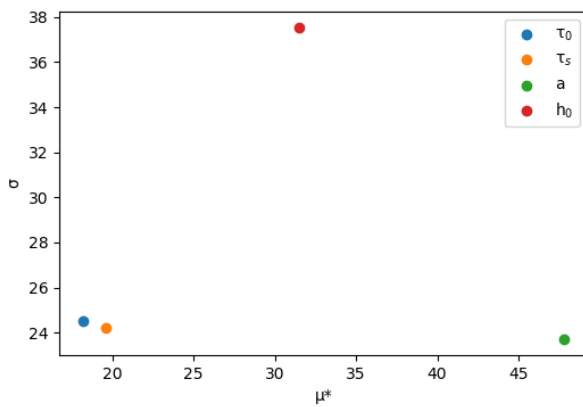


Figure 62: Morris sensitivity analysis based on maximum force.

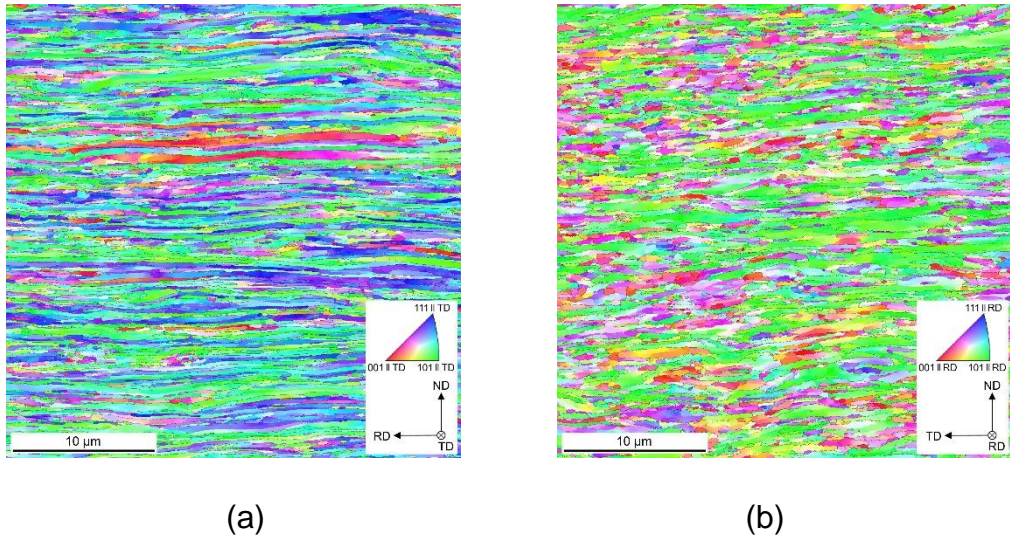


Figure 63: The microstructure maps showing (a) transverse direction (b) rolling direction . (73)

Finally, the success of the AI models for DP and PL steels is evaluated by using the two error functions and results are mentioned in **Figure 64**. Figure 64a shows the simulation which contains the lowest RMSE and Figure 64b presents the curve with the lowest WE for DP steel. It can be said that both curves are fairly fit well. This is a good example of proving that only RMSE as an error function is not wrong and can lead to good results if the data distributed evenly. Figure 64c shows the simulation which contains the lowest RMSE and WE at the same time which is also a good example to show that RMSE and WE can lead to the same result based on the distribution of the data. Lastly, it is also evident that AI predictions in all three figures are compatible with the reference and simulation data. Furthermore, the datasets of the mentioned graphs are given in **Table 19**.

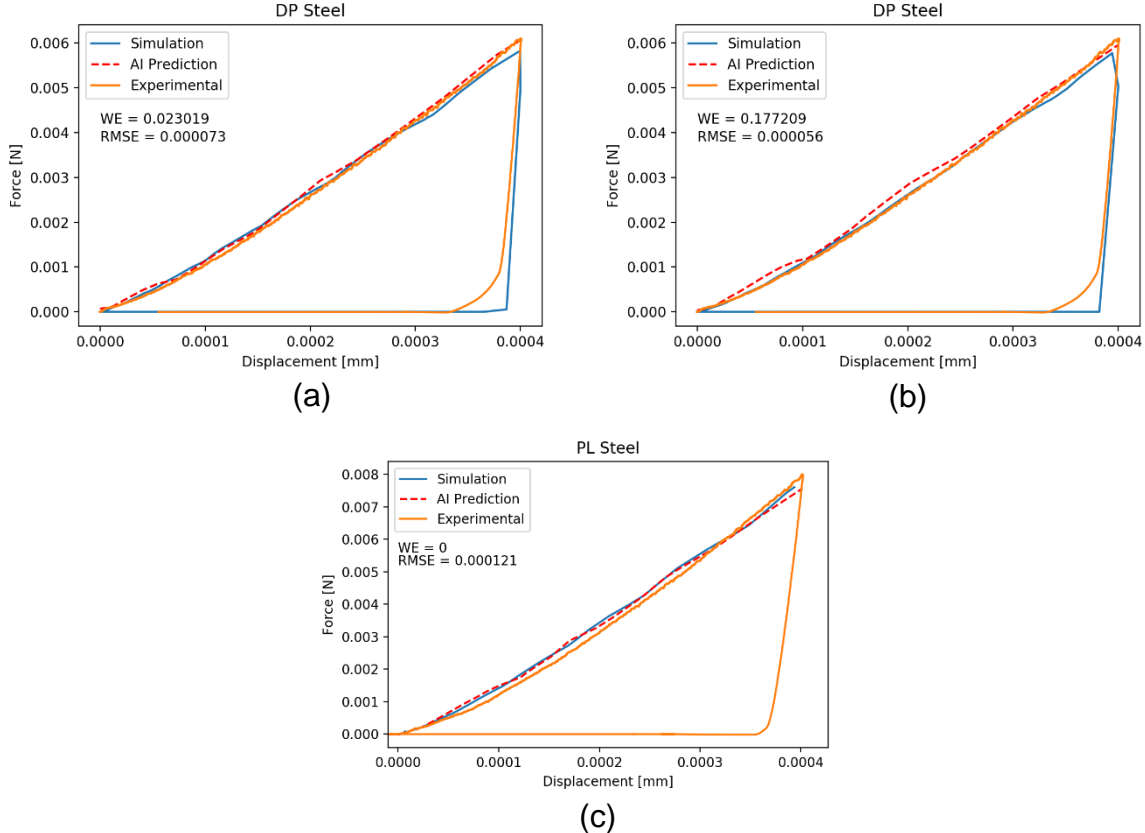


Figure 64: AI optimization results based on two error functions a,b) for DP steel c) for PL steel.

Table 19: Parameter sets of the simulations which are mentioned in Figure 64.

Figure No.	τ_0 , MPa	τ_s , Mpa	a	h_0 , Mpa
Figure 64a	47.40	727.48	1.65	986.31
Figure 64b	89.85	819.69	1.47	523.67
Figure 64c	67.12	824.66	1.27	1260.30

6.4 Response Surface Model

In this section, firstly, PSO results will be analyzed and then the simulations which are submitted after the second exploitation phase will be evaluated with two error functions.

It has been seen that the results of the exploration stage are almost the same for DP and PL steel variants which are 50 - 51 MPa for τ_0 and 1499 - 1500 MPa for

h_0 . In the following exploitation phase, only a slight difference has occurred between the two parameters (see **Table 20**) that is 4 MPa for the τ_0 parameter and 40 MPa for the h_0 parameter. The second exploitation phase causes a higher difference between h_0 that is more than 100 MPa but τ_0 values are still similar. Based on these similar results the sensitivity analysis became questionable. It has already been mentioned that the sensitivity analysis is based on the aim of the force-displacement curve because some simulations stop at the beginning or middle of the CPFEM analysis due to a convergency error. E.g. there are two curves, one contains a high degree of aim but ends up in the middle of the CPFEM analysis due to an error and for that reason its maximum force value is low. The second curve exhibits a lower aim but the simulation is successfully completed, for that reason its maximum force is higher. If their maximum force value were taken into account for the sensitivity analysis these convergency errors could influence the results. On the other hand, the AI model does not consider this information and for that reason, its sensitivity analysis is based on maximum force. But for the RS model, instead of the maximum obtained force, the aim of the slope is considered for the sensitivity analysis. However, these results show that τ_0 could have been taken constant for both steel variants and instead of τ_0 , optimizing a parameter could take place. The PSO results after the second exploitation phase, on the other hand, have some similarities with the AI results. The PL steel variant exhibits higher h_0 compared to DP steel and both steel variants show low τ_0 values. The τ_s and a values haven't been optimized but for the PL steel, these values are close to the AI predictions. Contrary, DP steel's τ_s and a values are far from their AI prediction. This deviation is probably caused by the inaccuracy of the RMSE method. With the WE function, these two parameters could have been closer to the AI predictions.

Table 20: PSO results after the first exploration and exploitation stages.

Stage	Steel Grade	τ_0 , MPa	h_0 , MPa	τ_s , MPa	a
Exploration	DP	51	1499	1000.86	4.57
	PL	50	1500	822.17	1.57
1.Exploitation	DP	54	1404	1000.86	4.57
	PL	58	1444	822.17	1.57
2.Exploitation	DP	67	1297	1000.86	4.57
	PL	63	1402	822.17	1.57

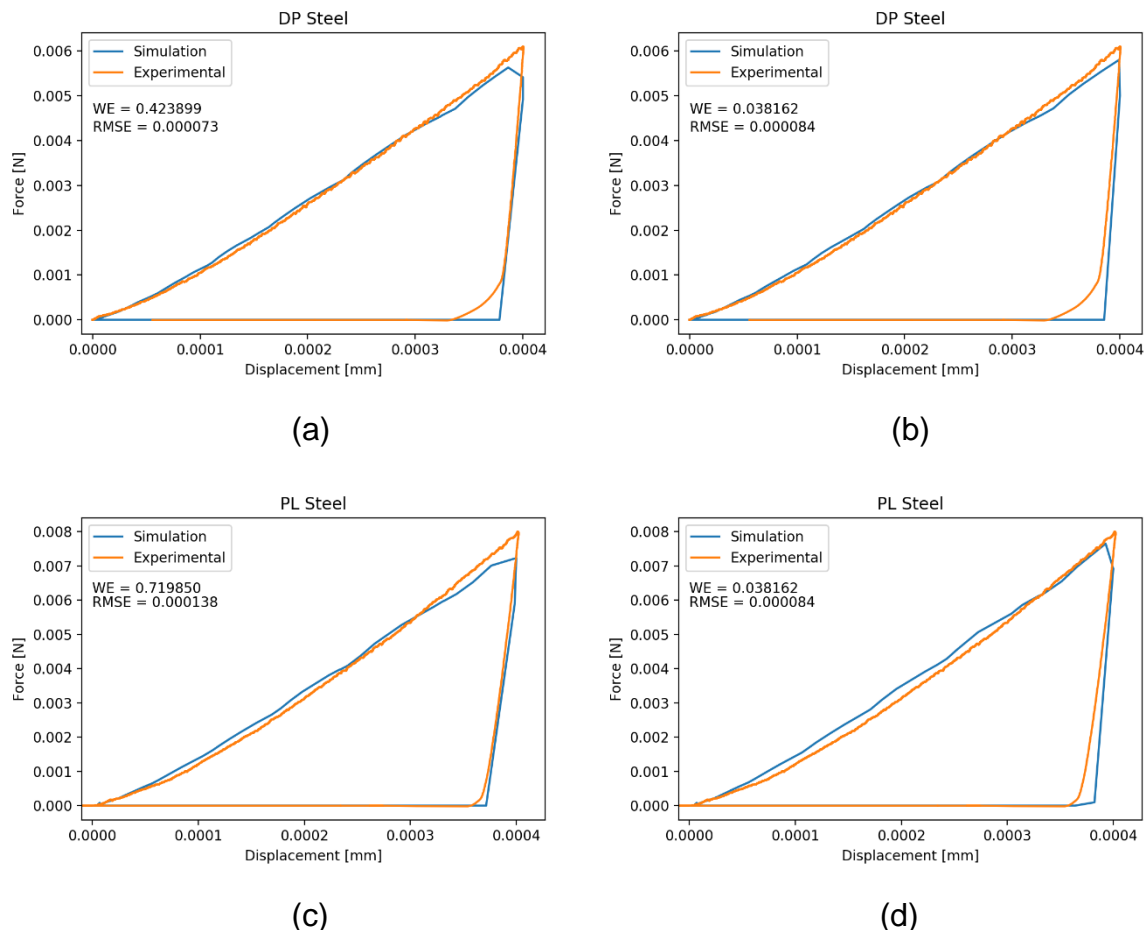


Figure 65: Second exploitation results evaluated with RMSE and WE functions for DP and PL steels

After the end of the second exploitation phase, 30 simulations have been submitted and the simulation results for both steel variants are evaluated via RMSE and WE and illustrated in **Figure 65**. From Figure 65(a,c), it can be seen that the fitting is not

succeeded at maximum force due to using only RMSE and this also explains why all the graphs in Figure 56 are insufficient in terms of curve fitting. Once again, fitting is high at the beginning of the curve and the deviation at the maximum load has a tiny effect on RMSE. Contrarily, when WE take place (see Figure 65b,d) the curve fitting gets better.

Table 21: Results from every single model.

Model	Steel Grade	τ_0 , MPa	h_0 , MPa	τ_s , MPa	α
AI (RMSE)	DP	47.40	986.31	727.48	1.65
AI (WE)	DP	89.85	523.67	819.69	1.47
AI (RMSE-WE)	PL	67.12	1260.30	824.66	1.27
RSM (RMSE)	DP	46.66	1554.50	1000.86	4.57
RSM (WE)	DP	47.57	1522.06	1000.86	4.57
RSM (RMSE)	PL	56.32	1449.65	822.17	1.57
RSM (WE)	PL	68.82	1432.12	822.17	1.57

After getting all the outcomes, they are mentioned in **Table 21**. It is seen that RS for DP steel gives above 1500 MPa for h_0 and 1000.86 MPa for τ_s but both variables are not valid in the provided literature (see Table 6). This result shows the flexibility of the RS model. It can extend the provided parameter range and can find the optimal data set. All the results indicate from the given parameter range (see Table 7) the lowest τ_0 and the highest τ_s values are determined for the ferrite CP parameters. For h_0 parameter the lowest value is 523 MPa and it goes up to 1550 MPa. It is visible that high h_0 values are best for the current samples. And lastly, the α value is mostly chosen between 1 – 2 as an exception 4.57 seems to be appeared due to the inaccuracy of the RMSE function but even this value is compatible with the current literature search (72).

7 Conclusion and Outlooks

This thesis aims to study the CP parameter of the phases in DP and PL steels. Through conducting nanoindentation experiments, simulations, and optimization models, the following conclusions can be drawn.

- By comparing the load-displacement curves obtained from the nanoindentation tests, it can be said that the hardness of the ferrite in PL steel is higher compared to the DP steel variant.
- Via automated CPFEM simulations, the CP parameters of the two ferrites from different steel variants are determined. A reasonably good agreement between numerical load-displacement curves and experimental results has been achieved.
- Despite unbalanced training data and low data density at higher loads, the AI model could achieve consistent solutions, and compare to the RS model outcomes are more successful. The only thing that should be implemented is the WE function instead of RMSE for the evaluation of AICS. However, the required computational power is far more than the RS model. To reduce this computational cost, the same model should be trained with less (e.g. 250) simulations and the optimum number of the required simulations should be determined.
- The number of data points gathered by the simulations can be increased by implementing polynomial regression. Based on the polynomial formula new data points can be generated which will increase the amount of the data training and test set which is vital for any AI model.
- The third dimension ‘time’ can be added to the force-displacement dataset and results can be post-processed based on time series analysis. For this instead of the perceptron algorithm, long short-term memory (LSTM) network can be used which is well suited with time-series data. By doing this the unloading part can be analyzed for further material properties like elasticity.
- RS model consists of 3 stages and in all these stages an issue has arisen. The evaluation of the sensitivity analysis might be inaccurate that's why ANOVA analysis should be carried out to double-check sensitivity analysis.
- Between exploration and exploitation stages only RMSE has been used to evaluate the outcome and it has been proved that RMSE is less accurate than

WE. Furthermore, RMSE is used 3 times in a single optimization process which definitely increases the bias term significantly. Not only RMSE but also PSO and polynomial regressions increase the bias term in each step. In order to decrease this bias, a higher degree polynomial equation and as an error function WE or unscaled WE function should be used. Furthermore, these changes will not increase the required computational source and within a week CP calibration can take place.

- The pile-up effect which occurs during the nanoindentation should be considered in CP calibration as well and therefore nanoindentation and pile-up simulation outputs have to be combined in a unique model.

8 Literatur

1. BULYCHEV, S.I., V.P. ALEKHIN, G.D. SHNYREV, A.P. TERNOVSKII und M.K. SHORSHOROV. Determining Young's modulus from the indentor penetration diagram. *Zavodskaya Laboratoriya*, 1975, **39**, 1137-1140.
2. H. HERTZ. Über die Berührung fester elastischer Körper [online]. *Journal für die reine und angewandte Mathematik*, 1881, **92**, 156-171. Verfügbar unter: <https://home.uni-leipzig.de/pwm/web/download/Hertz1881.pdf>
3. POON, B., D. RITTEL und G. RAVICHANDRAN. An analysis of nanoindentation in linearly elastic solids [online]. *International Journal of Solids and Structures*, 2008, **45**(24), 6018-6033. ISSN 00207683. Verfügbar unter: doi:10.1016/j.ijsolstr.2008.07.021
4. BAKER, L.J., S.R. DANIEL und J.D. PARKER. Metallurgy and processing of ultralow carbon bake hardening steels [online]. *Materials Science and Technology*, 2002, **18**(4), 355-368. ISSN 0267-0836. Verfügbar unter: doi:10.1179/026708302225002452
5. SAEED, N. und H.R. RONAGH. Design of fibre-reinforced polymer overwraps for pipe pressure. In: V.M. KARBHARI, Hg. *Rehabilitation of Pipelines Using Fiber-reinforced Polymer (FRP) Composites*: Woodhead Publishing, 2015, S. 211-223. ISBN 978-0-85709-684-5.
6. Code: ABAQUS CPFEM - EVOCD [online]. 7/25/2020 [Zugriff am: 10/28/2020]. Verfügbar unter: https://icme.hpc.msstate.edu/mediawiki/index.php/Code:_ABAQUS_CPFEM.htm
7. FONSTEIN, N. *Advanced high strength sheet steels*. Cham: Springer International Publishing; Imprint: Springer, 2015. ISBN 3319191659.
8. *Advanced High Strength Sheet Steels. Physical Metallurgy, Design, Processing, and Properties*. Cham: Springer International Publishing, 2015. ISBN 9783319191652.
9. *Piping handbook*. 7th ed. New York: McGraw-Hill, 2000. McGraw-Hill's AccessEngineering. ISBN 0070471061.
10. GRANBOM, Y., L. RYDE und J. JEPPSSON. Simulation of the Soaking and Gas Jet Cooling in a Continuous Annealing Line using Dilatometry [online]. *steel/*

research international, 2010, **81**(2), 158-167. ISSN 16113683. Verfügbar unter:
doi:10.1002/srin.200900097

11. GRANBOM, Y. *Structure and mechanical properties of dual phase steels. An experimental and theoretical analysis*. Doctoral Thesis. Stockholm, 2010.
12. YÜKSEL BILIR, Hg. *Çift Fazlı Çeliklerde Mikroyapının Mekanik Özelliklere Etkisi*: UCTEA Chamber of Metallurgical & Materials Engineers, 2016.
13. *History of Hardness Testing | Buehler* [online]. 4 Juli 2020 [Zugriff am: 4. Juli 2020]. Verfügbar unter: <https://www.buehler.com/history-of-hardness.php>
14. GIANNAKOPOULOS, A.E., P.-L. LARSSON und R. VESTERGAARD. Analysis of Vickers indentation [online]. *International Journal of Solids and Structures*, 1994, **31**(19), 2679-2708. ISSN 00207683. Verfügbar unter: doi:10.1016/0020-7683(94)90225-9
15. LOUBET, J.L., J.M. GEORGES, O. MARCHESINI und G. MEILLE. Vickers indentation curves of magnesium oxide {MgO}. *Tribol-T ASME*, 1984, **106**, 43-48.
16. PETHICA, J.B., R. HUTCHINGS und W.C. OLIVER. Hardness measurement at penetration depths as small as 20 Nm. *Philos. Mag.*, 1983, **48**, 593-606.
17. OLIVER, W.C. und G.M. PHARR. An improved technique for determining hardness and elastic modulus using load and displacement sensing indentation experiments [online]. *Journal of Materials Research*, 1992, **7**(6), 1564-1583. ISSN 0884-2914. Verfügbar unter: doi:10.1557/JMR.1992.1564
18. WANG, H., L. ZHU und B. XU. *Residual stresses and nanoindentation testing of films and coatings*. Singapore: Springer; Science Press Beijing, 2018. ISBN 9811078408.
19. FISCHER-CRIPPS, A.C. *Nanoindentation*. 3. ed. New York, NY: Springer Science+Business Media, LLC, 2011. Mechanical engineering series. 1. ISBN 9781441998729.
20. AGILENT TECHNOLOGIES. How to Select the Correct Indenter Tip [online]. Verfügbar unter:
<http://www.toyo.co.jp/files/user/img/product/microscopy/pdf/5990-4907EN.pdf>
21. OLIVER, W.C. und G.M. PHARR. Measurement of hardness and elastic modulus by instrumented indentation: Advances in understanding and refinements to methodology [online]. *Journal of Materials Research*, 2004, **19**(1), 3-20. ISSN 0884-2914. Verfügbar unter: doi:10.1557/jmr.2004.19.1.3

22. ROTERS, F. *Crystal plasticity finite element methods in materials science and engineering*. Weinheim: Wiley-VCH, 2010. ISBN 352732447X.
23. GOTTSTEIN, G. *Physical foundations of materials science*. Berlin: Springer, 2011], 2010. ISBN 9783642072710.
24. SCHMID, E. ber die Schubverfestigung von Einkristallen bei plastischer Deformation [online]. *Zeitschrift fr Physik*, 1926, **40**(1-2), 54-74. ISSN 1434-6001. Verfügbar unter: doi:10.1007/BF01390836
25. COURANT, R. Variational methods for the solution of problems of equilibrium and vibrations [online]. *Bulletin of the American Mathematical Society*, 1943, **49**(1), 1-24. ISSN 0002-9904. Verfügbar unter: doi:10.1090/S0002-9904-1943-07818-4
26. LIVESLEY, R.K. The Finite Element Method in Structural and Continuum Mechanics.O. C. Zienkiewicz. McGraw-Hill. 1967. 272 pp. Figures. 84s [online]. *The Journal of the Royal Aeronautical Society*, 1967, **71**(681), 659. ISSN 0368-3931. Verfügbar unter: doi:10.1017/S0001924000054695
27. LIN, P., J. NIE und M. LIU. Study on irradiation effect in stress-strain response with CPFEM during nano-indentation [online]. *Nuclear Materials and Energy*, 2020, **22**, 100737. ISSN 23521791. Verfügbar unter: doi:10.1016/j.nme.2020.100737
28. PEIRCE, D., R.J. ASARO und A. NEEDLEMAN. An analysis of nonuniform and localized deformation in ductile single crystals [online]. *Acta Metallurgica*, 1982, **30**(6), 1087-1119. ISSN 00016160. Verfügbar unter: doi:10.1016/0001-6160(82)90005-0
29. HARREN, S.V., H.E. DÈVE und R.J. ASARO. Shear band formation in plane strain compression [online]. *Acta Metallurgica*, 1988, **36**(9), 2435-2480. ISSN 00016160. Verfügbar unter: doi:10.1016/0001-6160(88)90193-9
30. KADKHODAPOUR, J., A. BUTZ, S. ZIAEI-RAD und S. SCHMAUDER. A micro mechanical study on failure initiation of dual phase steels under tension using single crystal plasticity model [online]. *International Journal of Plasticity*, 2011, **27**(7), 1103-1125. ISSN 07496419. Verfügbar unter: doi:10.1016/j.ijplas.2010.12.001
31. LIU, W., J. LIAN, N. ARAVAS und S. MÜNSTERMANN. A strategy for synthetic microstructure generation and crystal plasticity parameter calibration of fine-grain-structured dual-phase steel [online]. *International Journal of Plasticity*,

- 2020, **126**, 102614. ISSN 07496419. Verfügbar unter:
doi:10.1016/j.ijplas.2019.10.002
32. BOX, G.E.P. und K.B. WILSON. On the Experimental Attainment of Optimum Conditions [online]. *Journal of the Royal Statistical Society. Series B (Methodological)*, 1951, **13**(1), 1-45. ISSN 00359246. Verfügbar unter: www.jstor.org/stable/2983966
33. JIN, R., W. CHEN und A. SUDJANTO. An efficient algorithm for constructing optimal design of computer experiments [online]. *Journal of Statistical Planning and Inference*, 2005, **134**(1), 268-287. ISSN 03783758. Verfügbar unter: doi:10.1016/j.jspi.2004.02.014
34. SALTELLI, A. *Sensitivity analysis in practice. A guide to assessing scientific models*. Reprint. Hoboken, NJ: Wiley, 2007. ISBN 0470870931.
35. MORRIS, M.D. Factorial Sampling Plans for Preliminary Computational Experiments [online]. *Technometrics*, 1991, **33**(2), 161. ISSN 00401706. Verfügbar unter: doi:10.2307/1269043
36. CAMPOLONGO, F., J. CARIBONI und A. SALTELLI. An effective screening design for sensitivity analysis of large models [online]. *Environmental Modelling & Software*, 2007, **22**(10), 1509-1518. ISSN 13648152. Verfügbar unter: doi:10.1016/j.envsoft.2006.10.004
37. REN, J., W. ZHANG und J. YANG. Morris Sensitivity Analysis for Hydrothermal Coupling Parameters of Embankment Dam: A Case Study [online]. *Mathematical Problems in Engineering*, 2019, **2019**, 1-11. ISSN 1024-123X. Verfügbar unter: doi:10.1155/2019/2196578
38. HELTON, J.C., F.J. DAVIS und J.D. JOHNSON. A comparison of uncertainty and sensitivity analysis results obtained with random and Latin hypercube sampling [online]. *Reliability Engineering & System Safety*, 2005, **89**(3), 305-330. ISSN 09518320. Verfügbar unter: doi:10.1016/j.ress.2004.09.006
39. HUSSLAGE, B.G.M., G. RENNEN, E.R. VAN DAM und D. DEN HERTOG. Space-filling Latin hypercube designs for computer experiments [online]. *Optimization and Engineering*, 2011, **12**(4), 611-630. ISSN 1389-4420. Verfügbar unter: doi:10.1007/s11081-010-9129-8
40. LIU, Z.-z., W. LI und M. YANG. Two General Extension Algorithms of Latin Hypercube Sampling [online]. *Mathematical Problems in Engineering*, 2015, **2015**, 1-9. ISSN 1024-123X. Verfügbar unter: doi:10.1155/2015/450492

41. *Bio-Inspired Computation and Applications in Image Processing*: Elsevier, 2016. ISBN 9780128045367.
42. SEBER, G.A.F. und A.J. LEE. *Linear Regression Analysis*: Wiley, 2003. ISBN 9780471415404.
43. KENNEDY, J. und R. EBERHART. Particle swarm optimization. In: *Proceedings of ICNN'95 - International Conference on Neural Networks*: IEEE, 27. November 1995, S. 1942-1948. ISBN 0-7803-2768-3.
44. MENG, X. und Z. PIAN. Theoretical Basis for Intelligent Coordinated Control. In: *Intelligent Coordinated Control of Complex Uncertain Systems for Power Distribution Network Reliability*: Elsevier, 2016, S. 15-50. ISBN 9780128498965.
45. MARTÍNEZ, C.M. und D. CAO. Integrated energy management for electrified vehicles. In: *Ihorizon-Enabled Energy Management for Electrified Vehicles*: Elsevier, 2019, S. 15-75. ISBN 9780128150108.
46. VISHWANATHAN, A.S.V.N. An Introduction to Machine Learning [online]. Verfügbar unter: <https://alex.smola.org/drafts/thebook.pdf>
47. BEKKERMAN, R., M. BILENKO und J. LANGFORD. *Scaling Up Machine Learning*. Cambridge: Cambridge University Press, 2011. ISBN 9781139042918.
48. BISHOP, C.M. *Pattern recognition and machine learning*. 11. (corr. printing). New York: Springer, 2013. Information science and statistics. ISBN 9780387310732.
49. BENGIO, Y., A. COURVILLE und P. VINCENT. Representation Learning: A Review and New Perspectives [online]. *IEEE Transactions on Pattern Analysis and Machine Intelligence*, 2013, **35**(8), 1798-1828. ISSN 0162-8828. Verfügbar unter: doi:10.1109/TPAMI.2013.50
50. *Deep Learning in Digital Pathology* [online]. 8 November 2020 [Zugriff am: 8. November 2020]. Verfügbar unter: <http://www.global-engage.com/life-science/deep-learning-in-digital-pathology/>
51. *What the Hell is Perceptron? The Fundamentals of Neural Networks | by SAGAR SHARMA | Towards Data Science* [online]. 8 November 2020 [Zugriff am: 8. November 2020]. Verfügbar unter: <https://towardsdatascience.com/what-the-hell-is-perceptron-626217814f53>
52. ROJAS, R. *Neural networks. A systematic introduction*. Berlin: Springer-Verlag, 1996. ISBN 3642610684.

53. SCHEMMANN, L., S. ZAEFFERER, D. RAABE, F. FRIEDEL und D. MATTISSEN. Alloying effects on microstructure formation of dual phase steels [online]. *Acta Materialia*, 2015, **95**, 386-398. ISSN 13596454. Verfügbar unter: doi:10.1016/j.actamat.2015.05.005
54. THYSSENKRUPP STEEL EUROPE AG. DP-W® und DP-K® - Produktinformation für Dualphasen-Stähle [online]. Verfügbar unter: https://www.thyssenkrupp-steel.com/media/content_1/publikationen/produktinformationen/dp_w_dp_k/thyssenkrupp_dp-w_dp-k_produktinformation_steele_de.pdf
55. *Dual Phase steels* [online]. 8/18/2020 [Zugriff am: 8/18/2020]. Verfügbar unter: https://automotive.arcelormittal.com/products/flat/first_gen_AHSS/DP
56. ABID, N.H., R.K. ABU AL-RUB und A.N. PALAZOTTO. Computational modeling of the effect of equiaxed heterogeneous microstructures on strength and ductility of dual phase steels [online]. *Computational Materials Science*, 2015, **103**, 20-37. ISSN 09270256. Verfügbar unter: doi:10.1016/j.commatsci.2015.02.051
57. BERNARD ENNIS. *A review of the effects of chemical and phase segregation on the mechanical behaviour of multi-phase steels*, 2016.
58. WANG, J.Q., A. ATRENS, D.R. COUSENS und N. KINAEV. Microstructure of X52 and X65 pipeline steels [online]. *Journal of Materials Science*, 1999, **34**(8), 1721-1728. ISSN 00222461. Verfügbar unter: doi:10.1023/A:1004538604409
59. YANNIK LINDENPÜTZ. *Alternative Parameterbeschreibung des bimodalen Materialverhaltens in Rohrleitungsstahl auf der Mikrostrukturebene*. Master, 26. September 2019.
60. WU, B., N. VAJRAGUPTA, J. LIAN, U. HANGEN, P. WECHSUWANMANEE und S. MÜNSTERMANN. Prediction of plasticity and damage initiation behaviour of C45E + N steel by micromechanical modelling [online]. *Materials & Design*, 2017, **121**, 154-166. ISSN 02641275. Verfügbar unter: doi:10.1016/j.matdes.2017.02.032
61. W. D. T. SPANJER und PATRICK JUN HAO KOK. VIRTUAL EXPERIMENTAL STUDY OF MICROSTRUCTURE DESIGN OF DUAL PHASE STEEL FOR OPTIMAL FORMABILITY [online], 2018. Verfügbar unter: <https://www.semanticscholar.org/paper/VIRTUAL-EXPERIMENTAL-STUDY-OF-MICROSTRUCTURE-DESIGN-Spanjer-Kok/f5ae6adcaa5f6d3087af416b81d27c1565aea7c0#references>

62. JIA, N., Z.H. CONG, X. SUN, S. CHENG, Z.H. NIE, Y. REN, P.K. LIAW und Y.D. WANG. An in situ high-energy X-ray diffraction study of micromechanical behavior of multiple phases in advanced high-strength steels [online]. *Acta Materialia*, 2009, **57**(13), 3965-3977. ISSN 13596454. Verfügbar unter:
doi:10.1016/j.actamat.2009.05.002
63. VAJRAGUPTA, N., P. WECHSUWANMANEE, J. LIAN, M. SHARAF, S. MÜNSTERMANN, A. MA, A. HARTMAIER und W. BLECK. The modeling scheme to evaluate the influence of microstructure features on microcrack formation of DP-steel: The artificial microstructure model and its application to predict the strain hardening behavior [online]. *Computational Materials Science*, 2014, **94**, 198-213. ISSN 09270256. Verfügbar unter:
doi:10.1016/j.commatsci.2014.04.011
64. ROTERS, F., M. DIEHL, P. SHANTHRAJ, P. EISENLOHR, C. REUBER, S.L. WONG, T. MAITI, A. EBRAHIMI, T. HOCHRAINER, H.-O. FABRITIUS, S. NIKOLOV, M. FRIÁK, N. FUJITA, N. GRILLI, K.G.F. JANSSENS, N. JIA, P.J.J. KOK, D. MA, F. MEIER, E. WERNER, M. STRICKER, D. WEYGAND und D. RAABE. DAMASK – The Düsseldorf Advanced Material Simulation Kit for modeling multi-physics crystal plasticity, thermal, and damage phenomena from the single crystal up to the component scale [online]. *Computational Materials Science*, 2019, **158**, 420-478. ISSN 09270256. Verfügbar unter:
doi:10.1016/j.commatsci.2018.04.030
65. ABID, N.H., R.K. ABU AL-RUB und A.N. PALAZOTTO. Micromechanical finite element analysis of the effects of martensite morphology on the overall mechanical behavior of dual phase steel [online]. *International Journal of Solids and Structures*, 2017, **104-105**, 8-24. ISSN 00207683. Verfügbar unter:
doi:10.1016/j.ijsolstr.2016.11.005
66. ÇAKMAK, S.O. und T. YALÇINKAYA. Morphology and Grain Orientation Dependent Localization and Necking in Dual-phase Steels [online]. *Procedia Structural Integrity*, 2019, **21**, 224-232. ISSN 24523216. Verfügbar unter:
doi:10.1016/j.prostr.2019.12.105
67. VAJRAGUPTA, N., S. MAASEN, T. CLAUSMEYER, D. BRANDS, J. SCHRÖDER und A. HARTMAIER. Micromechanical Modeling of DP600 steel: From Microstructure to The Sheet Metal Forming Process [online]. *Procedia*

Manufacturing, 2020, **47**, 1540-1547. ISSN 23519789. Verfügbar unter:
doi:10.1016/j.promfg.2020.04.347

68. DELANNAY, L. Modeling of microscopic strain heterogeneity during wire drawing of pearlite [online]. *Procedia Manufacturing*, 2018, **15**, 1893-1899. ISSN 23519789. Verfügbar unter: doi:10.1016/j.promfg.2018.07.199
69. EVRARD, P., A. EL BARTALI, V. AUBIN, C. REY, S. DEGALLAIX und D. KONDO. Influence of boundary conditions on bi-phased polycrystal microstructure calculation [online]. *International Journal of Solids and Structures*, 2010, **47**(16), 1979-1986. ISSN 00207683. Verfügbar unter:
doi:10.1016/j.ijsolstr.2010.03.016
70. COLLINS, D.M., T. ERINOSHO, F.P.E. DUNNE, R.I. TODD, T. CONNOLLEY, M. MOSTAFAVI, H. KUPFER und A.J. WILKINSON. A synchrotron X-ray diffraction study of non-proportional strain-path effects [online]. *Acta Materialia*, 2017, **124**, 290-304. ISSN 13596454. Verfügbar unter:
doi:10.1016/j.actamat.2016.11.011
71. VAJRAGUPTA, N., H. UL HASSAN und A. HARTMAIER. Towards prediction of springback in deep drawing using a micromechanical modeling scheme [online]. *Procedia Engineering*, 2017, **207**, 60-65. ISSN 18777058. Verfügbar unter:
doi:10.1016/j.proeng.2017.10.739
72. CHOI, S.-H., E.-Y. KIM und S.I. KIM. The micromechanical deformation behaviors of hot-rolled 590FB steel during hole-expansion test [online]. *International Journal of Plasticity*, 2014, **58**, 184-200. ISSN 07496419. Verfügbar unter: doi:10.1016/j.ijplas.2013.11.010
73. DIEHL, M., J. NIEHUESBERND und E. BRUDER. Quantifying the Contribution of Crystallographic Texture and Grain Morphology on the Elastic and Plastic Anisotropy of bcc Steel [online]. *Metals*, 2019, **9**(12), 1252. Verfügbar unter:
doi:10.3390/met9121252
74. ZHANG, C., L.-W. ZHANG, W.-F. SHEN, Y.-N. XIA und Y.-T. YAN. 3D Crystal Plasticity Finite Element Modeling of the Tensile Deformation of Polycrystalline Ferritic Stainless Steel [online]. *Acta Metallurgica Sinica (English Letters)*, 2017, **30**(1), 79-88. ISSN 1006-7191. Verfügbar unter: doi:10.1007/s40195-016-0488-9
75. DELANNAY, L., P.J. JACQUES, K. DEJAEGHER und S.-S. SABLIN. Evaluation of two multiscale models for the simulation of cross-die forming of Dual Phase

- (DP) steels [online]. *International Journal of Material Forming*, 2008, **1**(S1), 65-68. ISSN 1960-6206. Verfügbar unter: doi:10.1007/s12289-008-0045-9
76. DA FONSECA, J.Q. und P.S. BATE. Evolution of Internal Stresses during the Plastic Deformation of IF Steel and Their Correlation with Crystal Orientation [online]. *Materials Science Forum*, 2005, **495-497**, 1055-1060. Verfügbar unter: doi:10.4028/www.scientific.net/MSF.495-497.1055
77. YAMANAKA, A., T. TAKAKI und Y. TOMITA. Numerical Prediction of Mechanical Properties of Steel using Multi-Phase-Field Method and Homogenization Method [online]. *The Proceedings of the Materials and Mechanics Conference*, 2008, **2008**(0), _OS0608-1_-_OS0608-2_. Verfügbar unter: doi:10.1299/jsmem.2008._OS0608-1_
78. BOUHLEL, M.A., J.T. HWANG, N. BARTOLI, R. LAFAGE, J. MORLIER und J.R.R.A. MARTINS. A Python surrogate modeling framework with derivatives [online]. *Advances in Engineering Software*, 2019, **135**, 102662. ISSN 09659978. Verfügbar unter: doi:10.1016/j.advengsoft.2019.03.005
79. Ackley Function [online]. 8/22/2020 [Zugriff am: 10/28/2020]. Verfügbar unter: <https://www.sfu.ca/~ssurjano/ackley.html>
80. LI, H., L. GUTIERREZ, H. TODA, O. KUWAZURU, W. LIU, Y. HANGAI, M. KOBAYASHI und R. BATRES. Identification of material properties using nanoindentation and surrogate modeling [online]. *International Journal of Solids and Structures*, 2016, **81**, 151-159. ISSN 00207683. Verfügbar unter: doi:10.1016/j.ijsolstr.2015.11.022
81. TASAN, C.C., J.P.M. HOEFNAGELS, M. DIEHL, D. YAN, F. ROTERS und D. RAABE. Strain localization and damage in dual phase steels investigated by coupled in-situ deformation experiments and crystal plasticity simulations [online]. *International Journal of Plasticity*, 2014, **63**, 198-210. ISSN 07496419. Verfügbar unter: doi:10.1016/j.ijplas.2014.06.004